12-2020

Regulator of Gene Silencing Calmodulins: Components of RNA granules and autophagy during plant stress

W. Craig Conner
University of Tennessee

To the Graduate Council:

I am submitting herewith a dissertation written by W. Craig Conner entitled "Regulator of Gene Silencing Calmodulins: Components of RNA granules and autophagy during plant stress." I have examined the final electronic copy of this dissertation for form and content and recommend that it be accepted in partial fulfillment of the requirements for the degree of Doctor of Philosophy, with a major in Biochemistry and Cellular and Molecular Biology.

Daniel M. Roberts, Major Professor

We have read this dissertation and recommend its acceptance:

Tessa Burch-Smith, Andreas Nebenführ, Brad Binder, Elizabeth Fozo

Accepted for the Council:

Dixie L. Thompson

Vice Provost and Dean of the Graduate School

(Original signatures are on file with official student records.)

Regulator of Gene Silencing Calmodulins: components of RNA granules and autophagy during plant stress

A Dissertation Presented for the

Doctor of Philosophy

Degree

The University of Tennessee, Knoxville

William Craig Conner

December 2019

ACKNOWLEDGEMENTS

I am deeply grateful to the many people who have helped me over the years. There have been many small instances of brief conversations which ended up dramatically shaping the course of my research. There is no shortage of talented and generous professors and graduate students in this department, and I am grateful that they lent me their time and expertise. I hope that I have been able to do the same for others and can continue doing so.

I would especially like to thank my mentor Dr. Dan Roberts. He is an excellent scientist, mentor and role model. He has provided advice, insight and considerable patience as I veered the research ever farther from our lab's traditional focus areas. I would also like to thank Dr. Tessa Burch-Smith, Dr. Andreas Nebenführ and Dr. John Dunlap for helping me with my microscopy. Their help with my many technical questions has been indispensable. We have also relied heavily on Dr. Burch-Smith, whose substantial experience working with plant viruses and stress granules in tobacco has been instrumental to our work.

I also want to thank my graduate student friends and colleagues. When I first started, Ansul Lokdarshi, Pintu Masalkar, JinHa Hwang and Tian Li were always willing to help me when I approached them with my many annoying questions. Ansul has also spent countless hours teaching me all the essential lab skills. They are highly talented, and I wish them the best. Sterling Field is also a fantastic scientist, a great friend, and is a major asset to this research project.

I also want to give a special thanks to Dr. Jae Park. He spent countless hours personally working with me at a time when I had no prior lab experience. It is thanks to his generosity that I was able to decide that I wanted to pursue graduate research.

Lastly, I thank my family. They have always been incredibly supportive. Their love and support mean the world to me.

ABSTRACT

The central focus of this work is to understand how “regulator of gene silencing calmodulin” (rgsCaM) homologs regulate the RNA cycle at the level of cytosolic mRNP bodies under cellular stress. While rgsCaM is best known as an endogenous suppressor of gene silencing in tobacco, our findings for a homologous protein in Arabidopsis, “calmodulin-like protein 38” (CML38), suggest that a broader function in the regulation of mRNP bodies may be common to this family of calmodulin-like proteins. CML38 is induced by hypoxia stress, contributes to plant survival under hypoxia, and localizes to stress-induced mRNP bodies called stress granules (SGs), as well as to processing bodies (PBs). Members of this protein family target viral and endogenous proteins for degradation through the autophagy pathway. We propose that rgsCaM and its relatives may localize to stress-induced mRNP bodies and target them for autophagic degradation (granulophagy). In our investigations for rgsCaM, we used hypoxia stress as a means to induce stress granule formation and found that rgsCaM localizes to hypoxia-induced cytosolic granules which are both independent of but at the same time often bound to SGs and PBs. We further show that rgsCaM colocalizes with the autophagosome cargo-binding protein “autophagy-related gene 8” (ATG8e) and interacts with ATG8e *in planta* by bimolecular fluorescence complementation (BiFC) assay. Mutations disrupting the N-terminus of rgsCaM, or ones affecting the ability of ATG8 to bind cargo adaptors caused a loss in BiFC interaction. This suggests that the N-terminus contains a site for binding to the cargo binding protein ATG8e, and which might mediate the targeting of rgsCaM and bound cargo to autophagosomes as part of

the granulophagy process. For future studies, a Förster resonance energy transfer-based approach for probing rgsCaM interactions *in vivo* is demonstrated.

In a second thrust, we report the development of a novel, fluorescence-based, quantitative oxygen biosensor to facilitate the non-invasive assessment of the oxygen status of cells of living cells by fluorescent imaging.

TABLE OF CONTENTS

Chapter 1: Introduction 1

1.1 Plant abiotic stress survival in a changing climate 1

1.2 Low oxygen stress in higher plants: Perception, signaling, and responses 2

1.2.2 Hypoxia response 6

1.2.3 Calcium signaling during hypoxia 8

1.3 Arabidopsis Calmodulin-like 38 is a hypoxia-induced calcium sensor protein necessary for low oxygen stress survival 11

1.4 Regulator of Gene Silencing Calmodulins 14

1.4.1 Antiviral gene-silencing in plants 14

1.4.2 Regulator of gene silencing CaMs as targets for viral suppressors of gene silencing 22

1.4.3 rgsCaMs constitute a phylogenetic subclass of structurally related calcium-sensors and may have a common silencing suppression function 24

1.5 Hypoxia stress induces a global inhibition of translational initiation 28

1.5.1. Mechanism of translational inhibition in plants 28

1.5.2 The RNA cycle: Stress granules and Processing bodies 29

1.6. Goals of research 31

Chapter 2: Materials and Methods 33

2.1 Molecular cloning techniques and procedures 33

2.1.1 Generation of fluorescent protein fusions for co-localization experiments. 33

2.1.2 Generation of ratiometric BiFC constructs 40

2.1.3 Construction of the hypoxia sensor 42

2.2 Plant growth and transfection 44

2.3 Slide preparation and hypoxia treatment 46

2.4 Cycloheximide treatment 46

2.5 Microscopy and imaging techniques 47

2.6 Image analysis and processing 49

2.7 Infection of Arabidopsis with turnip mosaic virus 53

2.8 Generating multiple sequence alignments and phylogenetic trees 53

2.9 GeneID and accession numbers 54

Chapter 3: Results 55

3.1 Arabidopsis CML38 localizes to hypoxia-induced mRNP stress granules and processing bodies 55

3.2 Subcellular localization of Nicotiana tabacum regulator of gene silencing calmodulin 68

3.3 Nicotiana tabacum regulator of gene silencing calmodulin localizes to hypoxia-induced granules 69

3.4 Suppressor of Gene Silencing 3 shows strong co-localization with SG and increases rgsCaM localization to these structures 86

3.5 rgsCaM and CML38 are implicated in autophagy and contain putative ATG8-interacting motifs in their N-termini 91

3.6 rgsCaM colocalizes with autophagosome marker ATG8e and binds this protein through an AIM site 97

3.7 Mutation of the putative ATG-interacting motif does not prevent rgsCaM granulation or colocalization to foci with ATG8e 108

3.8 rgsCaM and ATG8e colocalize at the periphery of mRNP granules in late hypoxia 108

3.9 The rgsCaM S16A mutant shows greater nuclear localization than wt 111

3.10 rgsCaM interacts with TuMV HC-Pro by BiFC and FRET 113

3.11 Loss of CML38 delays systemic Turnip mosaic virus infection in Arabidopsis 120

3.12 Development of a novel fluorescent hypoxia biosensor based on oxygen-dependent N-degron-mediated proteolysis 121

Chapter 5: Discussion 129

4.1 rgsCaM and CML38 are homologous, stress-induced, mRNP localizing proteins 129

4.2 CML38 delays TuMV infection 131

4.3 rgsCaM targets mRNP bodies under hypoxia stress 134

4.4 rgsCaM interaction with ATG8 resembles that of autophagy cargo adaptors 137

4.5 rgsCaM S16 affects nuclear localization 145

4.6 rgsCaM as a calcium sensor 146

4.7 Model: rgsCaM induces mRNP recycling during stress 148

4.8 The suppression of silencing of rgsCaMs 152

4.9 Future directions for rgsCaM-like proteins 153

4.10 The pHypox 2 construct is a promising system for reporting in vivo hypoxia 154

List of references 158

Vita 181

LIST OF TABLES

Table 1 PCR primers for molecular cloning, mutagenesis and sequencing..... 34

Table 2 Sequence similarity for N-terminal domains of rgsCaM-like proteins, with At-CaM7 as a calmodulin reference. 96

Table 4 Pearson's correlation coefficients 136

Table 3 Mander's co-localization coefficients..... 136

LIST OF FIGURES

Figure 1 Shared components of trans-acting siRNA and secondary viral siRNA biosynthesis and sense-transgene silencing. 21

Figure 2 Phylogenetic tree and multiple sequence alignment of rgsCaM-like proteins in Arabidopsis and tobacco 25

Figure 3 Representative donor plasmid, pDONR 207, and donor construct, pDONR 207 CML38. 38

Figure 4 Vector map of pDONR/Zeo with assembled hypoxia sensor coding sequence 43

Figure 5 Phylogeny of tobacco rgsCaMs and Arabidopsis CaMs and CMLs 56

Figure 6 Representative pEarleyGate plasmid, pEarleyGate 101.. 58

Figure 8 Representative pEarleyGate localization construct, pEarleyGate 101 *CML38*.. 59

Figure 8 CML38 localizes to hypoxia-induced cytosolic foci. 61

Figure 9 CML38 colocalizes with the stress granule marker RBP47B to hypoxia-induced cytosolic granules. 63

Figure 10 Cycloheximide treatment prevents hypoxia-induced CML38 granule formation. 65

Figure 11 At-CaM2 does not localize to cytosolic foci in response to hypoxia under conditions. 64

Figure 12 CML38-YFP strongly colocalizes with PB-marker DCP1. 67

Figure 13 Localization of rgsCaM-YFP to cytosolic granules in *N benthamiana* leaf cells. 70

Figure 14 RgsCaM-YFP time series of granule formation in response to hypoxia. 71

Figure 15 Co-localization of rgsCaM-YFP and RBP47B-CFP 72

Figure 16 Fitting of SG-marker RBP47B and rgsCaM imaging data to 3D models 74

Figure 17 Co-localization of rgsCaM-YFP and processing body markers in hypoxic *N. benthamiana* leaves 76

Figure 18 Processing body marker DCP1-CFP colocalization with rgsCaM-YFP in *N. benthamiana* leaves 77

Figure 19 Fitting of PB-marker DCP1 and rgsCaM imaging data to 3D models 78

Figure 20 rgsCaM granule docking onto DCP1 processing body. 80

Figure 21 SGS3 localization time course in *N. benthamiana* leaves 82

Figure 22 rgsCaM associates with cytosolic SGS3 granules 83

Figure 23 SGS3 granules form before rgsCaM granules 84

Figure 24 Colocalization of rgsCaM-CFP and SGS3-YFP 85

Figure 25 Colocalization of RBP47B and SGS3 87

Figure 26 SGS3 and RBP47 colocalization in *N. benthamiana* cells. 88

Figure 27 SGS3 and DCP1 colocalization in *N. benthamiana* leaves..... 89

Figure 28 Colocalization of SGS3-CFP, RBP47-RFP and rgsCaM-YFP in *N. benthamiana* 90

Figure 29 At-CML38 also colocalizes with SGS3 in hypoxia-induced cytosolic foci 92

Figure 30 CaM2 does not localize to hypoxia-induced foci and does not colocalize with SGS3..... 93

Figure 31 Multiple sequence alignment of N-terminal domains of rgsCaM-like proteins 95

Figure 32 rgsCaM colocalizes with ATG8e under hypoxia 98

Figure 33 Representative vector map for a pBiFC 2-in-1 plasmid, pBiFC NC. 100

Figure 34 Representative vector map for a the BiFC construct "pBiFC NC ATG8e, rgsCaM" 102

Figure 35 Bimolecular fluorescence complementation of wt and mutant or truncated forms of Nt-rgsCaM and At-ATG8e 105

Figure 36 Quantification of rBiFC signals for wt and mutant forms of both rgsCaM and ATG8e. 107

Figure 37 Mutation of rgsCaM putative AIM motif does not prevent granulation. 109

Figure 38 rgsCaM AIM domain mutation does not prevent ATG8e colocalization 110

Figure 39 rgsCaM and ATG8e localization to the periphery of DCP1 and SGS3 bodies 112

Figure 40 rgsCaM S16A shows greater nuclear localization than wt rgsCaM 114

Figure 41 *In vivo* interaction of RgsCaM and TuMV HC-Pro by bimolecular fluorescence complementation 115

Figure 42 rgsCaM and HC-Pro partially co-localize to cytosolic foci under hypoxia 117

Figure 43 Acceptor photobleaching FRET for rgsCaM-mTRQ2 and Venus-HC-Pro 119

Figure 44 Constitutive expression of the rgsCaM-like protein CML38 in Arabidopsis delays TuMV systemic infection. 122

Figure 45 Hypoxia sensor validation in *N. benthamiana* 125

Figure 46 Plasmid map of pHypox 2 for *in vivo* ratiometric hypoxia quantification 127

Figure 47 Expression of pHypox 2 in *N. benthamiana* 128

Figure 48 The disrupted third EF-hands of rgsCaM-like proteins. 132

Figure 49 Multiple sequence alignment of rgsCaM homologs of the Solanaceae family 144

Figure 50 Model for rgsCaMs as autophagic cargo adaptors for stress-induced degradation of mRNP bodies 149

Chapter 1: Introduction

1.1 Plant abiotic stress survival in a changing climate

Since the first freshwater photosynthesizing multicellular eukaryotes emerged a billion years ago, the evolution of land plants has been driven by natural selection for genetic adaptations to harsh and varied environments (Stewart et al. 1993). It was not until 470 million years ago when the first recognizable land plants with roots and leaves, the embrophytes, first appeared (Stewart et al. 1993). Once rooted in the ground, a plant lives or dies by its ability to tolerate the changing stresses of its local environment. Flooding, drought, heat, cold, salt, too much or too little light, and low nutrients are some of the major abiotic stresses that plants experience. Evolution has produced plants that thrive in extreme conditions, and even plants that live in comparatively mild environments have evolved adaptive responses (Zhu 2016). These responses allow them to survive a variety of stresses for short periods, although some are clearly more adept than others (Zhu 2016). In particular, the few agricultural crop varieties on which we depend have been primarily selected based on yield and not stress tolerance.

As we face accelerated climate change, it is evident that the stress tolerance of crops is not adequate to sustain an exponentially growing human population. The 2018 report from the United Nations Intergovernmental Panel on Climate Change (IPCC) highlights the severity of the effects of human activities on the ability of our environment to sustain human life by the year 2050 (IPCC 2018). To continue producing enough food, we will need to grow crops in less optimal lands and conditions. As an example of the challenges faced, prolonged flooding or drought can devastate a field of crops, and

from 2011 data, together these accounted for over 70% of yield losses (Bailey-Serres et al. 2012).

Plant biologists have a major role to play in solving this problem of greater demand for food and increases in extreme weather. A strong understanding of the molecular and genetic mechanisms of plant stress tolerance is critical for engineering improved adaptive responses in the agricultural crops on which we depend. Traditional selective breeding alone is unlikely to be enough to produce high-yield, stress tolerant crops in time to prevent the expected food shortages by 2050 (IPCC 2018), but advances in genome editing and synthetic biology hold great promise (Goold et al. 2018). With these emerging technologies, scientists can attempt to directly introduce genes contributing to stress adaptations into crops, from anywhere in the plant kingdom or beyond, and they can engineer these genes in entirely new ways. Before any of these improvements will be possible, we must understand how the stress adaptation responses in plants function. Of interest in this study is flooding, which is a low oxygen stress affecting energy metabolism.

1.2 Low oxygen stress in higher plants: Perception, signaling, and responses

Hypoxia is a low-oxygen stress resulting from plant submergence or soil waterlogging. Aerobic respiration requires molecular oxygen as a terminal electron acceptor in the electron transport chain, and insufficient oxygen translates into insufficient ATP production and an energy crisis within cells. Flooded or waterlogged soil has 10^4-fold lower gas diffusion (Bailey-Serres et al. 2012). Further, soil bacteria rapidly consume the available dissolved oxygen under conditions of submergence,

further promoting hypoxic conditions (Bailey-Serres et al. 2012). To compensate for the resulting energy crisis, cells must redirect their energy metabolism to less efficient anaerobic pathways: lactic acid or ethanolic fermentation (van Dongen et al. 2015). This change in metabolism requires broad changes in gene expression, and accompanying sensory mechanisms, signal transduction, and effectors which can enact these changes (van Dongen et al. 2015, Fukao et al. 2019). While any plant cell can experience a shortage in ATP production due to low oxygen (Voesenek et al. 2015), hypoxia is a more commonly experienced in roots than above-ground tissues, since a heavy rain waterlogs the soil, while the above-ground tissues are not directly affected. Some tissues are also naturally hypoxic (Bailey-Serres et al. 2012, Shukla et al. 2019). For instance, as roots grow, the meristems at lateral root primordia have high metabolic activity due to rapid growth and division. This activity consumes oxygen faster than it can passively diffuse into the cells, creating a hypoxic micro-environment (Shukla et al. 2019). In another example, leguminous plants use a tissue structural strategy consisting of a water diffusion barrier to deliberately create hypoxic zones within their endosymbiotic nitrogen-fixing nodules (Minchin 1997). This is advantageous because the nitrogenase enzyme within is inactivated by oxygen (Layzell et al. 1990). Thus, we see that the hypoxia adaptive response is triggered both environmentally and developmentally.

Before plants can activate a response program to low oxygen stress, they must first sense the condition. There are two general strategies for sensing oxygen: direct and indirect. In direct sensing, an oxygen-dependent process directly regulates a sensor protein (van Dongen et al. 2015, Fukao et al. 2019). Indirect oxygen sensing

mechanisms are triggered by the consequences of poor energy metabolism, such as reactive oxygen species produced by the mitochondria (Fukao et al. 2019).

An example of the first mechanism is the group VII family of ethylene response transcription factors (ERF-VII), which are primary activators for many of the anaerobic response genes (Fukao et al. 2019). Most ERF-VII transcription factors act as direct oxygen sensors (van Dongen et al. 2015). All ERF-VII proteins have a conserved DNA-binding domain in common with the APETALA2 transcription factor (van Dongen et al. 2015), and as such are named “related to APETALA2,” or RAP proteins. ERF transcription factors are transcriptionally upregulated by ethylene signaling (Muller et al. 2015). Ethylene gas is constitutively produced under unstressed conditions, and three of the five ERF-VII genes in Arabidopsis (RAP2.2, RAP2.3 and RAP2.12) are constitutively expressed. While ethylene easily diffuses from plant tissues into the air, it diffuses poorly in water. Thus, cellular ethylene accumulates during submergence and waterlogging (Bailey-Serres et al. 2012).

ERF-VII transcription factors undergo oxygen-dependent, N-degron-mediated proteolysis under normal oxygen conditions (normoxia), but accumulate as oxygen levels fall (Licausi et al. 2011). ERF-VII proteins have a cysteine at their N-termini (the initiating methionine is removed with a methionine amino peptidase) (Bailey-Serres et al. 2012). In the N-degron pathway, certain N-termini are recognized by specific E3 ligases, with the first amino acid having the largest influence over protein half-life (Tasaki et al. 2012). An N-terminal cysteine is known as a secondary destabilizing residue (Tasaki et al. 2012). Proteins with an N-terminal cysteine tend to have a long half-life (Tasaki et al.

2012). However, these cysteines can be modified and arginylated (Tasaki et al. 2012, Weits et al. 2014). This newly-added N-terminal arginine is a destabilizing residue with a very short half-life (Tasaki et al. 2012, Weits et al. 2014). In this arginylation mechanism of ERF-VII transcription factors, plant cysteine oxidases (PCO) use molecular oxygen as a cofactor to oxidize the N-terminal cysteine of ERF-VII proteins to cysteine-sulphinic acid (CSA) (Weits et al. 2014). The dioxygenase activity of PCOs are maximal at 20% oxygen and have a near-linear decline in activity with decreased oxygen (White et al. 2018). CSA is a substrate for arginyl-transfer RNA transferases (ATE), which add an arginine to the N-terminus. Specific E3-ligases recognize proteins with an N-terminal arginine and target them for degradation in the 26S proteasome (Weits et al. 2014). Thus, these constitutively expressed ERF-VIIs are degraded except when oxygen levels fall, at which point they activate anaerobic response genes.

Additional regulatory mechanisms ensure that ERF-VIIs can have rapid on/off transitions in response to changing O_2 concentrations. RAP2.12 (and likely other ERF-VIIs) are tethered to the plasma membrane under normoxia by binding acyl-coenzyme A binding protein 1 (ACBP1) and 2 (van Dongen et al. 2015). This binding also prevents cysteine oxidation (van Dongen et al. 2015). Under hypoxia, RAP2.12 is released from the plasma membrane, although the mechanism is unclear (van Dongen et al. 2015). The advantage of this tethering is that a pool of RAP2.12 can persist under normoxia and remain sequestered outside the nucleus, ready to be released during hypoxia for a rapid response (van Dongen et al. 2015). A negative feedback mechanism is used to ensure rapid inactivation of RAP2.12 (Giuntoli et al. 2014, van Dongen et al. 2015).

Under hypoxia, the RAP2.12 transcription factor induces expression of hypoxia response attenuator 1 (HRA1), a RAP2.12 inhibitor (Giuntoli et al. 2014, van Dongen et al. 2015).

Indirect sensory mechanisms of hypoxia are less clear. However, the major cellular changes which accompany insufficient energy metabolism are changes in adenylate charge (increased [ADP] to [ATP] ratio), increased reactive oxygen species, nitric oxide, ethylene, calcium signaling, decreased cytosolic pH, and tissue-specific changes in [K^+] (Fukao et al. 2019).

1.2.2 Hypoxia response

Hypoxia sensing is followed by changes in gene expression both at the transcriptional and translational levels (Bailey-Serres et al. 2012). However, during hypoxia many mRNAs are held translationally inactive and sequestered into messenger ribonucloprotein particle (mRNP) aggregates. Further, some mRNAs are upregulated by hypoxia but are not translated until recovery (Branco-Price et al. 2008)

Arabidopsis has 49 core hypoxia response genes which are highly translated in all tissues and developmental stages examined (Mustroph et al. 2009). In order to determine which mRNAs were translated under hypoxia across a range of tissues and developmental states, Mustroph *et. al.* (2008) used a strategy involving expressing and immunoprecipitating FLAG-tagged ribosomal protein L18 (FLAG-RPL18) under a variety of cell and tissue-specific promoters. RPL18 is a component of the 60S large ribosomal subunit, and as such associates with actively translated mRNAs, and not with those in stalled translational pre-initiation complexes (Mustroph et al. 2009). Following immunoprecipitation with an anti-FLAG antibody, RNA microarray was performed to

identify actively translated mRNAs (Mustroph et al. 2009). The analysis involved nine promoters specific to different root tissues, three to shoot and cotyledons, as well as the near-constitutive CaMV 35S promoter (Mustroph et al. 2009). Co-immunoprecipitated mRNA was subjected to microarray analysis to identify highly translated mRNAs for each tissue type (Mustroph et al. 2009). Among these, there were 49 mRNAs with elevated translation in all tissues which constitute the core hypoxia response genes. These core hypoxia response genes include anaerobic metabolism enzymes like ALCOHOL DEHYDROGENASE 1 (ADH1), transcription factors, signaling proteins, but also many with no known function (Mustroph et al. 2009).

Hypoxia response strategies vary among—and even within—plant species. For example, there are three major strategies: rapid growth, aerenchyma, and quiescent strategies. Rapid growth is employed by the *Oryza sativa* strain Deepwater rice, which is semi-aquatic. Deepwater rice has SNORKEL1 and 2 ERF transcription factors which promote stem elongation during flooding (Hattori et al. 2009). Here, the strategy is to mobilize stored carbohydrates to stay above the water level, avoiding complete submergence rather than tolerating it *(Bailey-Serres et al. 2012)*. Alternatively, lowland rice, also called submergence-tolerant rice, becomes quiescent upon submergence and conserves carbohydrate energy to wait for the water to recede. This response is mediated by the ERF SUBMERGENCE1A (Sub1A) (Xu et al. 2006). This is also the strategy used by *Arabidopsis thaliana (Bailey-Serres et al. 2012)*. Note that these induced responses differ from permanent adaptations such as those found in aquatic and wetland plants. As an example, wetlands plants have submerged roots with shoots exposed to air. They avoid hypoxia in submerged tissues with the help of internal air

channels called aerenchyma, which extend through their leaves, stems, and roots. These channels act like a snorkel and provide a means of gas exchange between the tissues above and below the water (Sculthorpe 1967).

1.2.3 Calcium signaling during hypoxia

Calcium signaling is used by all eukaryotes, and the general mechanism is well conserved. Calcium functions as a second messenger because the resting cytosolic concentrations are maintained 20,000-fold lower than extracellular and organellar concentrations (100-200 nM in plant cells at rest (Virdi et al. 2015) vs 1-5 µM when stimulated (Clapham 2007). This steep gradient is needed because elevated calcium can bind phosphate and precipitate, which becomes toxic for phosphate-based energy metabolism (Virdi et al. 2015). Calcium efflux from the cytosol is accomplished by Ca^{2+}/H^{+} antiporters and Ca^{2+}-ATPase pumps (Clapham 2007), which are always active (Bender et al. 2013). Regulated Ca^{2+} channels allow influx from the ER, vacuole or extracellular spaces down the concentration gradient (Cai et al. 2015). A calcium signal occurs when influx exceeds efflux, which can occur cell-wide or can be localized at specific membrane sites (Bender et al. 2013). Transient elevations in cytosolic Ca^{2+} triggers Ca^{2+}-binding by calmodulins (CaM) and related EF-hand calcium-binding proteins, which act as sensors for the calcium second messenger. Ca^{2+}-bound calmodulin then bind and activate downstream targets, orchestrating a cellular response (Clapham 2007). Calcium signals are transient bursts of cytosolic calcium that is quickly removed, but there is a great deal of complexity that can be encoded in these signals (Yuan et al. 2017). The frequency, amplitude, and distribution throughout the cell all

contribute to a so-called “calcium signature,” which can determine the subset of EF-hand proteins which are activated, or can influence their downstream response (Yuan et al. 2017). In plant microbe interactions, when microbes interact with plant pattern recognition receptors on the cell surface, they produce a characteristic calcium signaling signature which can distinguish one bacterial species from another (Yuan et al. 2017). In abiotic stress, the same variables are at play, with frequency, amplitude and spatial distribution encoding information about the stress (Yuan et al. 2017). The existence of these signatures complicates the study of calcium sensing proteins, since not all calcium signals are the same.

Plant hypoxia responses involve complex changes in calcium signaling. Early experiments with the calcium channel blocker, ruthenium red (RR), which inhibits calcium signaling, demonstrated that calcium is part of the plant hypoxia response (Subbaiah et al. 1994). In these initial experiments, maize suspension-cultured cells showed an increase in cytosolic calcium concentration following exposure to anoxia, as reported by a fluorescent calcium probe, Fluo-3 AM. This calcium influx was blocked by RR, which suggested that the mobilization of calcium from intracellular stores were involved. Further, RR treatment also prevented the downstream upregulating of fermentation genes, including alcohol dehydrogenase, indicating that a calcium signal is necessary for the genetic response. (Subbaiah et al. 1994). This is supported by the observation that RR-treated maize seedlings showed poorer survival following anoxia treatment (Subbaiah et al. 1994).

Gross changes in cytosolic calcium concentrations throughout the course of a hypoxia treatment and recovery have been examined in Arabidopsis seedlings by using genetically engineered reporter plants (Sedbrook et al. 1996). The study used transgenic Arabidopsis seedlings expressing aequorin, a protein which luminesces upon binding to Ca^{2+} in the presence of a co-factor (Sedbrook et al. 1996). Observations with the plants show that the onset of hypoxia is marked with a sharp influx of calcium into the cytosol, which gives way to sustained lower-amplitude calcium signals as hypoxia continues. During the recovery phase, reoxygenation first involves a transient drop in calcium levels, followed by a large elevation before returning to resting levels (Sedbrook et al. 1996). This study provided the significant insight that calcium shows dynamic responses at every stage of hypoxia, and likely evokes different responses perhaps through different pathways and different sensors at each phase. A detailed understanding of calcium signaling during a hypoxia time course is still lacking at the cellular level.

The molecular mechanisms regarding how calcium is sensed and transduced into responses during these various phases of the hypoxia/flooding response and recovery is not clear. Key to understanding such mechanisms is the identity of the calcium sensor proteins involved in the response, and their downstream targets. Insight into one such calmodulin-like protein in Arabidopsis comes from Calmodulin-like 38 (CML38), which plays an important role during hypoxia (Lokdarshi et al. 2016). In the next section, I review the biochemical and physiological features of calmodulins and a specialized class of calmodulin-like proteins which are related to “regulator of gene silencing calmodulins,” including Arabidopsis CML38.

1.3 Arabidopsis Calmodulin-like 38 is a hypoxia-induced calcium sensor protein necessary for low oxygen stress survival

Calmodulin (CaM) is the archetypal calcium-sensing protein that is ubiquitous in all eukaryotic cells (Popescu et al. 2007). Its canonical function is to detect the Ca^{2+} second messenger, become active, and then bind and activate downstream targets (Clapham 2007). Calmodulin is a dumbbell-shaped protein consisting of N-terminal and C-terminal lobes that cooperatively binds four Ca^{2+} atoms, one in each of its four "EF-hand" domains. The EF-hands are helix-loop-helix domains which bind a Ca^{2+} atom in a conserved 12 amino acid loop using seven coordinating interactions provided by oxygen atoms: six from acidic amino acid side chains (with one sometimes coming from a coordinated water molecule) (Clapham 2007), and one from a backbone carbonyl oxygen (Biekofsky et al. 1998). When calmodulin is in its apo-state, without calcium bound, it has a closed conformation (Clapham 2007). After Ca^{2+} binding, hydrophobic residues become exposed in its amino and carboxyl lobes, facilitating target interactions. Active Ca^{2+}CaM can then bind target proteins, usually leading to activation by disruption of an auto-inhibitory domain on the target (Clapham 2007). Calmodulins play physiologically critical roles. They bind and activate a wide range of intracellular target proteins such as protein phosphatases, kinases, transcription factors and many others. intracellular proteins such as kinases, transcription factors and many others. The mechanism of calmodulin calcium binding and activation is highly conserved across all kingdoms of life, and its specific biological function in a cell is determined by the collection of CaM target proteins (Clapham 2007).

In contrast to the canonical mechanism of CaM-binding and target activation, there are some well-known examples in which a calmodulin binds a target protein in a calcium-independent manner, and dissociates once calcium levels rise, activating the target (Rhoads et al. 1997, Chin et al. 2000). This is the case for calmodulin binding to isoleucine, glutamine (IQ) domains of human neuromodulin, as well as several unconventional myosins (Rhoads et al. 1997).

In addition to the true calmlodulins, there are numerous related proteins called calmodulin-like proteins (CMLs). CMLs diverge from CaMs in either their number of EF-hand domains, the addition of regulatory elements or additional domains, their expression patterns or target specificity (McCormack et al. 2003). CMLs are also much more divergent than CaMs with respect to sequence identity. While all vertebrate CaMs are >90 identical, Arabidopsis CaMs are all >99% identical to At-CaM2 (McCormack et al. 2003). In contrast, Arabidopsis CMLs share 16 to 75% identity to At-CaM2 (McCormack et al. 2003). The CaMs and CMLs of Arabidopsis phylogenetically cluster into nine clades (groups 1-9) (McCormack et al. 2003). Group 1 represents the CaMs (McCormack et al. 2003), and group six, which will be discussed later, is the clade containing the regulator of gene silencing calmodulins. While CaMs do not exhibit much transcriptional change in response to stimuli, most Arabidopsis CMLs (35 out of 50) show a >5-fold induction by one or more stress treatments (McCormack et al. 2005).

A microarray experiment to identify Arabidopsis transcripts showing significant up- or down-regulation in response to hypoxia was conducted. (Choi 2009) (Lokdarshi et al. 2016). In these findings, *CML38* mRNA was found to have >600-fold upregulation

in response to 4 hours of anoxia. Notably, this was the only calmodulin-like protein to show upregulation. Lokdarshi et al. subsequently confirmed this up-regulation using quantitative real-time PCR (qPCR) (Lokdarshi et al. 2016). In this experiment, 10-day old Arabidopsis seedlings were subjected to hypoxia by displacing air with argon. qPCR results showed that *CML38* had a near-linear increase in mRNA accumulation and reached a maximum between 4-6 hours. The roots showed an approximate 350-fold increase in transcript levels at 6 hours, this declined to ~100-fold at 8 hours, and slowly declined to ~50-fold by 24 hours of hypoxia. In contrast, the shoots showed a maximum accumulation of ~100-fold at 4 hours, and this fell to ~75-fold at 6 hours and remained between 75-25-fold through to 24 hours. This analysis was also performed on *CML39* (At1g76640), which is a closely related (76% protein identity) tandem gene (Lokdarshi et al. 2016). In contrast, *CML39* showed a relatively small ~5-fold increase in mRNA accumulation in response to the hypoxia (Lokdarshi et al. 2016). Analysis of the other CMLs and calmodulin by microarray confirmed that CML38 is the only calcium sensor that responds to low oxygen stress. Moreover, translatome analysis by Mustroph et al. showed that CML38 is readily associated with translating polysomes, and it was designated one of the 49 core hypoxia response genes, and is the only EF hand protein within this collection (Mustroph et al. 2009).

CML38 protein also accumulates during hypoxia based on the analysis of a *CML38*-3xYFP recombineering line driven by the native promoter (Lokdarshi et al. 2016). In this technique, a bacterial artificial chromosome is used that contains the *CML38* gene along with upstream promoter elements, in the context of ~60 kb of the chromosome (Lokdarshi et al. 2016). Recombination was used to introduce the 3xYFP

sequence (Zhou et al. 2011) in-frame at the 3' end of the *CML38* coding sequence (Lokdarshi et al. 2016). Western blotting against the YFP tag was used to identify that CML38 protein reaches maximal levels between 6-8 hours and persists through the 20-hour time course (Lokdarshi et al. 2016).

Subsequent analysis of *cml38* T-DNA mutant plants revealed that they showed poorer survival to argon-induced low oxygen stress (Lokdarshi et al. 2016). This study showed that *CML38* is a hypoxia-induced calcium sensor that is needed for optimal survival following hypoxia treatment (Lokdarshi et al. 2016). In the next section, the relationship of CML38 to a subclass of calcium sensors known as the "regulator of gene silencing" calmodulins (rgsCaMs) is discussed.

1.4 Regulator of Gene Silencing Calmodulins

1.4.1 Antiviral gene-silencing in plants

Gene silencing consists of two major types: post-transcriptional gene-silencing (PTGS) and transcriptional gene silencing (TGS) (Pumplin et al. 2013). While PTGS targets mRNA or viral RNA for degradation or translational repression, TGS targets DNA to block transcription via epigenetic modification such as methylation, and can target endogenous genes as well as the genomes of DNA viruses (Pumplin et al. 2013). Most of the work with rgsCaM has been in the context of RNA silencing (Anandalakshmi et al. 2000, Nakahara et al. 2012, Li et al. 2014, Nakamura et al. 2014, Li et al. 2017), with some evidence that this can influence RNA splicing (Shin et al. 2014). However, rgsCaM-like proteins are also actively being studied in the context of the DNA

Geminiviruses (Yong Chung et al. 2014, Li et al. 2017), against-which TGS is an important defense (Yong Chung et al. 2014). Both PTGS and TGS will be discussed.

RNA silencing (or RNA interference) consists of the recognition of double-stranded RNA, its cleavage into small non-coding RNAs (smRNAs) and subsequent use to target complementary RNA substrates for either cleavage (leading to degradation) or translational repression (Pumplin et al. 2013, Borges et al. 2015). Silencing is widely believed to have evolved as a defense response to RNA viruses (Pumplin et al. 2013). dsRNA binding proteins of silencing pathways can target the dsRNA of viral replication intermediates or their regulatory imperfect hairpin regions (Pumplin et al. 2013, Bologna et al. 2014). Before describing the types of smRNAs in plants, and the RNA silencing pathways, three major enzymes of these processes will be discussed: Dicers, argonautes and RNA-dependent RNA polymerases (RDRs).

The initial cleavage of dsRNA, “dicing,” is performed by DICER-LIKE proteins (DCLs) (Borges et al. 2015). DCLs contain a dsRNA binding domain and a ribonuclease III domain for the cleavage of both RNA strands (Borges et al. 2015). Additionally, many DCLs contain DExD box helicase domains for RNA remodeling, and PIWI/ARGONAUTE/ZWILLE (PAZ) domains for binding 3’ overhangs on dsRNA. DCLs determine the length of the smRNA product, which is typically 20-24 nucleotides (Borges et al. 2015). There are four DCL enzymes in Arabidopsis, DCL1 through DCL4, and each has specificities for a subset of dsRNA substrates, and produces smRNAs of specific lengths which, in turn, can selectively be incorporated into different ARGONAUTE proteins (AGOs) (Wang et al. 2011). While dicing does inactivate its

target, dicing alone is not sufficient to protect plants from RNA viruses, for this, AGO activity is also needed (Wang et al. 2011). The smRNA products of dicing are called "primary smRNAs," since they are produced from the original RNA substrate without additional RNA synthesis (Bologna et al. 2014).

Double-stranded smRNAs are sorted into AGO proteins and used to identify complementary mRNAs for cleavage or translational repression (Pumplin et al. 2013). Arabidopsis has 10 AGO genes which bind smRNAs (Pumplin et al. 2013). The bias by which AGOs select smRNAs is based on the identity of the 5' nucleotide and the sequence length (Pumplin et al. 2013). Once bound by an AGO, one of the smRNA strands is selected to remain while the other is degraded. DCL products contain a two-nucleotide 5' overhang on each strand (Siomi et al. 2009). The 5' overhang which resides at the smRNA side with the lower thermodynamic stability stays associated with the AGO as the "guide strand," while the other strand, the "passenger strand," is degraded by AGO-associated proteins (Schwarz et al. 2003, Siomi et al. 2009). AGOs are part of a ribonucloprotein (RNP) complex called the RNA-induced silencing complex (RISC) (Siomi et al. 2009). To distinguish this AGO-catalyzed cleavage from that of DCLs (dicing), this is referred to as "slicing" (Pumplin et al. 2013).

RNA-dependent RNA polymerases (RDRs) are employed in some silencing pathways to synthesize the complementary strand of a target RNA prior to dicing (Willmann et al. 2011). This is advantageous because it allows the entire sequence of a target RNA to be used to produce smRNAs, even if the target RNA only has a short region that is double-stranded. Arabidopsis has six RDRs, named RDR1 through RDR6

(Willmann et al. 2011). Evolution has led to duplications and diversification of DCLs, AGOs and RDRs, and has led to multiple, overlapping silencing pathways that can target a variety of exogenous and endogenous RNAs (Borges et al. 2015).

Micro-RNAs are the primary means by which PTGS is used to regulate endogenous gene expression in plants and animals. In Arabidopsis, miRNA genes are transcribed as long and imperfect stem-loop structures called primary-miRNAs (Lelandais-Briere et al. 2009). The dsRNA regions of a primary-miRNA are diced by DCL1 producing pre-miRNA. DCL1 then further cleaves pre-miRNA into 21 nucleotide double-stranded miRNAs. To stabilize these miRNAs, the 2'OH of the 5' ends are methylated by HUA ENHANCER 1 (HEN1). Stabilized miRNA is shuttled out of the nucleus by HASTY. In the cytoplasm, miRNAs associate with AGO1 as part of the RISC complex. The guide miRNA is selected as described previously, selecting the strand which has its 5' end on the side with lower thermodynamic stability. The miRNA then guides the RISC complex to complementary RNA, typically an mRNA. Upon binding, the target RNA molecule is either cleaved by AGO1 as the first step in RNA degradation, or it is translationally inhibited (Lelandais-Briere et al. 2009).

Trans-acting siRNAs (tasiRNAs) are a plant-specific class of siRNAs (Bologna et al. 2014). tasiRNAs are encoded as pri-tasiRNAs from non-coding loci. There are eight recognized loci for tasi-RNA genes (TAS genes) in Arabidopsis (Bologna et al. 2014), falling into four families (Borges et al. 2015), and TAS genes have been found in several plant species, including mosses (Bologna et al. 2014), but apparently not in other kingdoms. Similar to mRNA, these pri-tasiRNAs are transcribed by RNA polymerase II,

capped and polyadenylated (Bologna et al. 2014). These transcripts are not self-complimentary like primary-miRNA. Rather, pri-tasiRNAs are targeted by a sequence-specific miRNA. (Bologna et al. 2014).

There are two pathways for tasiRNA biogenesis, but both ultimately cleave much of the pri-tasiRNA into 21-nt tasiRNAs along predetermined (phased) cut sites. In the "one hit pathway," a single miRNA in association with AGO1 binds and cleaves the pri-tasiRNA at the 5' end of the miRNA recognition site. The 5' cleavage product of the pri-tasiRNA is degraded, while the 3' cleavage product is protected from degradation by suppressor of gene silencing 3 (SGS3), which forms a complex with the miRNA-containing AGO1. RDR6 then synthesizes the second RNA strand (Bologna et al. 2014). The dsRNA is cleaved into 21-nt tasiRNAs by DCL4, which requires the RNA-binding protein DRB4 (Adenot et al. 2006), starting from the miRNA binding site through to the end of the molecule (Bologna et al. 2014). In the "two hit pathway," AGO7 loaded with miR390 binds to two distinct binding sites within its target pri-tasiRNA, but cleavage only occurs at the 3' end of the binding site nearer the 3' end of the molecule (Bologna et al. 2014). The 5' cleavage product is then processed by DCL4 into 21-nt tasiRNAs as in the "one hit pathway" (Bologna et al. 2014). The cleavage positions of all the resulting tasiRNAs are reliably determined by the initial cleavage at the miRNA site (Bologna et al. 2014). It has also been reported that DCL2 is also active here and produces 22-nt tasiRNAs (Borges et al. 2015). Compared to miRNAs, a tasiRNA often targets entire gene families. siRNAs generated following RDR6 amplification also have much more cell-to-cell mobility through plasmodesmata than miRNAs (Bologna et al. 2014). For instance, the TAS3 tasiRNA behaves like a morphogen, creating a gradient throughout

the leaf which controls auxin-response factor (ARF) expression, helping to establish the abaxial-adaxial leaf polarization (Bologna et al. 2014). As with miRNAs, secondary siRNAs are stabilized by methylation at the 5' end (Bologna et al. 2014).

The mechanism by which secondary viral siRNAs (vsiRNAs) are produced is thought to be closely related to the latter part of the tasiRNA biogenesis pathway (after miRNA-induced cleavage). RDR6 and SGS3 are required for second strand RNA synthesis, and DCL4/DRB4 and DCL2 cleave to produce 21 and 22-nt vsiRNAs (Figure 1) (Pumplin et al. 2013, Borges et al. 2015). As with tasiRNAs, secondary vsiRNAs are similarly mobile cell-to-cell and are thought to be involved as messengers of systemic silencing. In contrast, the primary vsiRNAs, produced directly from dicing viral RNA (without RDR6 amplification), are more involved in silencing within an infected cell (Pumplin et al. 2013).

Sense-transgene silencing is another important example of a secondary siRNA overlapping with tasiRNAs and vsiRNAs. Transgene silencing does not require self-complementation. Rather, it is proposed that accumulation of aberrant RNA (lacking capping or polyadenylation), especially in cases of overexpression, escapes the RNA quality control mechanisms and are instead acted upon by RDR6/SGS3 (Liu et al. 2016). The action of RDR6 produces dsRNA precursors for siRNA production via dicing. The resulting siRNAs would lead to PTGS of the transgene.

The collection of other major types of siRNAs will be briefly discussed. Hairpin siRNAs (Inverted-repeat RNAs) are derived from endogenous RNA polymerase II-transcribed mRNAs that contain internal complementary sequences that form secondary

structure (Borges et al. 2015). These can be recognized by any of the four DICER-LIKE protein of Arabidopsis, and produce siRNAs of 21-24-nt. These hairpin RNAs have longer hairpins than pri-miRNAs, and do not have the imperfections in complementarity which are characteristic of miRNAs (Borges et al. 2015). Natural-antisense siRNAs (natsiRNAs) are another type of secondary siRNA. natsiRNAs are produced from two complementary transcripts which hybridize (Borges et al. 2015). These can originate from different loci, or from transcription of a single locus in both directions (Borges et al. 2015). It is proposed that precursor transcripts for natsiRNAs are acted on by RDR6 and RDR2, and subsequently diced by DCL1, DCL2, and DCL3 (Borges et al. 2015). Heterochromatic siRNAs (hetsiRNAs) are more distinct and direct RNA-directed DNA methylation (RdDM) to a gene locus for transcriptional gene silencing (Borges et al. 2015). RNA polymerase IV is a plant-specific isoenzyme which is recruited to transcribe the DNA locus which will be silenced. RDR2 synthesizes the second strand, and DCL3 cleaves it into 24-nt hetsiRNAs (Borges et al. 2015). hetsiRNAs are incorporated into AGO4-containing RISC complexes, which target nascent transcripts by RNA polymerase V from the same DNA locus (Borges et al. 2015). It is proposed that AGO4 (possibly with some redundancy with AGO6 and AGO9) recruits DOMAINS REARRANGED METHYTRANSFERASE 2 (DRM2), which methylates cytosines at CpG islands resulting in promoter silencing (Borges et al. 2015). Subsequent recruitment of chromatin remodeling factors including histone deacetylase would transcriptionally silence the region in heterochromatin (Borges et al. 2015). Epigenetically activated siRNAs (easiRNAs) are similar to hetsiRNAs, but are produced from active retrotransposons

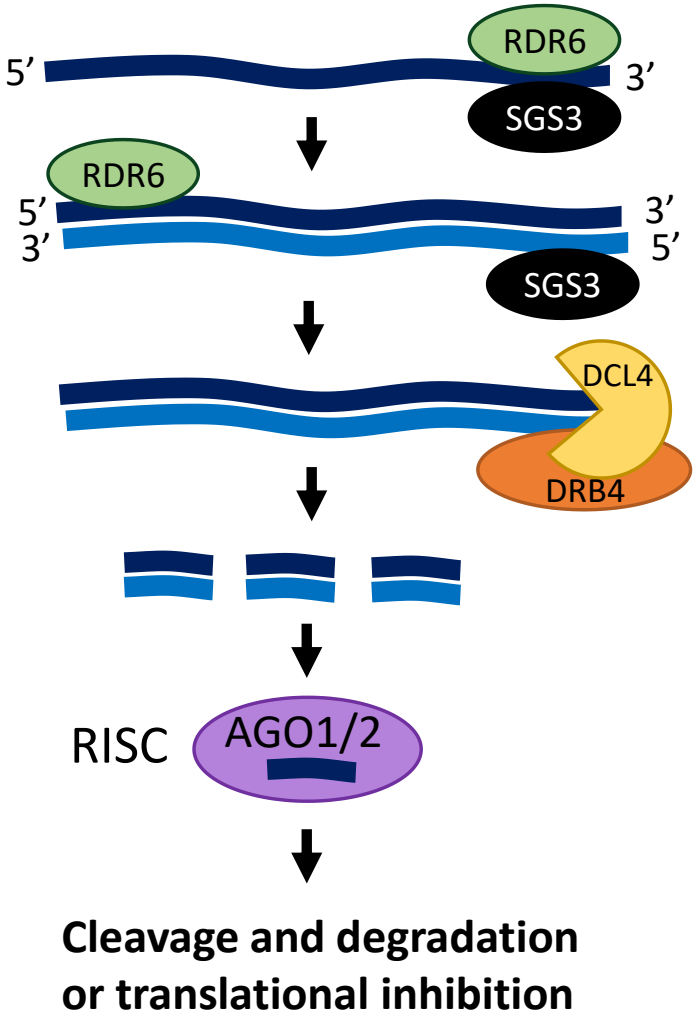

Figure 1 Shared components of trans-acting siRNA and secondary viral siRNA biosynthesis and sense-transgene silencing. Suppressor of gene silencing 3 (SGS3) and RNA-dependent RNA polymerase 6 (RDR6) cooperatively synthesize the second strand of the target RNA. Dicer-like 4 and dsRNA-binding protein 4 (DRB4) cooperatively cleave the dsRNA into 21-22nt siRNAs. One strand is selected for incorporation into argonaute 1 or 2 of the RNA-induced silencing complex (RISC) for targeting complementary RNA for cleavage and degradation or translational repression.

transcribed by RNA polymerase IV (Martinez et al. 2018). easiRNAs are responsible for silencing transposons to promote genomic stability (Martinez et al. 2018).

1.4.2 Regulator of gene silencing CaMs as targets for viral suppressors of gene silencing

rgsCaM was discovered in a yeast two-hybrid screen aimed at identifying endogenous *N. tabacum* proteins that interact with the *tobacco etch* potyvirus protein "helper component proteinase" (HC-Pro) (Anandalakshmi et al. 2000). HC-Pro was previously identified as a viral suppressor of gene silencing (Anandalakshmi et al. 1998). Subsequent analysis revealed that overexpression of rgsCaM could prevent or reverse virus-induced gene silencing (VIGS) and transgene silencing (Anandalakshmi et al. 2000). This was demonstrated using an *N. benthamiana* GFP-expressing line with and without constitutive expression of rgsCaM (Anandalakshmi et al. 2000). Both lines were infected with a potato virus X-GFP (PVX-GFP) VIGS construct. In this assay, the modified virus contains part of the GFP nucleotide sequence, such that host silencing of the virus also results in silencing of the GFP transgene. Over the course of about three weeks, the infection spreads systemically, and then subsequently the plant establishes VIGS against PVX and the GFP transgene (Anandalakshmi et al. 2000). However, the GFP transgene did not become silenced in the line with constitutive rgsCaM expression, demonstrating that rgsCaM was sufficient to prevent VIGS (Anandalakshmi et al. 2000). A variation of this experiment showed that rgsCaM could also reverse VIGS (Anandalakshmi et al. 2000).

rgsCaM suppression of transgene silencing was also investigated (Anandalakshmi et al. 2000). Here, the GFP-expressing tobacco line was again silenced for GFP, but this time this was accomplished by transgene silencing rather than VIGS, by infiltrating the leaves with a plasmid expressing GFP. Within three weeks transgene silencing had occurred in the infiltrated area and spread throughout the plant (Anandalakshmi et al. 2000). Subsequent infiltration with PVX vectors containing either the normal HC-Pro suppressor of silencing, or one in which rgsCaM replaced HC-Pro, both resulted in reversal of the transgene silencing (Anandalakshmi et al. 2000). Since constitutive expression of rgsCaM prevents and reverses VIGS and transgene silencing, much like HC-Pro, it was proposed that HC-Pro may hijack the function of rgsCaM. Thus, rgsCaM was the first reported endogenous suppressor of gene silencing (Anandalakshmi et al. 2000).

The notion that HC-Pro works in part through rgsCaM was further supported by the discovery that transgenic expression of HC-Pro or infection with an HC-Pro-containing virus leads to the upregulation of rgsCaM (Anandalakshmi et al. 2000). Additionally, overexpression of either HC-Pro or rgsCaM generated the same developmental phenotype of a differentiated tumor at the root-shoot junction in *N. benthamiana*. These findings supported the hypothesis that HC-Pro suppresses silencing at least in part through activation of rgsCaM. Further, since rgsCaM is a calmodulin-like calcium sensor, it was proposed that this endogenous silencing suppression activity may be regulated by Ca^{2+} signals. In a subsequent study of rgsCaM from *N.* benthamiana, rgsCaM was found to directly interact with potyvirus HC-Pro and bromovirus 2b, a viral suppressor of gene silencing that is structurally unrelated to HC-

Pro (Nakahara et al. 2012). These findings suggest different viruses may have independently evolved to target rgsCaM.

Further analysis of rgsCaM suppression of silencing shows that it is specific for a subset of smRNA silencing pathways. rgsCaM can suppress pathways for VIGS (Anandalakshmi et al. 2000), tasiRNAs (Foreman 2012), and sense-transgene silencing (Li et al. 2014), but has no effect on miRNA silencing (Foreman 2012) or hairpin-siRNAs (Li et al. 2014). The commonality in rgsCaM-suppressed pathways is that these are all secondary siRNA pathways which require the production of dsRNA through the cooperative action of RDR6 and SGS3 (Pumplin et al. 2013). More specifically, rgsCaMs (Nb-rgsCaM) directly bind SGS3 and lead to the degradation of both SGS3 and RDR6 (Li et al. 2017). rgsCaM-mediated degradation of SGS3 would prevent the generation of transitive secondary siRNAs and prevent silencing.

1.4.3 rgsCaMs constitute a phylogenetic subclass of structurally related calcium-sensors and may have a common silencing suppression function

rgsCaM is structurally and functionally distinct from calmodulin. As compared to calmodulin, which has little sequence upstream of its first EF hand, rgsCaM has a 50-amino acid N-terminal extension (Figure 2). Another key difference is that of the four ancestral EF hands within the canonical calmodulin domain, EF3 of rgsCaM has substitutions which strongly suggest that it would be incapable of binding calcium (Anandalakshmi et al. 2000) (Lokdarshi et al. 2016). Arabidopsis has four (Lokdarshi et al. 2016) or five (McCormack et al. 2003) rgsCaM-like (rgsCML) encoding genes which cluster within a phylogenetic clade with rgsCaM (Figure 2). These consist of CMLs 37,

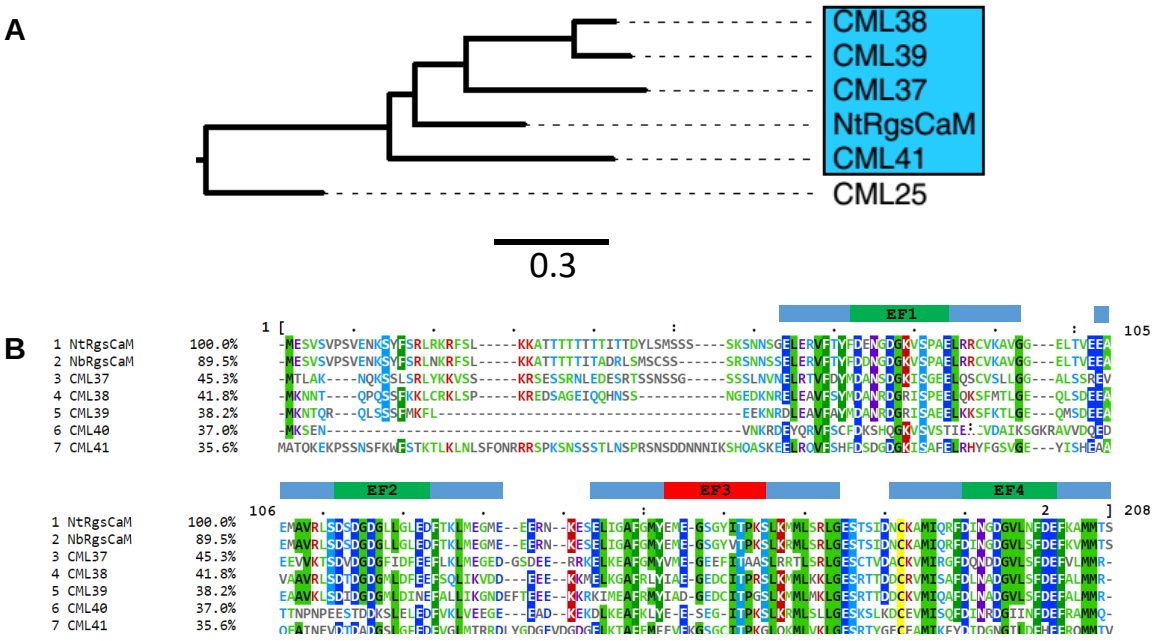

Figure 2 Phylogenetic tree and multiple sequence alignment of rgsCaM-like proteins in Arabidopsis and tobacco. **A)** Abbreviated phylogenetic tree showing the A. thaliana rgsCaM-like clade (CML37, CML38, CML39 and CML41) alongside rgsCaM from *N. tabacum*. CML25 is shown as a single outlier. The scale bar shows the length f the branches that corresponds to 0.3% amino acid sequence divergence. See results section (Figure 5) for complete tree. **B)** Multiple sequence alignment of At-rgsCMLs and Nt-rgsCaM and Nb-rgsCaM. EF hands are indicated with the E and F helices shown in blue, flanking the calcium binding loop in green, or in red for the site of disrupted calcium binding loops of EF3 for the members of this clade. Alignment was performed using the MUSCLE algorithm and visualization is by Mview (www.ebi.ac.uk). Color code indicates amino acid chemical properties. Percent sequence identity relative to Nt-rgsCaM is shown following the sequence name.

38, 39 and 41, but in an earlier multiple sequence alignment CML40 clustered here as well (McCormack et al. 2005). The predicted disrupted third EF hand domain of CML38 was investigated with homology modeling based on a crystal structure of calcium-bound *bona fide* calmodulin as a template structure (Lokdarshi et al. 2016). This work identified four disruptive amino acid substitutions of the calcium-binding loop of CML38. Ile87, Glu91, and Ser98 are in conserved positions of the EF hand that contribute oxygens to make contacts with calcium, but the model illustrates that these these substituted residues do not do so. There is also a substitution of the conserved glycine which contributes flexibility of the loop backbone with a bulky side chain (Asp92) (Lokdarshi et al. 2016). The phylogenetic similarity of rgsCaM to this Arabidopsis CML clade raises the possibility that CML38 and related CMLs share functional similarities to rgsCaM (Lokdarshi et al., 2016).

In support of this conserved function, rgsCaM homologs in *N*. *benthamiana* (Li et al. 2014, Li et al. 2017) and Arabidopsis (CML38 (Endres et al. 2010) and CML39 (Yong Chung et al. 2014) exhibit some of the properties of tobacco rgsCaM. In *N. benthamiana,* a study involving the Geminivirus Tomato yellow leaf curl China virus and its suppressor of silencing βC1 (Li et al. 2014) found strikingly similar results as earlier studies with TEV and HC-Pro (Anandalakshmi et al. 2000). It was found that virus infection upregulated rgsCaM mRNA levels by 10-fold, and transgenic expression of βC1 increased by 25-fold (Li et al. 2014). As with HC-Pro expression (Anandalakshmi et al. 2000), transgenic expression of βC1 also produced a developmental phenotype (leaf curling), a result which was phenocopied in constitutive rgsCaM expressing lines (*35S:rgsCaM*) (Li et al. 2014). An *N. benthamiana* rgsCaM RNA interference (RNAi) line

(expressing a double-stranded portion of rgsCaM) reduced mRNA accumulation to approximately 20% of wt. Consistent with a role as a suppressor of RNA silencing, relative to wt plants, constitutive rgsCaM expression greatly suppressed silencing in a VIGS assay and increases virus susceptibility, while rgsCaM RNAi elevated silencing and reduced virus susceptibility (Li et al. 2014). These findings are significant since they identify that the point of action for rgsCaM is likely something which is shared between highly divergent RNA and DNA viruses. CML39 also interacts with a viral suppressor of silencing, AL2 from a DNA-genome Geminivirus Tomato golden mosaic virus (TGMV) (Yong Chung et al. 2014). *CML39* promoter activity is mildly upregulated (1.39 fold) by AL2 from TGMV, and CML39 interacts directly with AL2 (Yong Chung et al. 2014). Additionally, CML39 was shown to self-interact by BiFC in the cytosol, but BiFC complexes of CML39 and AL2 were seen exclusively within nuclear puncta (Yong Chung et al. 2014). Consistent with the proposed role for rgsCMLs as a target and effector for viral suppressors of silencing, *CML39* overexpression lines exhibited enhanced infectivity, and knockouts had reduced infectivity to the TGMV Geminivirus. The authors propose that AL2 may sequester CML39 in the nucleus to prevent AL2 from being degraded by autophagy. This proposal was based on findings from another publication which had shown that tobacco rgsCaM targets HC-Pro for degradation by autophagy (Nakahara et al. 2012), which is a cytosolic process (Stolz et al. 2014). It is not clear whether all members of the rgsCaM clade participate in RNA silencing and RNA regulation, and whether a connection to autophagic regulation is at play in each case.

The evidence connecting CML38 to gene silencing activities is less clear, but Endres *et al*. (2010) showed that transgenic plants that express potyviral HC-Pro also

show upregulated *CML38* (Endres et al. 2010), as was previously shown for rgsCaM (Anandalakshmi et al. 2000). It was further shown that this upregulation required the ethylene-inducible transcription factor RELATED TO ABI3/VP1 2 (RAV2) (Endres et al. 2010).

1.5 Hypoxia stress induces a global inhibition of translational initiation

Although plants have unique adaptive responses to a wide variety of stresses, one common response in both abiotic and biotic stresses is to broadly inhibit translational initiation of most genes, so that stress-induced transcripts and those involved in homeostasis are preferentially translated (Echevarria-Zomeno et al. 2013). This allows stressed cells to suspend unnecessary protein translation, which is a highly energy-consuming process (Echevarria-Zomeno et al. 2013), and focus only on making gene products that enhance survival (Echevarria-Zomeno et al. 2013).

1.5.1. Mechanism of translational inhibition in plants

In mammals, this stress-induced repression of translational initiation is primarily mediated by two ways. First, the eukaryotic initiation factor 2α (eIF2α) can be phosphorylated by protein kinase R (PKR) or general control nonderepressible 2 (GCN2) kinase (Kimball et al. 2003). Second, eukaryotic initiation factor 4e (eIF4e) can be bound by its inhibitory binding proteins (4eBPs), which is preceded by stress-induced dephosphorylation of 4eBPs (Echevarria-Zomeno et al. 2013). The mechanisms of translational inhibition in plants are emerging. eIF2α does get phosphorylated in plants by a GCN2 homolog in response to some abiotic stresses (nutrient deprivation, wounding, UV light), but GCN2 is not the kinase doing the job in some other stresses

(heat shock, NaCl, and H_2O_2) (Echevarria-Zomeno et al. 2013) (Sesma et al. 2017). A PKR homolog in plants has not been identified, but the PKR inhibitor is present (Echevarria-Zomeno et al. 2013). If the PKR inhibitor in plants is silenced, eIF2α becomes phosphorylated and unstressed plants die, suggesting this mechanism is present and is a critical regulator of translation, although the specific kinase involved here is unknown (Echevarria-Zomeno et al. 2013). The target of rapamycin (TOR) kinase is involved in the positive regulation of global translation, but the specific mechanism is not established (Sesma et al. 2017).

1.5.2 The RNA cycle: Stress granules and Processing bodies

Inhibition of translational initiation causes formation of stress-induced mRNP bodies called stress granules (SGs). When translational initiation is arrested, translating ribosomes “run-off” the mRNA, leaving only the 48S pre-initiation complex (small ribosomal subunit and eukaryotic initiation factors) on an otherwise exposed mRNA (Khong et al. 2018). Exposed RNA in both plants and mammals are bound by RNA binding proteins containing triple RNA recognition motifs (RRMs) (Bailey-Serres et al. 2009, Sorenson et al. 2014). These proteins effectively cross-link the mRNAs with stalled initiation and cause aggregation and the nucleation of stress granules (SGs) (Bailey-Serres et al. 2009, Sorenson et al. 2014). In mammals, the RRM protein is TIA-1 (Kimball et al. 2003), while UBP1 and RBP47 serve these roles in plants (Weber et al. 2008, Sorenson et al. 2014). SGs can form within minutes after the onset of a stress treatment and can similarly dissipate once the stress is removed (Sorenson et al. 2014, Protter et al. 2016). Despite stress-induced translational repression, stress related

transcripts remain translationally active are not bound by RRM proteins. The mechanism by which these transcripts undergo translational initiation under these conditions is not entirely clear (Echevarria-Zomeno et al. 2013).

Structurally, SGs are non-membrane enclosed heterologous structures with relatively stable cores and shells which are highly dynamic, liquid-like phase separations from the cytosol showing rapid exchange of material (Protter et al. 2016). SGs range in size from 0.1 nm to 2 μm (Kedersha et al. 2009). In addition to the RRM nucleating proteins, numerous other proteins localize to stress granules, such as chaperones, metabolic enzymes and proteins involved in cell signaling (Samaha et al. 2010, Isabelle et al. 2012, Sorenson et al. 2014, Protter et al. 2016).

Stress granules (SG) are sorting sites for non-translating mRNAs. The mRNAs in SGs can be held, transferred for degradation, or released back to resume translation if translational repression is alleviated (Sorenson et al. 2014). mRNAs which are sorted for degradation must first be transferred to another type of mRNP body, the mRNA processing bodies (PBs). This is thought to occur through stress granule docking onto processing bodies, which can be seen by fluorescence microscopy (Kedersha et al. 2005, Protter et al. 2016).

Stress granules are in dynamic equilibrium with polysomes and processing bodies (Kedersha et al. 2005, Protter et al. 2016, Chantarachot et al. 2018), and there is significant overlap in the proteins which reside in these structures. However, processing bodies are distinct in their enrichment for proteins relating to mRNA degradation and miRNA gene silencing (Chantarachot et al. 2018). While the mRNA in SGs is intact, the

mRNA found in PBs can be stable or acted upon by enzymes that remove the 5' cap and poly-A tail (Weber et al. 2008), as well as exoribonucleases for degrading mRNAs. Among these enzymes, four are commonly used as PB markers in plants. DECAPPING PROTEIN 1 and 2 (DCP1, DCP2) form the decapping complex along with the scaffold protein VARICOSE. Exoribonuclease 4 (XRN4), the plant homolog of mammalian XRN1, is an exoribonuclease of the 5' to 3' RNA degradation pathway (Chantarachot et al. 2018). Unlike SGs, PBs are also found in unstressed cells, since mRNA degradation is a constitutive process, but they also show a pronounced increase in their size and number during stresses such as heat shock and treatment with inhibitors of translation, both of which lead to increased mRNA degradation (Weber et al. 2008).

1.6. Goals of research

The goals of this project were to gain insight into how the rgsCaM-like family of calmodulin-like proteins regulate the mRNP cycle under cellular stress. We wanted to better understand how CML38 functions under hypoxia, and how rgsCaM functions to suppress silencing during viral infection, by testing a combined hypothesis which can explain both of these functions. This hypothesis draws from our knowledge of CML38 as an mRNP-localizing protein under stress conditions, and available information on rgsCaM as a virus-induced protein which targets and degrades binding partners through autophagy. We hypothesized that both homologs function by targeting mRNP particles for autophagic degradation (granulophagy) in response to stress-induced calcium signals. CML38 degradation of mRNPs under the hypoxia energy crisis would help plants survive by recycling unneeded material, and since rgsCaM interacts with proteins

involved in gene silencing, degradation of these mRNPs could also explain the suppression of silencing. We began with a cell biological approach to investigate rgsCaM mRNP localizations. With some bioinformatics indicating that these proteins contain a putative domain for binding autophagosomes, we tested for direct interaction between rgsCaM and the autophagosome protein ATG8e. Direct interaction between rgsCaM and ATG8e would indicate that rgsCaM functions as an autophagy cargo adaptor, serving as a link between its mRNP cargo and the autophagosome.

Chapter 2: Materials and Methods

2.1 Molecular cloning techniques and procedures

2.1.1 Generation of fluorescent protein fusions for co-localization experiments.

Coding sequences for proteins used in localization studies were amplified from complementary DNA (cDNA) or from existing clones. cDNA was generated with the SuperScript III first strand cDNA synthesis system (ThermoFisher), according to manufacturer's protocol, using total RNA from 1-2-week-old *Arabidopsis thaliana* Col-0, or *N. tabacum* seedlings. The open reading frames (ORF) were amplified with gene specific primers which incorporate all or a portion of the *attB1* and *attB2* recombination sites on the 5' and 3' ends. The recombination sites were either added in a single PCR reaction, or in a 2-step process, which used shorter gene-specific primers for the initial amplification, and then universal *attB1* or *attB2* primers to complete the recombination sites. The 2-step PCR procedure is described in detail in Lokdarshi et. al. (2016). For a complete list of primers and descriptions of their use see Table 1. Amplified PCR products were purified from agarose gels (Zymoclean Gel DNA Recovery kit, Zymo research, Irvine, California), then recombined with the Gateway-compatible donor vector pDONR207 in a BP clonase II (Invitrogen) reaction as previously described (Lokdarshi et al. 2016). Arabidopsis *ATG8e* was amplified from the pJ4GFP-XB GFP-AtATG8e plasmid (Contento et al. 2005). pDONR 207 constructs were selected on Luria Bertani (LB) agar plates supplemented with 50 µg/ml gentamycin. A representative map of pDONR 207 and an example of a donor construct containing *CML38* are shown in Figure 3.

Table 1 PCR primers for molecular cloning, mutagenesis and sequencing

Primer Name	Sequence	Use
Universal attB1 Fwd adaptor	GGGGACAAGTTTGTACAAAAAAGCAGGCT	Completing attB site for 2 PCR strategy
Universal attB2 Rev adaptor	GGGGACCACTTTGTACAAGAAAGCTGGGT	Completing attB site for 2 PCR strategy
Universal attB3 Rev adaptor	GGGGACAAGTTTGTATAATAAAGTTG	Completing attB site for 2 PCR strategy
Universal attB4 Rev adaptor	GGGGACAACTTTGTATAGAAAAGTTGGGT	Completing attB site for 2 PCR strategy
CaM2 attB1 Fwd	GGGGACAAGTTTGTACAAAAAAGCAGGCTTAATGGCGGATCAGCTCACAG	Making donor clone, 1 PCR
CaM2 No Stop attB2 Rev	GGGGACAACTTTGTACAAGAAAGCTGGGTTCTTAGCCATCATAACCTTCACAAACTC	Making donor clone, 1 PCR
NbRgsCaM attB1 Fwd	GGGGACAAGTTTGTA CAAAAAAGCAGGCTTA ATGGAATCGG TTTCTGTACC TAG	Making donor clone, 1 PCR
NbRgsCaM No stop attB2 Rev	GGGGACAACTTTGTA CAAGAAAGCTGGGTT ACTTGTCATCATAACTTTGAACTCATC	Making donor clone, 1 PCR
RgsCaM No Stop attB4	GGGGACAACTTTGTA TAGAAAAGTTGGGTG ACTTGTCATCATAGCTTTGAACTC	Making donor clone, 1 PCR
mScarlet attB1 Fwd	GGGGACAAGTTTGTACAAAAAAGCAGGCTTAATGGTGAGCAAGGGCGAG	Making donor clone, 1 PCRs
mScarlet attB2 Srop Rev	GGGGACAACTTTGTACAAGAAAGCTGGGTTTTTAAGATCTGTACAGCTCGTCCATG	Making donor clone, 1 PCRs
NBR1 attB1 Fwd	GGGGACAAGTTTGTACAAAAAAGCAGGCTTAATGGAGTCTACTGCTAACGCAC	Making donor clone, 1 PCRs
NBR1 attB1 Fwd	GGGGACAAGTTTGTACAAAAAAGCAGGCTTAATGGAGTCTACTGCTAACGCAC	Making donor clone, 1 PCRs
NBR1 attB2 No Stop Rev	GGGGACAACTTTGTACAAGAAAGCTGGGTTAGCCTCCTTCTCCCCTGTG	Making donor clone, 1 PCRs
NBR1 attB2 Stop Rev	GGGGACAACTTTGTACAAGAAAGCTGGGTTCTATTAAGCCTCCTTCTCCCCTGTG	Making donor clone, 1 PCRs
NBR1 attB3 Fwd	GGGGACAAGTTTGTATAATAAAGTTGTAATGGAGTCTACTGCTAACGCAC	Making donor clone, 1 PCRs
NBR1 attB3 Fwd	GGGGACAAGTTTGTATAATAAAGTTGTAATGGAGTCTACTGCTAACGCAC	Making donor clone, 1 PCRs

Table 1 Continued

NBR1 attB4 No Stop Rev	GGGGACAACTTTGTATAGAAAAGTTGGG TGAGCCTCCTTCTCCCCTGTG	Making donor clone, 1 PCRs
NBR1 attB4 Stop Rev	GGGGACAACTTTGTATAGAAAAGTTGGG TGCTATTAAGCCTCCTTCTCCCCTGTG	Making donor clone, 1 PCRs
NBR1 No Stop attbB2 Rev	GGGGACAACTTTGTACAAGAAAGCTGGG TTAGCCTCCTTCTCCCCTGTG	Making donor clone, 1 PCRs
NBR1 No Stop B4 Rev	GGGGACAACTTTGTATAGAAAAGTTGGG TGAGCCTCCTTCTCCCCTGTG	Making donor clone, 1 PCRs
NBR1 Stop attB2 Rev	GGGGACAACTTTGTACAAGAAAGCTGGG TTCTATTAAGCCTCCTTCTCCCCTGTG	Making donor clone, 1 PCRs
NBR1 Stop attB4 Rev	GGGGACAACTTTGTATAGAAAAGTTGGG TGCTATTAAGCCTCCTTCTCCCCTGTG	Making donor clone, 1 PCRs
NbRgsCaM attB1 Fwd	GGGGACAAGTTTGTACAAAAAAGCAGGC TTAATGGAATCGGTTTCTGTACCTAG	Making donor clone, 1 PCRs
NbRgsCaM attB2 No Stop Rev	GGGGACAACTTTGTACAAGAAAGCTGGG TTACTTGTCATCATAACTTTGAACTCATC	Making donor clone, 1 PCRs
RgsCaM No Stop attB4 Rev Full-length	GGGGACAACTTTGTATAGAAAAGTTGGG TGACTTGTCATCATAGCTTTGAACTC	Making donor clone, 1 PCRs
RgsCaM ΔN attB1 Fwd	GGGGACAAGTTTGTACAAAAAAGCAGGC TTAATGAGTAGTAGTAGCAAAAGTAATAA TAG	Making donor clone, 1 PCRs
ATG8e attB1 Fwd	CAAAAAAGCAGGCTTAATGAATAAAGGAA GCATCTTTAAGATG	Making donor clone, 2 PCRs
ATG8e attB2 Stop Rev	CAAGAAAGCTGGGTTCTATTAGATTGAAG AAGCACCGAATG	Making donor clone, 2 PCRs
ATG8e attB3 Fwd	TTTGTATAATAAAGTTGTAATGAATAAAGG AAGCATCTTTAAGATG	Making donor clone, 2 PCRs
ATG8e attB4 Stop Rev	CAACTTTGTATAGAAAAGTTGGGTGCTAT TAGATTGAAGAAGCACCGAATG	Making donor clone, 2 PCRs
CaM2 attB1 Fwd	CAAAAAAGCAGGCTTAATGGCGGATCAG CTCA	Making donor clone, 2 PCRs
CaM2 No Stop attB4 Rev	CAACTTTGTATAGAAAAGTTGGGTGCTTA GCCATCATAACCTTCACAAAC	Making donor clone, 2 PCRs
CaM2 Stop attB4 Rev	CAACTTTGTATAGAAAAGTTGGGTGCTAT TACTTAGCCATCATAACCTTCACAAAC	Making donor clone, 2 PCRs
CML38 attB1 Fwd	CAAAAAAGCAGGCTTAATGAAGAATAATA CTCAACCTCAATC	Making donor clone, 2 PCRs
CML38 attB2 No Stop Rev	CAAGAAAGCTGGGTTGCGCATCATAAGA GCAAAC	Making donor clone, 2 PCRs
CML38 attB2 Stop Rev	CAAGAAAGCTGGGTTCTATTAGCGCATCA TAAGAGCAAAC	Making donor clone, 2 PCRs
CML38 attB3 Fwd	TAATAAAGTTGTAATGAAGAATAATACTCA ACCTCAATC	Making donor clone, 2 PCRs

Table 1 Continued

CML38 attB4 No Stop Rev	GTATAGAAAAGTTGGGTGGCGCATCATAAGAGCAAAC	Making donor clone, 2 PCRs
CML38 attB4 Stop Rev	GTATAGAAAAGTTGGGTGCTATTAGCGCATCATAAGAGCAAAC	Making donor clone, 2 PCRs
DCP1 attB1 Fwd	AAAAAAGCAGGCTTCATGTCTCAAAACGGGAAGA	Making donor clone, 2 PCRs
DCP1 No Stop attB2 Rev	CAAGAAAGCTGGGTTTTGTTGAAGTGCATTTTG	Making donor clone, 2 PCRs
DCP1 STOP attB2 Rev	CAAGAAAGCTGGGTCTATCATTGTTGAAGTGCATTTTG	Making donor clone, 2 PCRs
HC-Pro attB1 Fwd	CAAAAAAGCAGGCTTAATGAGTGCAGCAGGAG	Making donor clone, 2 PCRs
HC-Pro attB2 No Stop Rev	CAAGAAAGCTGGGTTTGCAGCTCCGACGC	Making donor clone, 2 PCRs
HC-Pro attB2 Stop Rev	CAAGAAAGCTGGGTTCTATTATGCAGCTCCGACGC	Making donor clone, 2 PCRs
HC-Pro attB3 Fwd	TAATAAAGTTGTAATGAGTGCAGCAGGAGC	Making donor clone, 2 PCRs
HC-Pro attB4 No Stop Rev	GTATAGAAAAGTTGGGTGTGCAGCTCCGACGC	Making donor clone, 2 PCRs
HC-Pro attB4 Stop Rev	GTATAGAAAAGTTGGGTGCTATTATGCAGCTCCGACGC	Making donor clone, 2 PCRs
RBP47 attB1 Fwd	CAAAAAAGCAGGCTTAATGCAGACAACCAACG	Making donor clone, 2 PCRs
RBP47 attB2 No Stop Rev	CAAGAAAGCTGGGTTGCTAGCATTCTCCCCATG	Making donor clone, 2 PCRs
RgsCaM attB1 Fwd	CAAAAAAGCAGGCTTAATGGAATCAGTTTCTGTACCTAGTG	Making donor clone, 2 PCRs
RgsCaM attB3 Fwd	TAATAAAGTTGTAATGGAATCAGTTTCTGTACCTAGTG	Making donor clone, 2 PCRs
RgsCaM No Stop attB2 Rev	CAAGAAAGCTGGGTTACTTGTCATCATAGCTTTGAACTC	Making donor clone, 2 PCRs
RgsCaM No Stop attB4 Rev	GTATAGAAAAGTTGGGTGACTTGTCATCATAGCTTTGAACTC	Making donor clone, 2 PCRs
RgsCaM Stop attB2 Rev	CAAGAAAGCTGGGTTCTATTAACTTGTCATCATAGCTTTGAACTC	Making donor clone, 2 PCRs
RgsCaM Stop attB4 Rev	GTATAGAAAAGTTGGGTGCTATTAACTTGTCATCATAGCTTTGAACTC	Making donor clone, 2 PCRs
SGS3 attB1 Fwd	CAAAAAAGCAGGCTTAATGAGTTCTAGGGCTGGTCC	Making donor clone, 2 PCRs
SGS3 attB3 Fwd	TTTGTATAATAAAGTTGTAATGAGTTCTAGGGCTGGTCC	Making donor clone, 2 PCRs

Table 1 Continued

SGS3 No Stop attB2 Rev	CAAGAAAGCTGGGTTATCATCTTCATTGTGAAGGCC	Making donor clone, 2 PCRs
SGS3 No Stop attB4	CAACTTTGTATAGAAAAGTTGGGTGATCATCTTCATTGTGAAGGCC	Making donor clone, 2 PCRs
SGS3 Stop attB2 Rev	CAAGAAAGCTGGGTTCTATTAATCATCTTCATTGTGAAGGCC	Making donor clone, 2 PCRs
SGS3 Stop attB4 Rev	CAACTTTGTATAGAAAAGTTGGGTGCTATTAATCATCTTCATTGTGAAGGCC	Making donor clone, 2 PCRs
RgsCaM Fwd XbaI	GACTCTAGAATGGAATCAGTTTCTGTACCTAGTG	Making pBin19 35S::rgsCaM-mScarlet
RgsCaM Rev XmaI	GACCCCGGGACTTGTCATCATAGCTTTGAACTC	Making pBin19 35S::rgsCaM-mScarlet
ATG8e L52A Fwd	GCTGTGCCATCAGACCTAACAGTTG	Mutagenesis
ATG8e L52A rev	CAACTGTTAGGTCTGATGGCACAAGGTACTTCTTCTTGTCTATATTTGGGACTTC	Mutagenesis
RgsCaM F15A Rev	GAGGCATAAGATTTGTTTTCAACACTAGGTACAG	Mutagenesis
RgsCaM S16A Rev	GCGAAATAAGATTTGTTTTCAACACTAGGTACAG	Mutagenesis
ATG8e G118A B2 Rev	CAAGAAAGCTGGGTTCTATTAGATTGAAGAAGCAGCGAATGTGTTCTC	Mutagenesis, Making donor clone, 2 PCRs
ATG8e G118A B4 Rev	CAACTTTGTATAGAAAAGTTGGGTGCTATTAGATTGAAGAAGCAGCGAATGTGTTCTC	Mutagenesis, Making donor clone, 2 PCRs
pBiFC cYFP Fwd	GGCATGGACGAGCTGTACAAG	Sequencing pBiFC 2-in-1 constructs
pBiFC cYFP Rev	GATGCCGTTCTTCTGCTTGTC	Sequencing pBiFC 2-in-1 constructs
pBiFC nYFP Fwd	CAGCCACAACGTCTATATCATGGC	Sequencing pBiFC 2-in-1 constructs
pBiFC nYFP Rev	CTCGCCCTTGCTCACCATTC	Sequencing pBiFC 2-in-1 constructs
pEG101/102 seq Fwd	TCGCAAGACCCTTCCTCTAT	Sequencing pEarleyGate 101 and 102
pEG101/102 seq Rev	TACGTCGCCGTCCAGCTCGA	Sequencing pEarleyGate 101 and 102

Figure 3 Representative donor plasmid, pDONR 207, and donor construct, pDONR 207 CML38. pDONR 207 (left) contains a Gateway cassette with a chloramphenicol resistance gene (Cm(R)) and the *ccdB* suicide gene flanked by *attP1* and *attP2* recombination sites. The plasmid also has a bacterial gentamycin resistance gene (Gm(R)). Recombination of pDONR 207 with PCR-amplified *CML38* with a 5' attB1 and 3' attB2 recombination sites produces pDONR207 CML38 (right). The recombination converts the P1 and P2 sites to the L1 and L2 recombination sites needed for recombination into destination plasmids. "*CML38 no stop*" indicates that the stop codon was excluded by the reverse primer. All donor constructs for use in pEarleyGate 101 or 102, with C-terminally fused fluorescent tags contained no stop codons.

Gateway-compatible expression constructs with translational fluorescent protein fusions driven by the Cauliflower Mosaic Virus (CaMV) *35S* promoter were generated in pEarleyGate vectors (Earley et al. 2006) or pK7RWG2 (Karimi et al. 2005). These include: pEG101 (C-terminal YFP), pEG102 (C-terminal CFP), pEG104 (N-terminal YFP), and pK7RWG2 (C-terminal RFP). These localization constructs were generated by Gateway LR Clonase II reactions with pDONR207 constructs containing the gene-of-interest, per manufacturer's protocol (Invitrogen). pEarleyGate constructs were selected on LB plates with 50 µg/ml kanamycin. The pK7RWG2 construct was selected with 100 µg/ml spectinomycin.

The following Gateway-compatible clones were generated and used in this study: pEG 101 *rgsCaM-YFP*, pEG 102 *rgsCaM-CFP*, pEG 102 *DCP1-CFP*, pEG 101 *SGS3-YFP*, pEG 102 *SGS3-CFP*, pEG 104 *YFP-ATG8e*, and pK7RWG2 *RBP47B-RFP*. pEG 102 *RBP47B*-CFP was generated as previously described in (Lokdarshi et al. 2016). All generated plasmids confirmed by DNA sequencing.

A translational fusion construct of *rgsCaM* with the *mScarlet* fluorescent reporter protein (Bindels et al. 2017) was prepared in pBin19 (Frisch et al. 1995). *Xba*I and *Xma*I sites were introduced into the *Nt-rgsCaM* open reading frame at the 5' and 3' ends respectively by PCR using gene specific primers with these sites (Table 1). *Nt-rgsCaM* was then subcloned into these sites within pAN990 (a gift from Andreas Nebenführ, University of Tennessee – Knoxville) to generate the *mScarlet* translational fusion under the control of the *35SCaMV* promoter. A fragment containing *35S::rgsCaM-mScarlet* was excised by digestion with SacI and HindIII, and subcloned into pBin19.

2.1.2 Generation of ratiometric BiFC constructs

pBiFCt-2in1 plasmids (Grefen et al. 2012) were used for ratiometric BiFC. Donor clones were generated in pDONR 221 plasmids containing either *attP1* and *attP4* sites, or *attP3* and *attP2* sites using the PCR strategies described in section 2.1.1, and primers in Table 1. BiFC pairs were generated in a Multisite LR clonase II *plus* (Invitrogen) reaction with each reaction containing the two desired pDONR221 constructs for the interaction assay and one pBiFC 2-in1 plasmid. The multisite LR II *plus* reactions were modified from the Invitrogen protocols. Each reaction contained 10 fmols of the pBiFC plasmid and 30 fmols of each of the two pDONR 221 constructs (one with an insert flanked with attL1 and attL4 sites, and the other flanked with attL3 and attL2 sites). In addition to the plasmids, 0.5 µl of LR clonase II *plus* enzyme mix (which includes the buffer) was added, and the volume was raised to a total of 3 µl with TE buffer (10 mM Tris pH 8 with HCL, 1 mM EDTA). The reactions were incubated at room temperature overnight. Following incubation, 0.25 µl of the Proteinase K solution (provided with enzyme) was added and the reactions were incubated at 37ºC for 10 min. The entire reaction mixture was added to 100 µl of chemically competed Top 10 *E. coli* cells (ThermoFisher) for transformation. For selection, LB agar plates supplemented with 100 µg/mL spectinomycin were prepared, and when solidified, isopropyl-β-D-1-thiogalactoside (IPTG; 40 µl of 100 mM IPTG in H_2O) and 5-bromo-4-chloro-3-indolyl-β-D-galactopyranoside (X-Gal; 120 µl of 20 mg/ml X-Gal in dimethylformamide (DMF)) were spread on the surface for blue-white screening. White colonies were screened by colony PCR and grown for plasmid purification and DNA sequencing.

Site-directed mutagenesis was conducted on pDONR 221 plasmids containing Arabidopsis *ATG8e* or *rgsCaM* for use in ratiometric bimolecular fluorescence complementation (rBiFC). Mutagenesis was performed according to the "'round the horn" protocol (OpenWetWare). Briefly, a mutagenic forward primer and a non-mutagenic reverse primer were designed such that they would amplify the entire plasmid into a linear molecule (with no overlapping sequence at the ends). The mutagenic primer contained the base substitutions at its 5' end. The primers were designed such that the annealing portions have a T_m between 60ºC to 63ºC. Before PCR, the primers were phosphorylated in a reaction containing polynucleotide kinase (PNK) and ATP (OpenWetWare). Following PCR, a *DpnI* reaction was performed to degrade methylated template DNA (OpenWetWare). The PCR product was then gel-purified, and an overnight T4 DNA ligase reaction was performed at room temperature. Mutagenesis primers for ATG8e L52A and G118A mutations are listed in Table 1.

An N-terminal truncation of rgsCaM (ΔN-rgsCaM) that removes amino acids 1-42 was also generated for BiFC. The coding region of *Nt-rgsCaM* corresponding to amino acids 43-190 was amplified from pDONR207 *Nt-rgsCaM* using an rgsCaM ΔN attB1 forward primer and the rgsCaM attB4 reverse primer (Table 1), and was recombined into pDONR 221 to generate a donor plasmid containing *ΔN-rgsCaM*.

Turnip mosaic virus helper component proteinase (HC-Pro) was amplified from pENTR TuMV *HC-Pro* (a gift from Dr. Vickie Vance, University of South Caroline, USA) using primers which incorporated attB recombination sites. *HC-Pro* was cloned into

pDONR 221 plasmids for use in BiFC (pBiFC plasmids) (Grefen et al. 2012) and FRET (pFRET plasmids) (Hecker et al. 2015).

BiFC clones generated and used in this study include: pBiFC NN *ATG8e*, *rgsCaM*; pBiFC NC ATG8e, *rgsCaM*; pBiFC NN *ATG8e*, CaM2; pBiFC NC *ATG8e*, CaM2; pBiFC NC *ATG8e-L52A*, rgsCaM; pBiFC NC *ATG8e-G118A*, *rgsCaM* and pBiFC NC *ATG8e*, *ΔN-rgsCaM*; pBiFC NC *ATG8e*, *rgsCaM-F15A;* pBiFC NC *ATG8e*, *rgsCaM-S16A* and pBiFC NC HC-Pro, rgsCaM. The two-letter code "NN" or "NC" indicates whether the split-YFP is positioned at the N- or C-terminus of each coding sequence. For instance, pBiFC NC ATG8e, rgsCaM expresses nYFP-ATG8e and rgsCaM-cYFP.

2.1.3 Construction of the hypoxia sensor

A 408bp synthesized DNA fragment (Invitrogen gene synthesis) was ordered which contained the nucleotide sequence for the first 28 amino acids of *A. thaliana* RAP2.12, followed by an *EcoRI* site. Additional nucleotides were included at the 5' end corresponding to the sequence of the pDONR/Zeo NLS-3xVenus plasmid (a kind gift from Dr. Robertas Urasche, University of Lausanne, Switzerland) to facilitate cloning back into this plasmid, spanning to the *AclI* site (major vector maps for hypoxia sensor construction are shown in results section 3.12). The synthetic fragment was cloned into pDONR/Zeo NLS-3xVenus at the *AclI* and *EcoRI* sites. The resulting plasmid, pDONR/Zeo HypoxSens-NLS-3xVenus (Figure 4) was recombined in a Gateway (Invitrogen) LR Clonase II reaction with the *35S* promoter-containing pEarlyGate100 (Earley et al. 2006), according to manufacturer's protocol. The modified regions of these

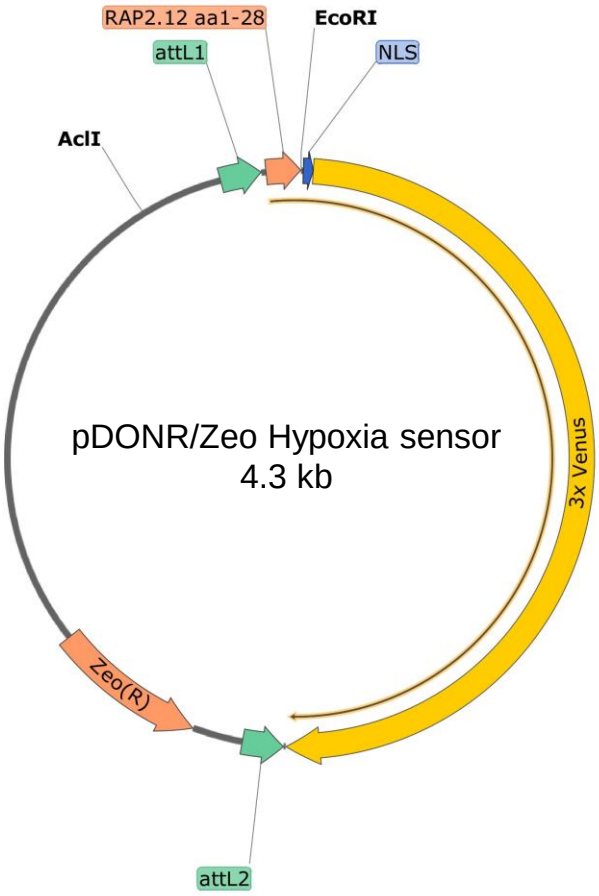

Figure 4 Vector map of pDONR/Zeo with assembled hypoxia sensor coding sequence. The ligation product after the fragment from *AclI* to *EcoRI* was replaced with the sequence from the synthetic gene construct containing the first 28 amino acids from RAP2.12. The RAP2.12 fragment in in frame with the SV40 nuclear localization signal and three tandem venus fluorescent proteins. *Zeo(R*) is a bacterial zeocine resistance gene. The Gateway recombination sites in this Gateway-compatible donor vector are indicated with *attL1* and *attL2*. The sequence spanning the hypoxia sensor translational fusion are indicated with the yellow-outlined black arrow.

plasmids were verified by Sanger sequencing. The constructed plasmid (pEarleyGate 100 *35S::RAP2.12 aa1-28-NLS-3xVenus*) was named pHypox 1.

Generation of the pHypox 2 plasmid for ratiometric imaging added the additional coding sequence: *35S::NLS-mScarlet* to the previously constructed pHypox 1. mScarlet was PCR-amplified from pAN990 (from Andreas Nebenführ, University of Tennessee, USA) using primers which incorporated the SV40 nulcear localization signal at the 5' end as well as the attB1 recombination site (Table 1). The attB2 recombination site was incorporated at the 3' end. A Gateway BP reaction introduced the insert into pDONR 207. The resulting donor construct was then recombined in a Gateway LR reaction with pEarleyGate 100 to produce pEarleyGate 100 NLS-mScarlet. pEarleyGate 100 contributes the *35S* promoter and the transcriptional terminator which flank the NLS-mScarlet insert. The sequence from the *35S* promoter through the terminator was PCR-amplified with PCR primers which added a 5' *HindIII* site and a 3' *PmeI* site. Restriction digestion and ligation were used to introduce this sequence into the *HindIII* and *PmeI* sites of pHypox 1, producing pHypox 2 (see section 3.12 for vector map).

Sanger DNA sequence analysis of all plasmid constructs generated in this thesis and was performed on all an Applied Biosystems 3730 Genetic Analyzer at the University of Tennessee Genomics Core Facility.

2.2 Plant growth and transfection

Nicotiana benthamiana seeds were sown in Lambert LM-GPS soil for germination and were grown in an environmental growth chamber with long day conditions (16h light at 25°C/8h dark at 23°C) and 50% humidity under a light intensity of

100 µmol m^{-2} s^{-1}. Four to five-week-old plants (prior to flowering) were used for transfections. Binary vectors were introduced into *Agrobacterium tumefaciens* strain GV3101 (Koncz et al. 1986) by electroporation (Jones 1995) or heat shock (Hofgen et al. 1988), and selected on LB agar plates supplemented with 50 µg/mL rifampicin, 50 µg/mL gentamycin and either 50 µg/mL kanamycin (for pEarleyGate plasmids) or 100 µg/mL spectinomycin (for pBiFCt-2in1 plasmids). Selected colonies were grown in LB broth with the same antibiotics at 28°C for 24-48 hr. Infiltration of *N. benthamiana* was performed as previously described (Brunkard et al. 2015). Cells were collected by centrifugation at 3,000 x *g* for 10 min and pellets were resuspended in 10 mM $MgCl_2$, 10 mM MES-NaOH, pH 5.7, 200 µM acetosyringone. The inoculum was incubated with slow rotation at 20°C for 2-4 hr to allow acetosyringone-induction of virulence gene expression. For co-infiltrations, cultures containing each plasmid were combined prior to infiltration so that each was equivalent to OD_{600} of 0.4. Combined *A. tumefaciens* cultures were infiltrated into the abaxial side of leaves using a needless syringe and the infiltrated region was marked. Plants were kept at 20°C overnight on a lab bench, and then transferred to growth light racks (16 h light at 22-25ºC, 8 h dark at 20-22ºC). Imaging experiments were performed two days after infiltration.

Arabidopsis thaliana Col. 0 transformed with pEarleyGate *35S:CML38-YFP* were grown according to Choi et al. (2007). Briefly, seeds were surface sterilizing, stratified in water at 4ºC for two days, and allowed to germinate on ½-strength MS agar plates in an environmental chamber under long-day conditions (16 h light at 22ºC, 8 h dark at 20ºC). Light intensity was adjusted to 100 µmol m-2s-1. Seedlings grew on vertical plates for 14 days prior to conducting the cycloheximide treatment experiment.

2.3 Slide preparation and hypoxia treatment

Approximately one cm^3 leaf discs were cut from infiltrated regions adjacent to the site of injection. Tissues were placed in a 25 ml syringe in DI water and a brief manual vacuum infiltration was administered with a syringe to remove air pockets as described by (Brunkard et al. 2015). Hypoxia was administered by immersing leaf samples in DI water on a #1.5 coverslip, adaxial face down, with a slide covering the sample, essentially as described previously (Lokdarshi et al. 2016). The times of slide preparations were recorded and used to reference the onset of hypoxia treatment based on (Weber et al. 2008, Sorenson et al. 2014, Lokdarshi et al. 2016). Imaging was performed on adaxial epidermal cells, typically 1 to 2 hr after mounting samples on slides.

For assessing the hypoxia sensor pHypox 1, hypoxia was administered with the addition of the commercial reagent EC-Oxyrase (Oxyrase, Inc.) to the slide during preparation. 8 units mL^{-1} of EC-Oxyrase reagent (Oxyrase, Inc.) were added to the DI water to induce rapid hypoxia.

2.4 Cycloheximide treatment

Cycloheximide treatment of 14-day-old Arabidopsis seedlings was performed as previously described (Sorenson et al. 2014). Seedlings were submerged for 35 min at room temperature in 1x Murashige and Skoog (MS) medium supplemented with 200 ng μL^{-1} cycloheximide and a final (v/v) of DMSO of 0.4%. Mock treatment used DMSO without cycloheximide. Seedlings were kept in the dark throughout treatment until imaging. Slides were prepared in 1x MS medium with 8 units mL^{-1} EC-Oxyrase

(Oxyrase Inc.) for rapid induction of hypoxia. Images were captured within 10 min of slide preparation.

2.5 Microscopy and imaging techniques

Colocalization imaging

A Leica SP8 laser scanning confocal microscope (Wetzlar, Germany) was used for all microscopy performed in this study. For co-localization experiments, each fluorescence channel was captured sequentially to prevent signal cross-talk. Sequential imaging was performed between scan lines to limit discrepancies between channels due to granule movement. Scan line averaging of four was used. Excitation/emission bandwidth settings for imaging were: 405 nm/425-500nm (DAPI), 470 nm/480-530 nm (CFP), 514 nm/540-575 nm (YFP), 575 nm/600-660 nm (RFP), and 590 nm/600-660 (mScarlet). Chloroplast autofluorescence was also captured over 680-740 nm, usually during YFP imaging, to ensure chloroplast fluorescence was not visible in other channels. To further reduce the likelihood of chloroplast autofluorescence when imaging CFP, YFP or RFP, time gating was used on the HyD hybrid detectors to exclude emission coming from the first 0.3 ns following pulsed excitation from the white light laser (Kodama 2016). Laser strength and gain were adjusted for each image as needed to produce signal just below saturation. For DAPI staining (4′,6-diamidino-2-phenylindole; Sigma, St. Louis, MO), transfected leaf discs were cut and placed in DI water with 5 µg/ml DAPI for 30 min prior to mounting for imaging. Co-localization imaging was performed over a Z-series to include the entire proximal surface of the cell, but to exclude the distal surface where signal from lower cell layers can be seen. The

step-size between optical sections was typically between 1-2 µm. The specific step sizes and the number of sections included in 2D projection images are described in each figure legend. The pinhole size was 0.8-1 AU.

Ratiometric bimolecular fluorescence complementation imaging

For BIFC analysis, pBiFC 2-in-1 plasmids (Grefen et al. 2012) expressing the two proteins of interest as nYFP or cYFP fusions were transfected into *N. benthamiana* as described in 2.2. The BiFC plasmid also expresses a constitutive mRFP1 which serves as a reference for ratiometric comparison to the YFP BiFC signal. This ratiometric approach allows for quantification of BiFC signals and controls for differences in plasmid copy number among transfected cells. mRFP1 was imaged with excitation/emission bandwidth of 543 nm/560-615 nm, while the eYFP BiFC signal used 514 nm/520-550 nm. Imaging experiments with both channels used time gating to exclude the first 0.3 ns to reduce chloroplast autofluorescence (Kodama 2016). Sequential imaging was performed between scan lines, with a line averaging of four used for each image of a single optical section. For each experimental replicate, leaf sections were screened to find standard excitation and gain settings that would produce images without oversaturation across all samples. Transfected cells were located by scanning for mRFP1 fluorescence. Four biological replicates were used, with at least five cells analyzed from each. Identical BiFC results were obtained for both N and C terminal fusions of rgsCaM, and only the results with C-terminal fusions of rgsCaM and rgsCaM mutants were analyzed further. A negative control construct (pBiFC NC *ATG8e*, *CaM2*) was generated in which Arabidopsis *calmodulin 2* (*CaM2*) was used in place of *rgsCaM*.

Acceptor photobleaching Förster resonance energy transfer assay

AB FRET was performed using the Leica LAS X AB FRET software module. Photobleaching of venus was performed with a 514 nm argon laser at full strength for 10 seconds. Imaging of mTurquoise2 (mTRQ2) used 405 nm excitation and emission bandwidth of 460-520 nm. Imaging of venus used 514 nm excitation and emission bandwidth of 525-590 nm. Calculation of the range of observed fluorophore distances based on FRET intensities used the equation, $E = R_0^6/(R_0^6 + r^6)$ (Gilmore 2013), where E = FRET efficiency, R_0 = Förster radius, 5.8 nm was used for the mTRQ2 and Venus pair (Bajar et al. 2016), and r = the radius, or distance between fluorophores (Gilmore 2013).

2.6 Image analysis and processing

Routine image processing

Confocal micrographs were captured with Leica LASX software and uncompressed images were exported and analyzed in ImageJ (Schneider et al. 2012). Brightness was increased to just below saturation, the built-in smoothing filter was applied to reduce noise. Scale bars added and false colorations and channel mergers were applied. Maximum intensity 2D projections were also performed in ImageJ. When sample drift was apparent during a Z-series image capture, stacked images were aligned using the ImageJ StackReg plugin with the rigid body method (Thevenaz et al. 1998).

Colocalization analysis

Colocalization analysis was performed in ImageJ using the Just Another Colocalization Plugin (JACoP) (Bolte et al. 2006). Images corresponding to the two channels were imported and a region of interest (ROI) was selected to correspond to the cytosol of an individual cell. The threshold was adjusted to minimize background. JACoP was used to compute the Pearson correlation coefficient (PC) along with a Van Steensel's cross-correlation analysis (van Steensel et al. 1996), and Manders' coefficients (Manders et al. 1992).

For determining Pearson's coefficients, analysis software generates a scatter plot in which each pixel in the image is potted with coordinates based on its intensity in the two channels (Bolte et al. 2006). For instance, the position along the X-axis could be the intensity in a CFP channel, while the position along the Y-axis could represent a YFP channel. Perfect colocalization would result in points which fall along a straight line (Bolte et al. 2006). The strength of the colocalization can be described by quantifying the distribution of points around this line. If points are tightly clustered around the trendline, colocalization is strong, whereas lower colocalization will have more distributed data points (Bolte et al. 2006). Pearson's coefficients range from 1, for complete colocalization, to -1, for negative correlation, meaning the signals are mutually exclusive. A PC of 0 indicates no correlation (Bolte et al. 2006). A Van Steensel's cross-correlation analysis (van Steensel et al. 1996) plots the PCs obtained as one channel is shifted in the X-axis relative to the other, over a set range of pixels (-20 to +20 used here). The objects in the image must be small enough for a 20 pixel shift to cause a significant loss of colocalization, which is the case for the cytosolic granules in this

study. Real colocalization should produce a gaussian distribution centered at 0 (van Steensel et al. 1996, Bolte et al. 2006).

Pearson's coefficients are very sensitive to background noise, which contributes to poorly correlated pixels that are generally of lower brightness than true signal. Corrections are performed by setting a threshold to exclude signal falling below a selected brightness value. Conventionally, conclusions regarding colocalization or exclusion are not drawn from PCs falling between -0.5 and 0.5 (Bolte et al. 2006). PCs are a commonly used first-line assessment of colocalization, but they do not rigorously evaluate colocalization (Bolte et al. 2006, Dunn et al. 2011).

Manders' overlap coefficients (MC) were also computed as they better describe situations of unequal colocalization for fluorophores A and B (e.g.: A always overlaps with B, but B is also often independent of A) (Bolte et al. 2006). MCs range from 0 to 1, representing non-overlapping and completely overlapping signals, respectively. Two Manders' coefficients are generated. One will quantify the fraction of A overlapping with B, while the other quantifies the fraction of B overlapping with A. Mander's coefficients are also very sensitive to noise and background, and require a threshold to be set (Bolte et al. 2006).

Line plot profiles

Data for line plots were obtained by drawing a line through the indicated region in ImageJ and using the built-in plot profile function within ImageJ. The output of brightness values by distance (µm) for each pixel was imported into Excel, converted

into percentages based on the highest obtained value by channel, and imported into Prism 8.1.1 (GraphPad) for figure generation.

Image deconvolution

Two approaches for Image deconvolution were used. Figure legends referring to "standard deconvolution" had images subjected to deconvolution in Huygens Essentials (Scientific Volume Imaging, Hilversum, The Netherlands), using the standard profile for automatic deconvolution. "Lightning deconvolution" used the Leica Lightning deconvolution system. The Lightning system optimizes image capture settings for Z-axis step size, resolution and scan speed based. A slider is used to choose settings favoring capture speed or resolution. Our imaging maximized resolution. The adaptive deconvolution profile setting in the Leica Lightning Deconvolution package was used.

3D modelling of confocal micrographs

Imaris (Oxford Instruments, Zurich, Switzerland) was used to generate 3D models from deconvolved Z-series signal volumes in selected co-localization experiments. Thresholds were defined for CFP and YFP signals to produce models corresponding to their respective signal volume data. To correct for signal bleed in the Z-axis, the setting for the Z-axis step size in Imaris was adjusted to produce a spherical shape of the imaged rgsCaM granules (Figure 15) or DCP1 granules (Figure 17).

Ratiometric BiFC analysis

Ratiometric BiFC analysis was similar to previously described methods (Grefen et al. 2012). In ImageJ, a region of interest (ROI) was traced to select individual cells.

Nuclei were not visible in all images and they were excluded from the ROI when present in case the BiFC complex had different nuclear preference than the mRFP1. ImageJ was used to compute the average brightness of the ROI for YFP and RFP channels. Data were exported to Excel and the eYFP: mRFP1 ratios were calculated for each cell. The values were normalized to the highest signal, which in all experiments was ATG8e and rgsCaM. Statistical analysis was performed in GraphPad Prism version 8.1.1 (Graph Pad).

2.7 Infection of Arabidopsis with turnip mosaic virus

The GFP-expressing TuMV infection clone, pCB-TuMV-GFP, based on the UK1 strain (Lellis et al. 2002), was used to infect Arabidopsis lines by agroinfiltration. Three lines were used: *35S::CML38-YFP* from (Lokdarshi et al. 2016) with constitutive CML38-YFP expression, a cml38ko T-DNA insertion line (Salk_066538C), and wt plants. pCB-TuMV-GFP was introduced into *Agrobacterium* GV3101 and infiltrated into two rosette leaves of four-week old plants. The clone has the GFP coding sequence inserted into the viral genome with flanking viral protease cleavage sites such that free GFP is produced where the virus has spread (Lellis et al. 2002). Infection progress was monitored daily by illumination under 395 nm light. The first day at which each plant showed GFP in an uninoculated leaf was recorded as the time of systemic infection.

2.8 Generating multiple sequence alignments and phylogenetic trees

A multiple sequence alignment was performed on amino acid sequences for the seven Arabidopsis CaMs, 50 CMLs, and rgsCaM from *N. tabacum* and *N. benthamiana* with the MEGA 6.06 software package (Tamura et al. 2013), using the MUSCLE

algorithm (Edgar 2004). Iterations were performed until convergence was reached. The protein sequences for the Arabidopsis CaMs and CMLs used in the alignment corresponded to the accession numbers reported in McCormack *et. al* (2003) (McCormack et al. 2003). A phylogenetic tree was generated with MEGA 6.06 from the alignment using the maximum likelihood algorithm and the Jones-Taylor-Thornton model (Jones et al. 1992) with 200 bootstrap iterations. Figtree 1.4.2 (http://tree.bio.ed.ac.uk/software/figtree) was used to generate the phylogenetic tree figure.

Methods for calculating sequence identities, similarities, applying color-coding based on amino acid chemical properties for alignments, and annotation of domains are described within figure legends.

2.9 GeneID and accession numbers

The GenBank accession numbers for coding sequences used in this study are: NM_106315.3 (*At-CML38*), NM_100710.4 (*At-DCP1*), NM_112800.4 (*At-RBP47B*), NM_001343817 (*At-SGS3*), NM_180100.7 (*At-ATG8e*), NM_180013.3 (*At-CaM2*), AF329729.1 (*Nt-rgsCaM*) and JX402081.1 (*Nb-rgsCaM*). *HC-Pro* comes from the UK1 strain of TuMV, and has an identical nucleotide sequence to the infectious clone pCB TuMV-GFP that is used in infection assays in this study (EF028235) (Lellis et al. 2002).

Chapter 3: Results

3.1 Arabidopsis CML38 localizes to hypoxia-induced mRNP stress granules and processing bodies

Elements of this work with respect to CML38 appeared in Lokdarshi, Conner et al., 2016 and are referenced here. Data figures shown in this results section were generated and prepared by the thesis author.

As summarized in the introduction, CML38 and rgsCaM, the two subjects of this work, are phylogenetically related calcium sensors in a clade that is referred to as the "regulator of gene silencing calmodulins" (**Figure 5**). For the sequence identities of these family members see (Figure 5B).

As an early step in investigating the function of CML38, the subcellular localization of CML38 was determined in *N. benthamiana* under normoxic and hypoxic conditions {Lokdarshi, 2016 #45}. The plant binary vector pEarleyGate 101 (Figure 6) (Earley et al. 2006) was used to generate a *CML38-YFP* localization clone. The coding sequence for *CML38* was introduced into pEarleyGate 101 using Gateway recombination (see Materials and Methods for details) to produce pEarleyGate 101 CML38 (Figure 7). pEarleyGate 101 contains a CaMV *35S* promoter, followed by a Gateway recombination cassette which is replaced with the gene-of-interest, the in-frame YFP coding sequence, and a transcriptional terminator (Earley et al. 2006). The CaMV *35S* promoter is constitutively active in nearly every plant tissue and in a wide range of plants (Bhullar et al. 2007). This allows for the investigation of the localization

Figure 5 Phylogeny of tobacco rgsCaMs and Arabidopsis CaMs and CMLs. (A) A phylogenetic tree for the seven Arabidopsis CaMs, 50 Arabidopsis CMLs and the rgsCaM proteins from *N. tabacum* and *N. benthamiana*. Names and sequences of the Arabidopsis CaMs and CMLs correspond to those previously described (McCormack et al. 2003). The CMLs clustering with rgsCaM are highlighted in blue correspond to the "regulator of gene silencing calmodulin-like proteins" (rgsCMLs). The scale bar indicates alignment and with similarity data from the Ident and Sim tool available at "http://www.bioinformatics.org/sms2/ident_sim.html." the branch length corresponding to 0.3% amino acid sequence divergence. **(B)** Percent protein sequence similarity matrix for the indicated proteins generated using a MUSCLE.

A

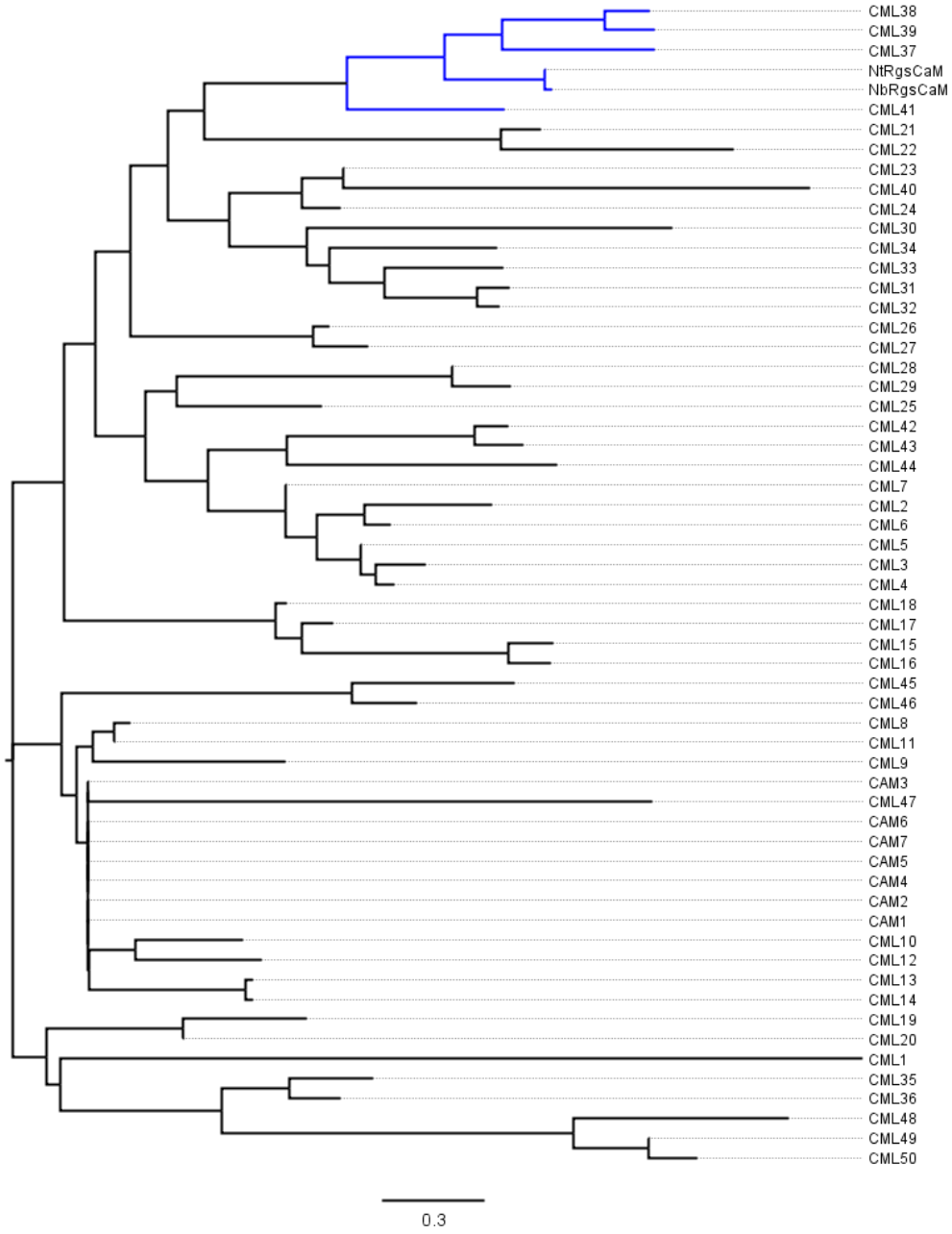

B

	CML37	CML38	CML39	CML40	CML41	NtRgsCaM
CML38	61.62	-	-	-	-	-
CML39	55.61	71.82	-	-	-	-
CML40	41.49	47.22	50	-	-	-
CML41	44.88	45.85	43.9	45.55	-	-
NtRgsCaM	59.16	57.89	51.56	53.17	52.2	-
NbRgsCaM	62.63	59.04	52.11	45.55	52.2	91.58

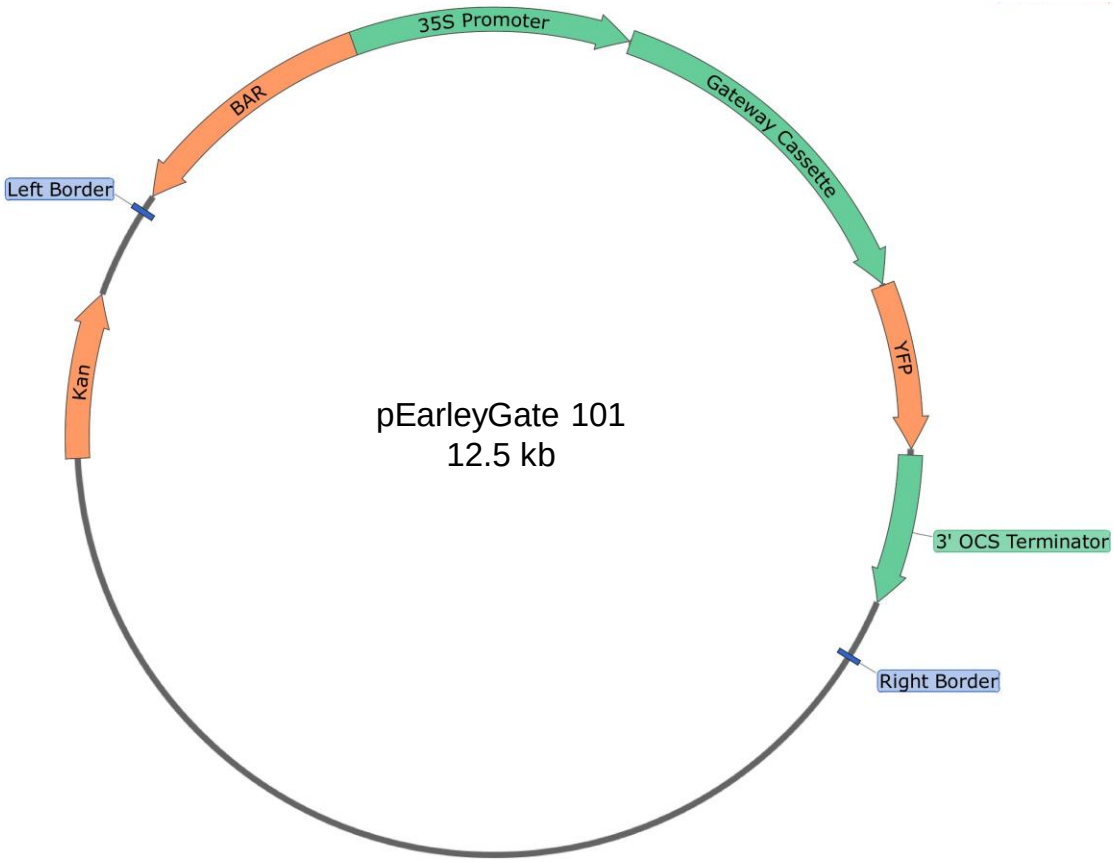

Figure 6 Representative pEarleyGate plasmid, pEarleyGate 101. This plasmid contains a Gateway-compatible cassette which includes a chloramphenicol resistance gene and the *ccdB* suicide gene flanked by *attP1* and *attP2* recombination sites. There is a CaMV 35S promoter upstream of the cassette and a YFP coding sequence to provide a C-terminal YFP fusion to an inserted coding sequence. The bacterial kanamycin resistance gene is shown (*Kan*), as well as the left and right T-DNA borders, enclosing the sequence which will transform plants. Following the YFP coding sequence, the 3' end of the octopine synthase (OCS) transcript is present as a transcriptional terminator.

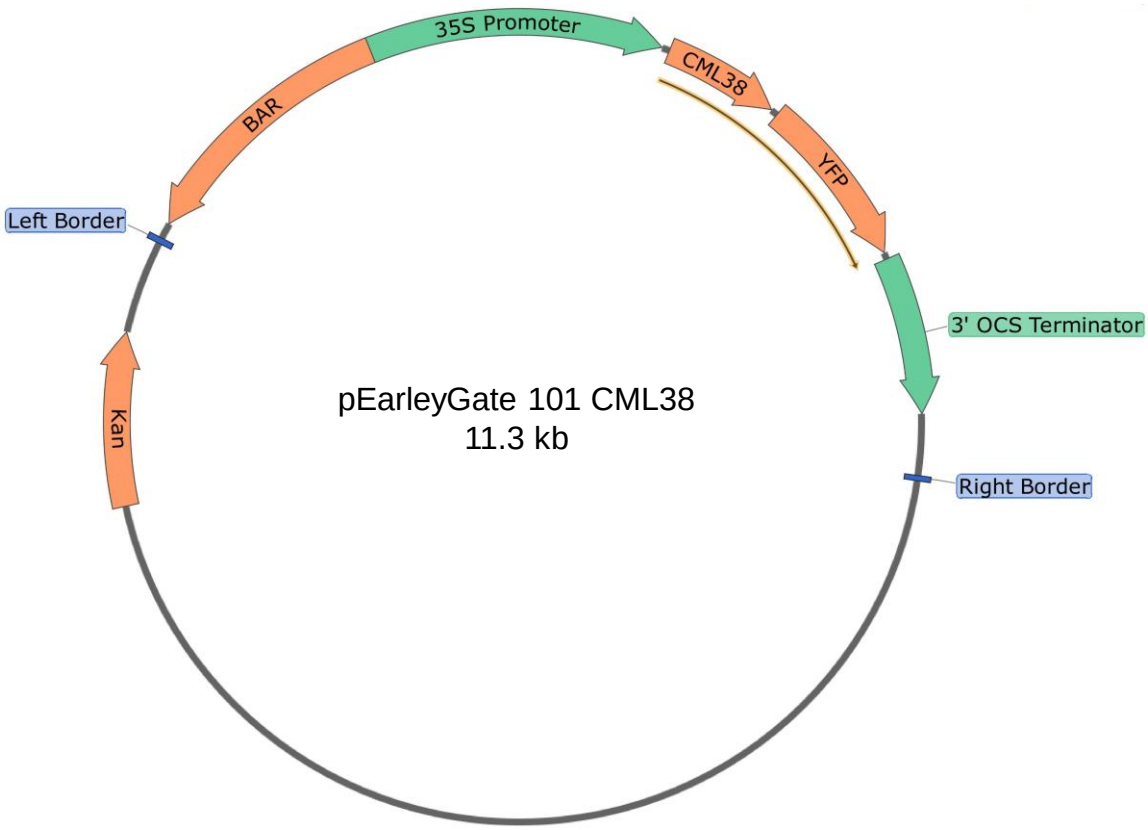

Figure 7 Representative pEarleyGate localization construct, pEarleyGate 101 *CML38*. This plasmid is the product of recombination of pEarleyGate 101 with pDONR 207 CML38. The Gateway cassette is replaced with the *CML38* coding sequence, and the sequence encoding the CML38-YFP fusion protein is indicated with a yellow-outlined black arrow.

behavior of this hypoxia-induced protein under both nonmoxic and hypoxic conditions, and in Arabidopsis as well as *N. benthamiana*. *N. benthamiana* was employed since it is a plant that is highly amenable to transient transfection by *Agrobacterium* infiltration of leaves (Brunkard et al. 2015), making it a useful and facile technique for protein localization studies. Using this system, transgenes can be introduced and examined within approximately 3 days, rather than the months needed for generating Arabidopsis transgenic lines.

To investigate the localization of CML38-YFP in *N. benthamiana* leaves, pEarleyGate 101 *CML38-YFP* was introduced into *Agrobacterium tumefaciens* strain GV3101 by electroporation (Fromm et al. 1985). A selected colony carrying the verified plasmid was then agroinfiltrated into *N benthamiana* leaves for transformation. After 2 days, leaf discs were dissected and imaged by confocal microscopy. Prior to submergence (normoxic conditions) leaves initially showed CML38-YFP in the nucleus and in the cytosol with a diffuse localization (Figure 8). As the leaf disc remains submerged in water between the coverslip and slide, the conditions naturally become hypoxic over time (Weber et al. 2008, Sorenson et al. 2014, Lokdarshi et al. 2016). In representative images, at 5 min after slide preparation CML38-YFP had diffuse cytosolic localization, while by 1 hr it had dramatically re-localized to foci (Figure 8.) This hypoxia-induced localization was confirmed in transgenic Arabidopsis lines using the native promoter (Lokdarshi 2015, Lokdarshi et al. 2016).

The CML38-YFP foci are similar in size to that of stress granules (0.1 to 2 µm) (Anderson et al. 2009, Sorenson et al. 2014, Lokdarshi et al. 2016) which also form

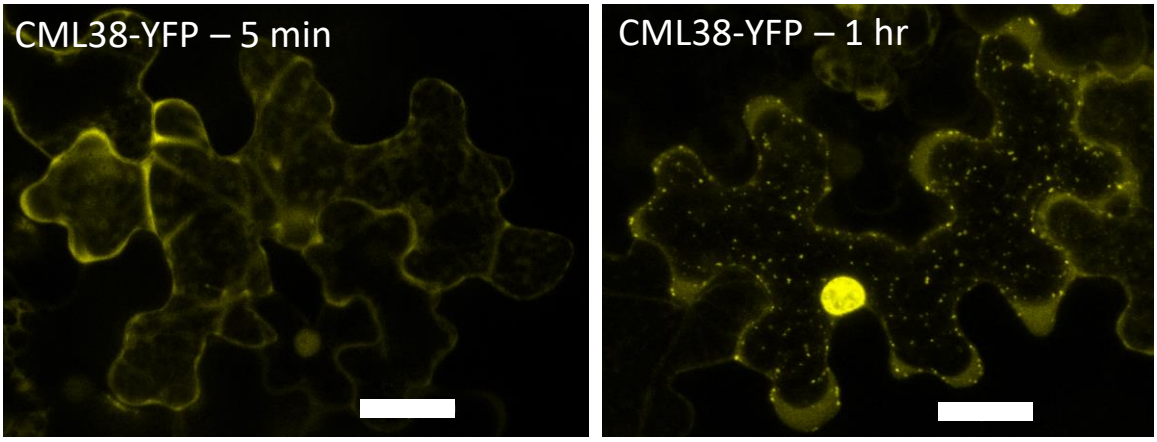

Figure 8 CML38 localizes to hypoxia-induced cytosolic foci. *N. benthamiana* leaves were transfected with pEarleyGate 101 CML38-YFP. Approximately 5 min after slide preparation CML38-YFP showed diffuse cytosolic signal, but at 1 hr of hypoxia pronounced cytosolic foci are visible. Images are 2D projections. The 5 min image is from 6 optical sections with a step size of 2 µm. The 1 hr image is from 9 optical sections with a step size of 3 µm. Scale bars are 30 µm.

under hypoxia (Weber et al. 2008). To determine whether the CML38 foci are SGs, a colocalization experiment with CML38 and the SG marker protein RBP47B was performed. *RBP47B* was cloned into pEarleyGate 102. This plasmid differs from pEarleyGate 101 (Figure 6) only in that CFP is substituted for YFP. *Agrobacterium* containing the CML38-YFP and the RBP47B-CFP constructs were combined and infiltrated into *N. benthamiana* leaves. Fluorescence confocal microscopy examination showed that CML38 does indeed strongly colocalize with hypoxia-induced RBP47B stress granules in *N. benthamiana* (Figure 9). This colocalization was quantified in Lokdarshi et al (2016) and showed a Pearson's correlation coefficient (PCC) (Bolte et al. 2006) of 0.63 (Lokdarshi et al. 2016), indicating partial colocalization (see Materials and Methods).

To determine whether this localization is specific to CML38 or is a common property of calcium sensors, the experiments were repeated using the *bona-fide* calmodulin *A. thaliana* calmodulin 2 (CaM2) as a control. After 2 hr of hypoxia, abundant RBP47B stress granules were present, while CaM2 showed only diffuse localization in the cytosol and the presumptive nucleus (Figure 10), which is a common feature of these ubiquitous, highly conserved proteins.

To provide additional evidence that CML38 localizes to stress granules, we conducted an experiment investigating whether granule accumulation is sensitive to the translational inhibitor cyclohexamide (Figure 11). Cycloheximide arrests translational elongation and prevents the ribosomal runoff which is needed before stress granules can form. As a result, cycloheximide treatment can be used to verify that granules

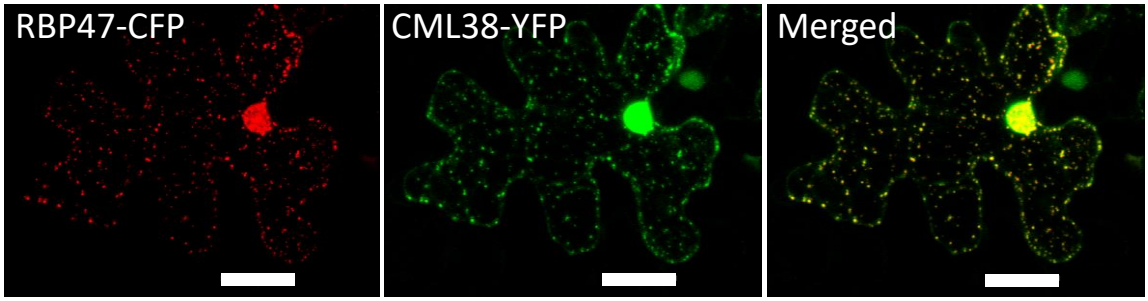

Figure 9 CML38 colocalizes with the stress granule marker RBP47B to hypoxia-induced cytosolic granules. Images are from a transfected *N. benthamiana* leaf after 1 hr of hypoxia and are 2D projections from 18 optical sections with a step size of 2 µm. Scale bars are 30 µm.

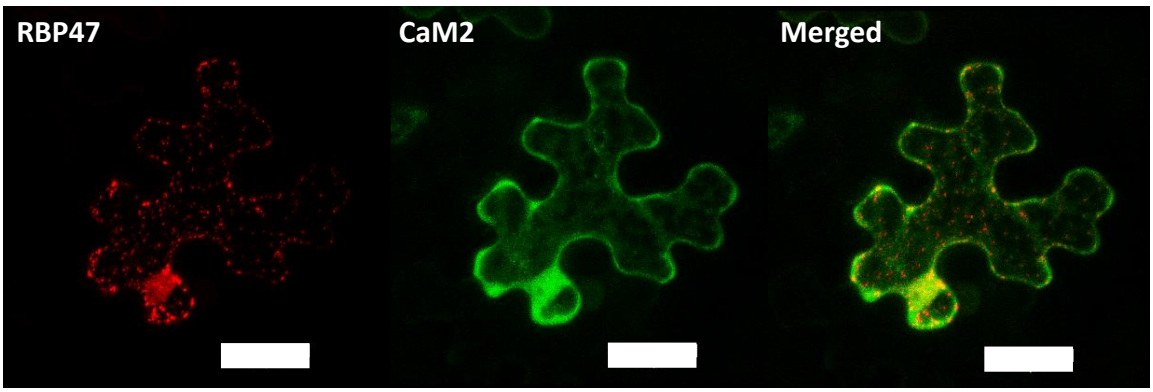

Figure 10 At-CaM2 does not localize to cytosolic foci in response to hypoxia under conditions. Images were taken at 2 hr of hypoxia under the coverslip, under conditions in which RBP47 SGs are evident. Images are shown as 2D projections of a Z-series of 15 optical sections with a Z-step size of 2 µm. Scale bars are 30 µm.

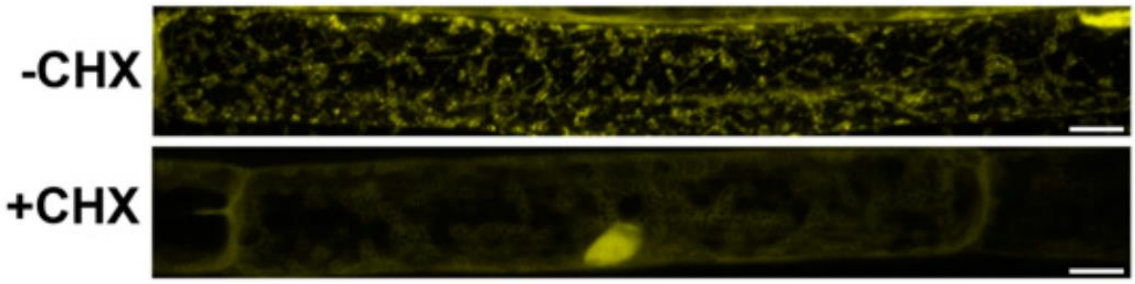

Figure 11 Cycloheximide treatment prevents hypoxia-induced CML38 granule formation. Two-week-old CML38-YFP expressing Arabidopsis seedlings were either treated with cycloheximide (+CHX) or with a DMSO mock treatment (-CHX). Images are confocal micrographs of root cells. Scale bars are 10 µm. These data originally appeared in Lokdarshi *et al.* (2016).

constitute stress granule aggregates (Kedersha et al. 2000, Sorenson et al. 2014). *35S::CML38-YFP* transgenic Arabidopsis seedlings were treated with cycloheximide. As shown in Figure 11, accumulation of CML38-YFP cytosolic granules under hypoxia is blocked by cycloheximide. This suggests that these bodies may be stress granules.

We also investigated if CML38 localizes to another common mRNP granule, the processing body (PB). PBs are enriched in some proteins of gene silencing pathways, such as argonaute 1 (AGO1) and argonaute 2 (AGO2) in animals (Liu et al. 2005), with the same implicated in plants (Maldonado-Bonilla 2014). Since CML38 is a homolog of the silencing suppressor rgsCaM, we hypothesized that CML38 may localize to PBs, and tested for colocalization of CML38 with the processing body-specific marker DECAPPING PROTEIN 1 (DCP1) (Steffens et al. 2014, Chantarachot et al. 2018). CML38-YFP and DCP1-CFP expression constructs were co-transfected into *N. benthamiana*. CML38 strongly colocalized to PBs (Figure 12.)

These observations support the findings of a CML38 immunoprecipitation and tandem mass spectrometry (MS/MS) experiment (Lokdarshi et al. 2016). CML38-YFP was immunoprecipitated from hypoxia-treated transgenic Arabidopsis seedlings using a GFP antibody, and peptides from the immunoprecipitate were analyzed by liquid chromatography followed by MS/MS. The identified proteins would consist of a mixture of some direct CML38 interacting proteins and indirect associating proteins, such as those found in an mRNP along with CML38. Notably, nearly half of the 106 identified proteins are known to reside in mRNPs or to have an RNA processing function (Lokdarshi et al. 2016). These identifications include proteins which are resident to SGs,

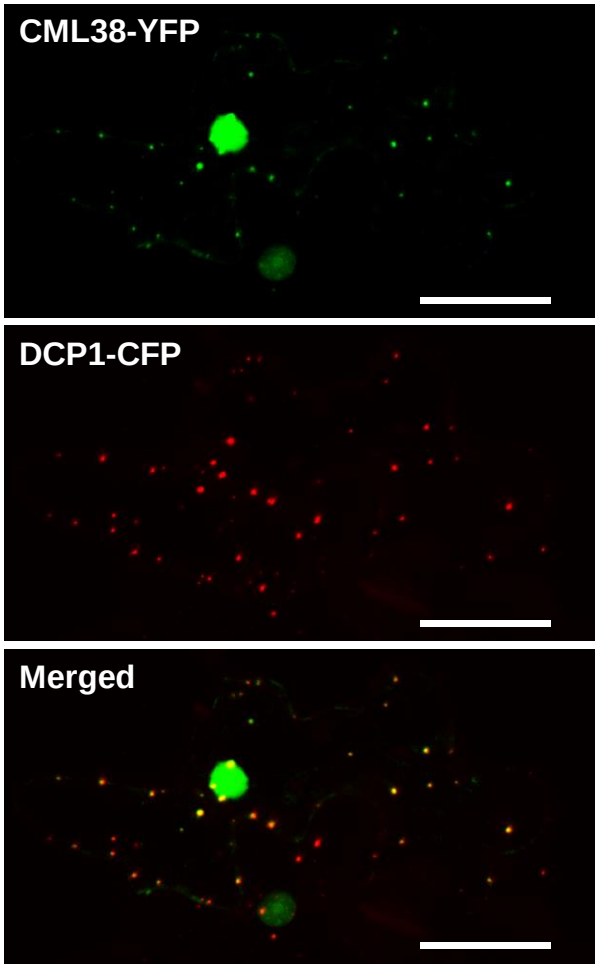

Figure 12 CML38-YFP strongly colocalizes with PB-marker DCP1. Images are 2D projections of 15 optical section from a transfected hypoxic *N. benthamiana* leaf, with a Z-step size of 0.6 µm. Scale bars are 30 µm.

like TUDOR-SN PROTEIN 1 (Yan et al. 2014, Gutierrez-Beltran et al. 2015), and PBs, like VARICOSE (Weber et al. 2008), as well as several each from the 60S and 40S ribosomes (Lokdarshi et al. 2016).

3.2 Subcellular localization of Nicotiana tabacum regulator of gene silencing calmodulin

The finding that CML38 is a core hypoxia protein that is necessary for hypoxia stress survival suggests a potential function in mitigating the low oxygen-induced energy crisis associated with anaerobic stress (discussed in Lokdarshi et al. (2016)). However, mechanistic details regarding such a role in stress and RNA biology remain unknown. Observation of SG and PB localization let to the proposal that CML38 may regulate the dynamics of mRNP particles, or the function of resident proteins as a means of affecting gene expression at the RNA level, and to regulate the energy expensive process of mRNA translation or other aspects of RNA metabolism (Lokdarshi et al. 2016). Support for a role in regulation of RNA homeostasis is provided in part by the observation that CML38 homolog, tobacco rgsCaM, suppresses post-transcriptional gene silencing (Anandalakshmi et al. 2000). Since CML38 localizes to mRNP bodies, and rgsCaM interferes with post-transcriptional gene silencing, both proteins are implicated in RNA functions. Further, the RNA-induced silencing complex (RISC), as well as small interfering RNAs, are also known to accumulate within cytosolic mRNP bodies (Sen et al. 2005, Jouannet et al. 2012). This suggests that CML38 and rgsCaM may both function within mRNP bodies. To better understand how these proteins function, we set

initially set out to determine if rgsCaM shows the same localization to SGs and PBs as CML38.

3.3 Nicotiana tabacum regulator of gene silencing calmodulin localizes to hypoxia-induced granules

To determine the localization of *Nicotiana tabacum* rgsCaM, we cloned *rgsCaM* into the pEarleyGate 101 plasmid, as was previously described for *CML38.* Examination of rgsCaM-YFP localization in *N. benthamiana* transfected leaves reveals the localization to cytosolic foci similar to granule structures observed with CML38 (Figure 13). Nuclei were stained with 4',6-diamidino-2-phenylindole (DAPI), and images were taken after 2 hr of hypoxia (Figure 13). Much like CML38, rgsCaM-YFP localized to the nuclear compartment as well as to cytosolic foci.

To determine whether these rgsCaM foci are constitutive or whether they are induced by hypoxia stress, a time series of images was taken after hypoxia was induced (Figure 14.) Fifteen min after slide preparation, a few rgsCaM granules are present (Figure 14), but the signal is largely diffuse, similar to CML38 (Figure 8). However, rgsCaM fluorescence shows a redistribution into cytosolic foci with a clear time-dependent increase in granule number evident over the 30 min, 50 min and 70 min timepoints (Figure 14).

Colocalization experiments were conducted with the SG marker RBP47 to determine whether rgsCaM is associated with cytosolic SG mRNPs (Figure 15). Unlike CML38, rgsCaM granules were predominantly localized to independent foci that were distinct from SGs (Figure 15). This is supported by co-localization quantification with a

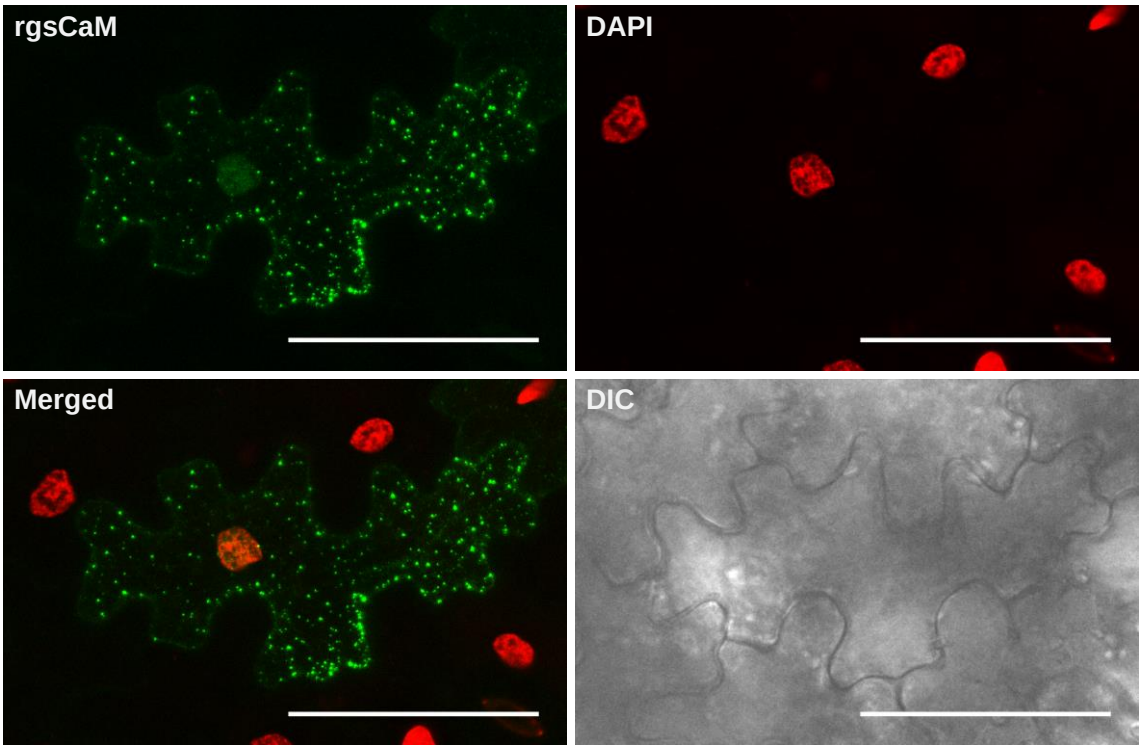

Figure 13 Localization of rgsCaM-YFP to cytosolic granules in *N benthamiana* leaf cells. *N benthamiana* leaves were transfected with *35S::rgsCaM-YFP* by *Agrobacterium* infiltration. Leaf sections were placed under a coverslip ("wet mounted") and were visualized by confocal microscopy after 2 hr to allow for the induction of hypoxia. Nuclei were stained with DAPI. Images are 2D-projections of 20 optical sections with a 1.4 µm step size. Scale bars are 50 µm.

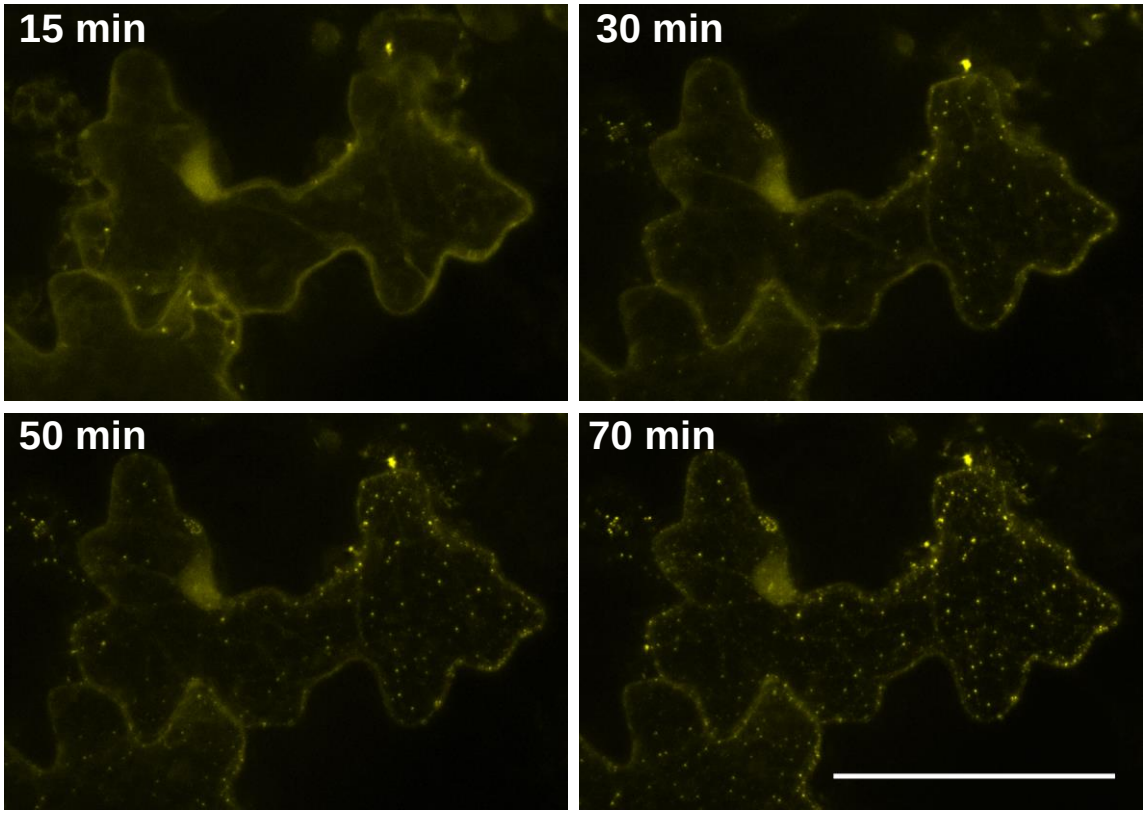

Figure 14 RgsCaM-YFP time series of granule formation in response to hypoxia. A representative cell from a transfected *N. benthamiana* leaf expressing rgsCaM-YFP. The tissues were wet mounted and imaged over time. Images are maximum intensity 2D projections of a Z-series consisting of 20 optical sections and a step size of 1.3 µm. Scale bar is 50 µm.

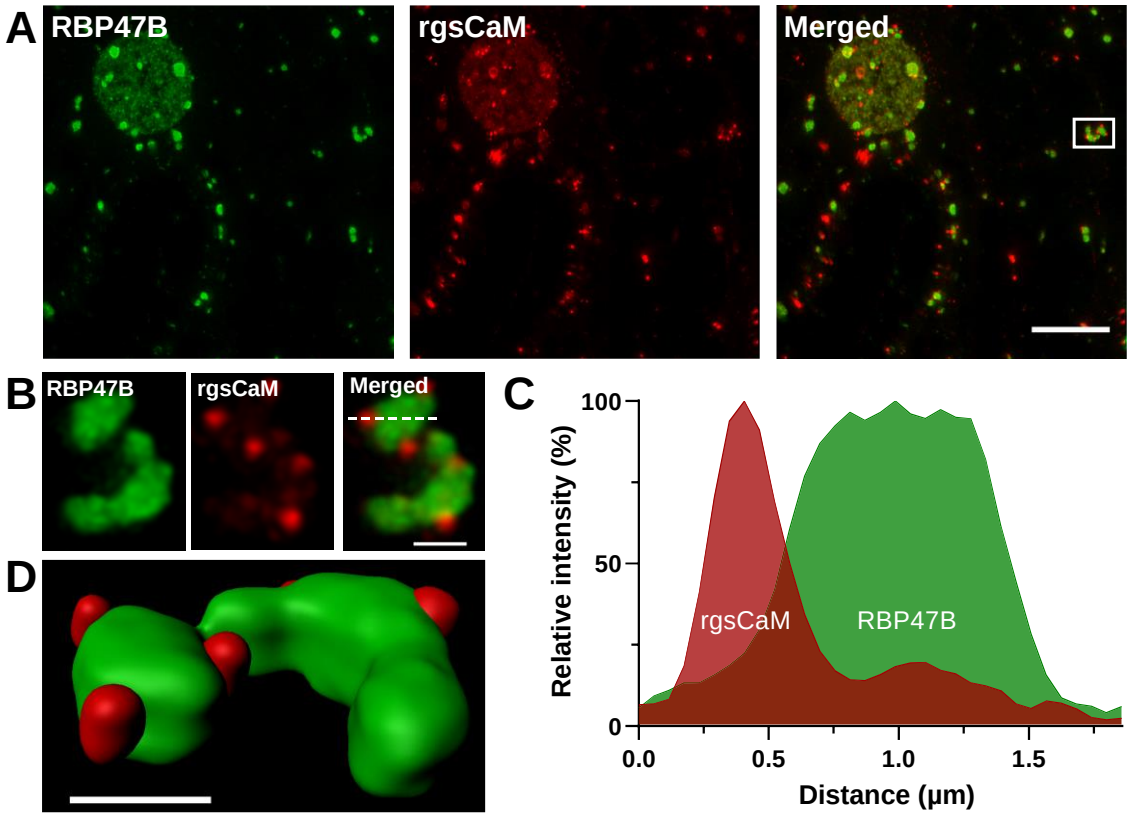

Figure 15 Co-localization of rgsCaM-YFP and RBP47B-CFP. Leaf sections of *N. benthamiana* leaves co-transfected with constructs that express rgsCaM-YFP and the stress granule marker RBP47B-CFP. **A)** 2D projections from a representative cell, consisting of 99 optical sections with a step size of 0.3 µm. Images were captured after 2 hr after the onset of hypoxia and were subjected to standard deconvolution as described in the Materials and Methods. Scale bars are 10 µm. **B)** Magnification of boxed region shown in panel A. Scale bar is 1 µm. A smoothing filter was applied in Leica LAS X software. **C)** A line plot profile of fluorescence intensities calculated along the axis shown by the dashed line in B as described in the Materials and Methods. **D)** 3D model reconstruction from the dataset shown in B using the Imaris software. Scale bar is 1 µm.

Pearson correlation coefficient of <0.5 (0.47) and low Manders' coefficients (0.12 and 0.18) obtained for rgsCaM and RBP47B.

However, a closer examination of the stress granule aggregates showed the apparent association of smaller rgsCaM foci at the periphery of stress granules. An example of this peripheral localization is enlarged in Figure 15B, which shows a cluster of SGs and five associating rgsCaM granules. To obtain high quality imaging data, 99 optical sections were taken with a Z-step size of 0.3 µm, and deconvolution was performed (Huygens Essentials software, Scientific Volume Imaging). A line plot profile was generated to show the fluorescence intensity for each channel (Figure 15C) through the white dotted line in Figure 15B. The line plot shows that even after deconvolution these objects are close enough to have some overlap in their fluorescence intensities at the interface, yet the maxima are clearly distinct (Figure 15C). A three-dimensional model was generated from the volumetric signal intensities in the Z-stack using Imaris software (Oxford Instruments) (Figure 15D; Figure 16). These data indicate that rather than localizing within SGs, rgsCaM appears to be bound at the surface of SGs under hypoxia stress, as well as to independent foci.

We next tested if rgsCaM localizes to DCP1-marked processing bodies. *N. benthamiana* was co-transfected with DCP1-CFP and rgsCaM-YFP plasmids, and imaged after 1 hr 15 min of hypoxia, conditions sufficient for the formation of rgsCaM granules. The results showed that rgsCaM largely localized to small cytosolic foci, with nuclear localization also observed. However, rgsCaM also showed apparent co-localization with DCP1 within large cytosolic foci that are characteristic of processing

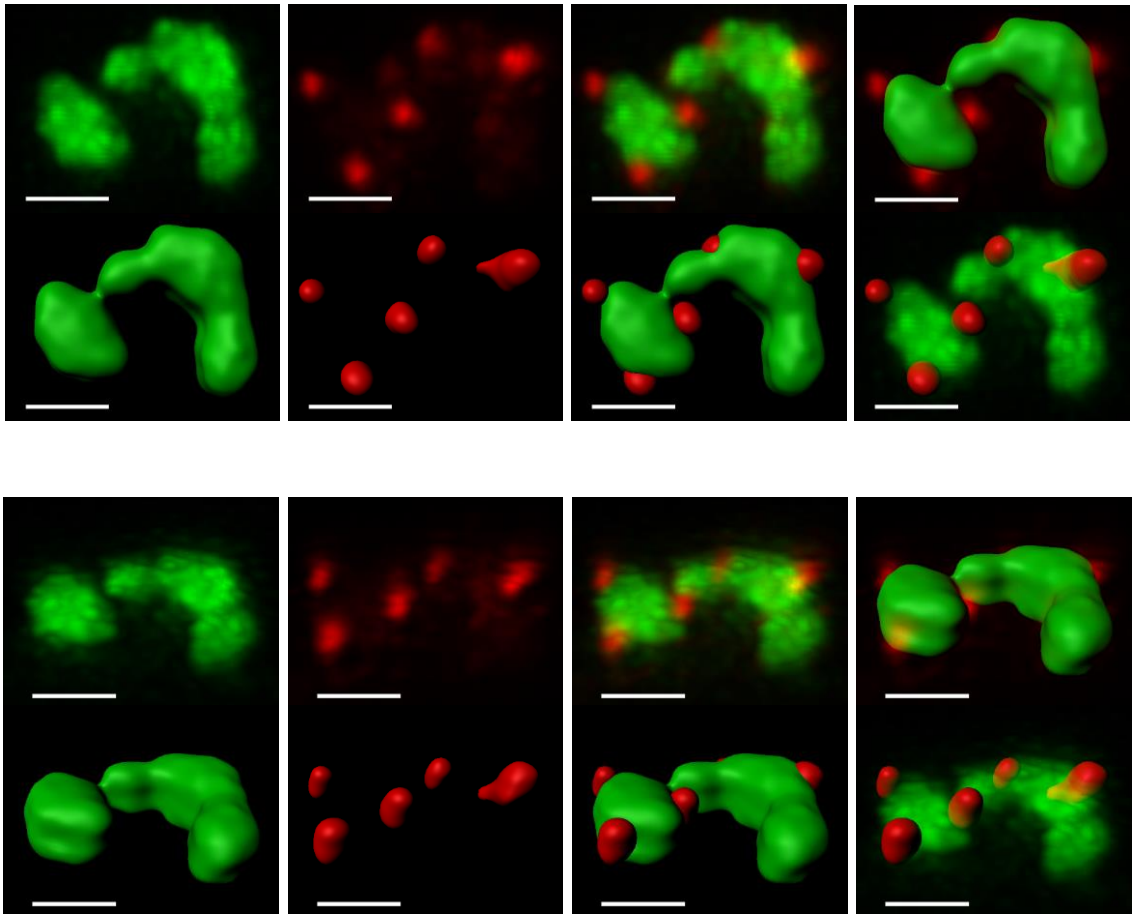

Figure 16 Fitting of SG-marker RBP47B and rgsCaM imaging data to 3D models. Deconvolved, volumetric fluorescence signals from a Z-series of confocal micrographs of RBP47B (green) and rgsCaM (red) is shown opposite the fitted models from Imaris. Two perspectives are shown (top and bottom panels). Each panel shows a different combination of fluorescence data and/or models. Scale bars are 1 µm.

bodies (Figure 17). The co-localization in the cytosol has a Pearson's correlation coefficient of 0.368, below the 0.5 threshold for a strong correlation. However, this may have been the result of a large number of rgsCaM granules that do not associate with DCP1. To obtain a more nuanced assessment of co-localization, Manders co-localization techniques were employed. Manders' colocalization coefficients (MCC) are more informative in cases in which one protein strongly colocalizes to the second, but the second is also abundant in independent sites. The $MCC_{DCP1:rgsCaM}$ for DCP1 overlapping with rgsCaM is 0.96, while the $MCC_{rgsCaM:DCP1}$ for rgsCaM overlapping with DCP1 is 0.08. This reflects the observation that PBs overwhelmingly have rgsCaM association, but the majority of rgsCaM granules are independent from DCP1 marked processing bodies (Figure 17).

Closer examination of rgsCaM-localizing PBs revealed that while there is a strong co-localization at low magnifications (Figure 17), higher resolution imaging revealed that rgsCaM is predominantly localized as rgsCaM bodies at the periphery of larger PB (Figure 18). High resolution imaging under hypoxic conditions and deconvolution identified a tight ring of rgsCaM around PBs (Figure 18A-B). This is also evident in a line-plot profile, which shows that the rgsCaM bodies have a fluorescent signal maximum outside the PB, and are close enough to show some signal overlap with DCP1-CFP (Figure 18C). Three-dimensional modeling of the volumetric intensities from a Z-stack of images through a representative PB was performed in Imaris (Figure 18D; Figure 19). rgsCaM bodies appear to incompletely surround the PB in three dimensions, and the irregular shapes and sizes may be indicative of fusion at the PB surface (Figure 19).

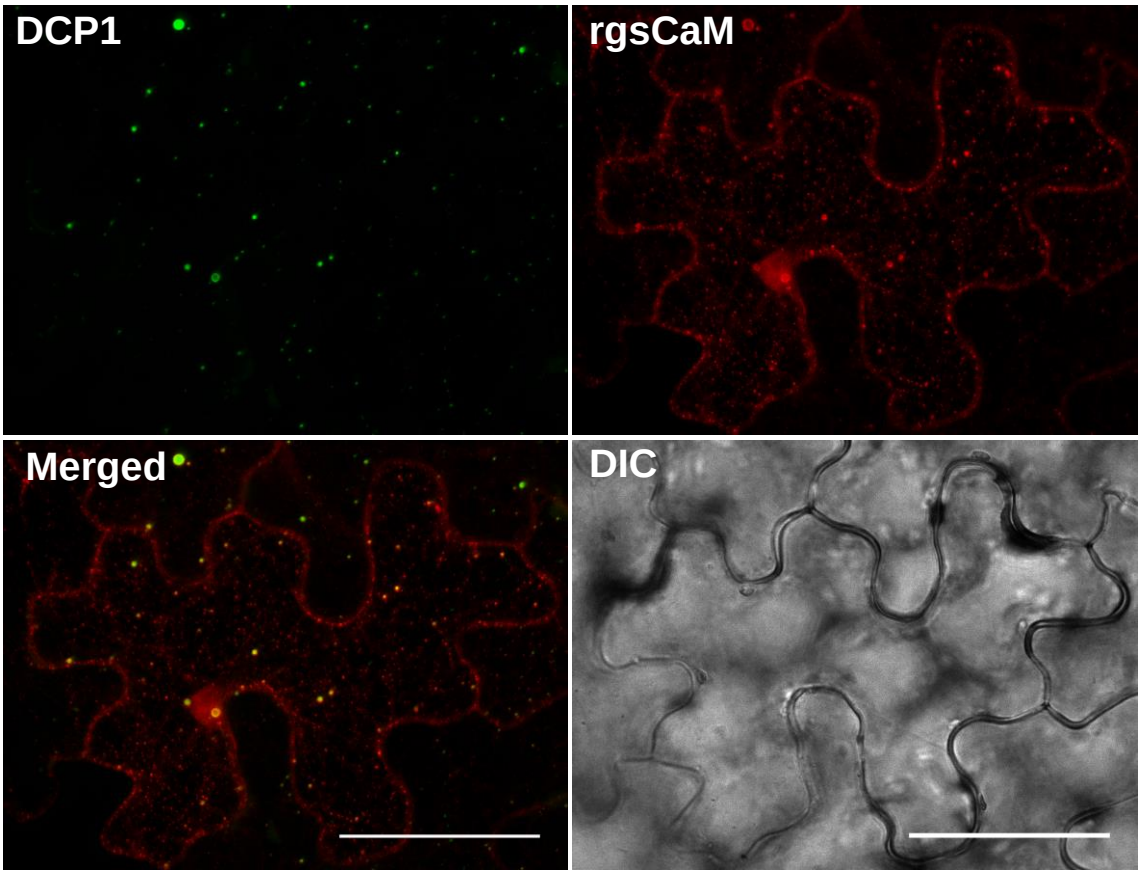

Figure 17 Co-localization of rgsCaM-YFP and processing body markers in hypoxic *N. benthamiana* leaves. Leaf sections of *N. benthamiana* leaves co-transfected with constructs that express rgsCaM-YFP and the processing body marker DCP1-CFP. Two-dimensional projection of 25 optical sections with a step size of 1.5 µm from a cell subjected to 75 min of hypoxia is shown. Scale bar is 50 µm.

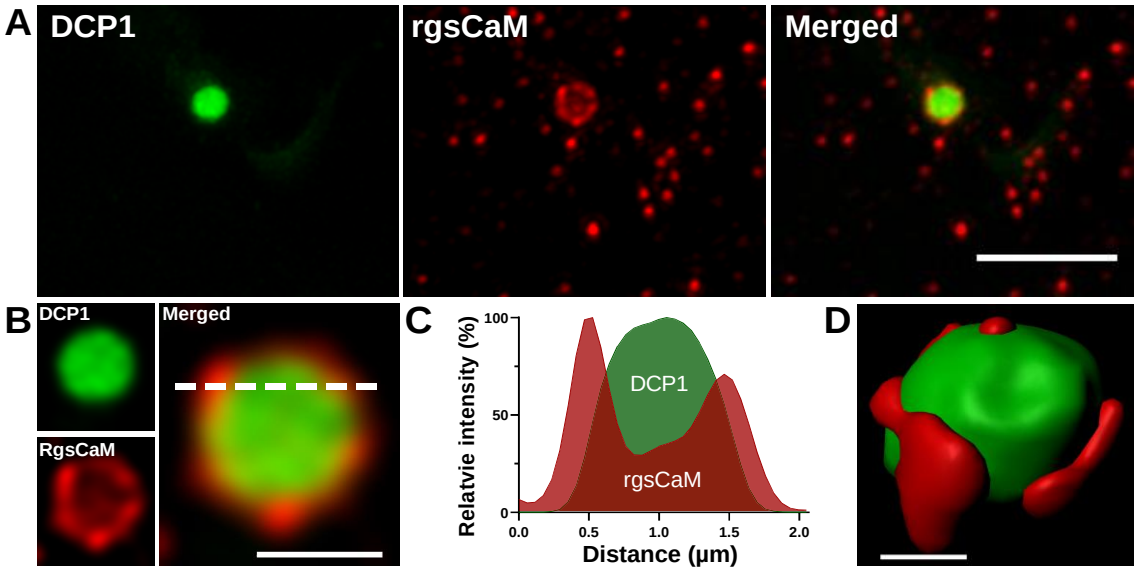

Figure 18 Processing body marker DCP1-CFP colocalization with rgsCaM-YFP in *N. benthamiana* leaves. A) A higher resolution two-dimensional projection from 27 optical sections (0.3 µm step size) of a representative processing body structure from a *N. benthamiana* cell co-transfected with *DCP1-CFP* and *rgsCaM-YFP* as described previously. Leaf sections were subjected to 1 hr 45 min of hypoxia before imaging. The image was subjected to standard deconvolution as described in the Materials and Methods. **B)** Magnification of the body shown in A. A smoothing filter was applied in Leica LAS X software. Scale bar is 1 µm. **C)** A line profile for the fluorescence intensities through the dashed line shown in B. **D)** 3D model constructed from the dataset shown in A-B using Imaris. Scale bar is 0.5 µm.

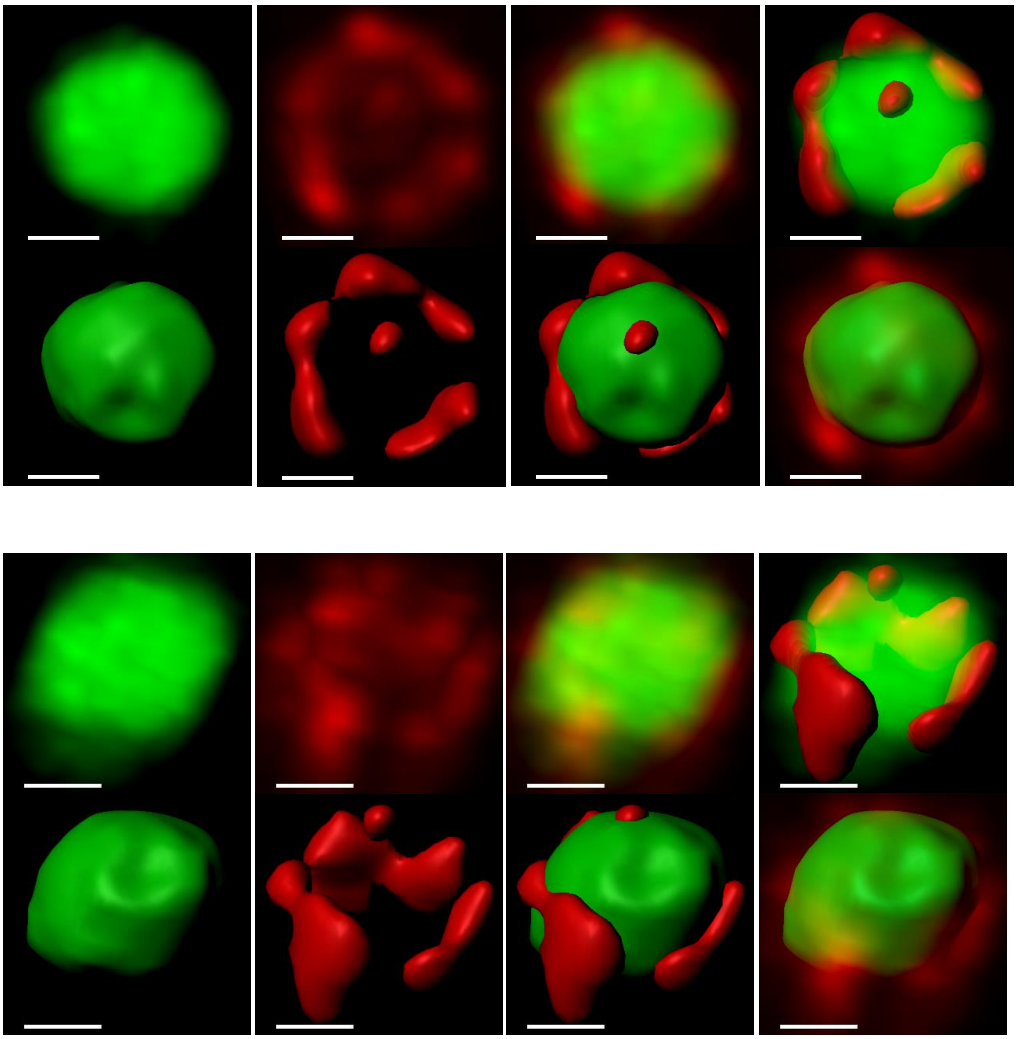

Figure 19 Fitting of PB-marker DCP1 and rgsCaM imaging data to 3D models. Volumetric fluorescence signals from a Z-series of confocal micrographs for DCP1 (green) and rgsCaM (red) is shown opposite the fitted models in Imaris. Two perspectives are shown (top and bottom panels), and each image shows a different combination of deconvolved fluorescence intensities and/or models. Scale bars are 0.5 µm.

Results from rgsCaM colocalization with RBP47 (Figure 15) and DCP1 (Figure 18) resemble granule docking. It is well-established that SGs and PBs show transient docking, which presumably facilitates the transfer of translationally arrested mRNA from SGs into PBs for degradation (Protter et al. 2016). These associations observed for rgsCaM bodies bound to SG or PB were apparently stable under these experiments. This is seen both from the accumulation of these rgsCaM peripheral granules in Figure 15 and Figure 18, but also in a live cell imaging movie that was recorded, which shows an rgsCaM granule traffic to and remain in contact with a DCP1 processing body (shown here as Figure 20.) From t=0 sec, the rgsCaM granule moves a distance of 4 µm, and docking at the PB surface occurs at t=1 min. However, the stable association was recorded up to 3.5 min with no change. The PB in the first frame is slightly out of the focal plane so the smaller PB is not visible. These findings indicate that rgsCaM granules traffic to SGs and PBs and become bound at the surface, accumulating over the hypoxia duration.

RgsCaM and CML38 colocalize with Suppressor of Gene Silencing 3 within SGs

Previous observations show that rgsCaM associates with the protein product of *Suppressor of Gene Silencing* 3 (Li et al., 2017). SGS3 has previously been shown to associate with cytosolic granule structures referred to as SGS3/RDR6 bodies, or siRNA bodies (Kumakura et al. 2009). siRNA bodies are known to contain SGS3, RDR6, AGO7, and also an example of a viral protein needed for replication, VP6 (Jouannet et al. 2012), as well as some SG components (Jouannet et al. 2012). To investigate further the localization of SGS3 in response to hypoxia stress, the protein was expressed as a

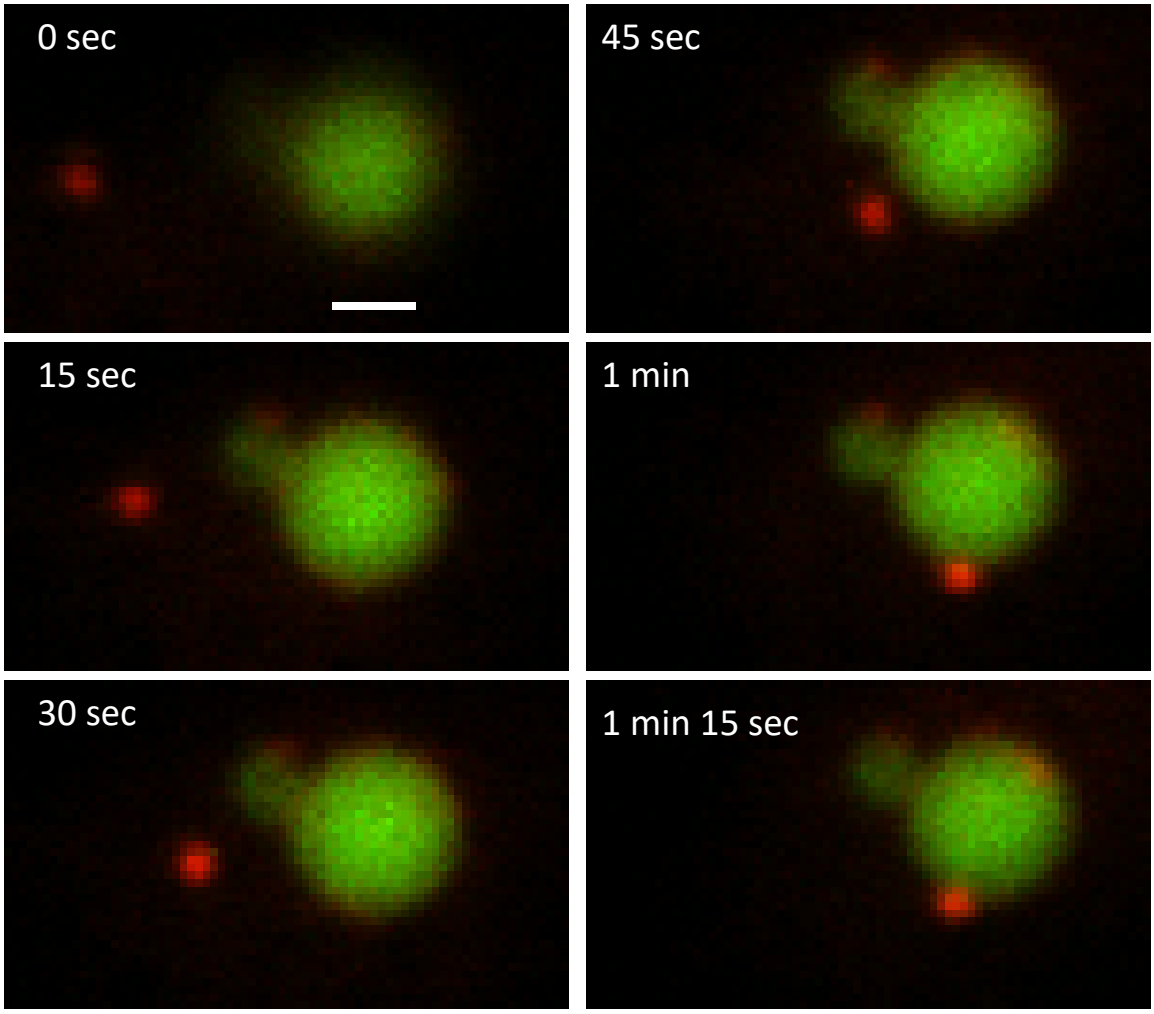

Figure 20 rgsCaM granule docking onto DCP1 processing body. rgsCaM-YFP body (red) trafficking to a DCP1-CFP PB (green) over a time series. The images come from co-transfected *N. benthamiana* leaves after 2 hr of hypoxia. Single optical sections are shown. Scale bar is 1 µm.

CFP fusion *N. benthamiana* (Figure 21). While a small number of SGS3 granules were present at 10 min after slide preparation, this number dramatically increased through the remaining time points at 45 min and 95 min as hypoxia increases (Figure 21). These observations show that SGS3 granules, similar to SG, are induced during hypoxia.

Next, we performed co-localization between rgsCaM and SGS3 in response to hypoxia to determine if they co-localize to hypoxia-induced granules. This was performed as in previous assays, using SGS3-CFP and rgsCaM-YFP. rgsCaM strongly colocalized with hypoxia-induced SGS3-CFP granules (Figure 22).

Since some SGS3 granules are present in unstressed conditions during while rgsCaM and CML38 are diffuse, we compared the granulation kinetics of SGS3 and rgsCaM under hypoxia (Figure 23). The representative cell in Figure 23 was imaged after 30 min of hypoxia and again after 90 min. SGS3 granules were abundant at 30 min of hypoxia, more than what is seen at hypoxia onset (10 min hypoxia, Figure 21), while rgsCaM showed no granulation after 30 min. This suggests that the SGS3 granule number increases during hypoxia prior to rgsCaM granulation. By 90 min of hypoxia, both proteins apparently fully colocalize (Figure 23) with high Manders' coefficients of co-localization ($MCC_{SGS3:rgsCaM}$ = 0.87, while the $MCC_{rgsCaM:SGS3}$ = 0.95).

High resolution imaging with the Leica Lightning de-convolution system revealed two patterns of co-localization (Figure 24). In one, the rgsCaM signal is virtually superimposable with the SGS3 signal, with a slightly higher rgsCaM intensity calculated at the periphery of the granule (Figure 24B-C). In the second, a pattern similar to that

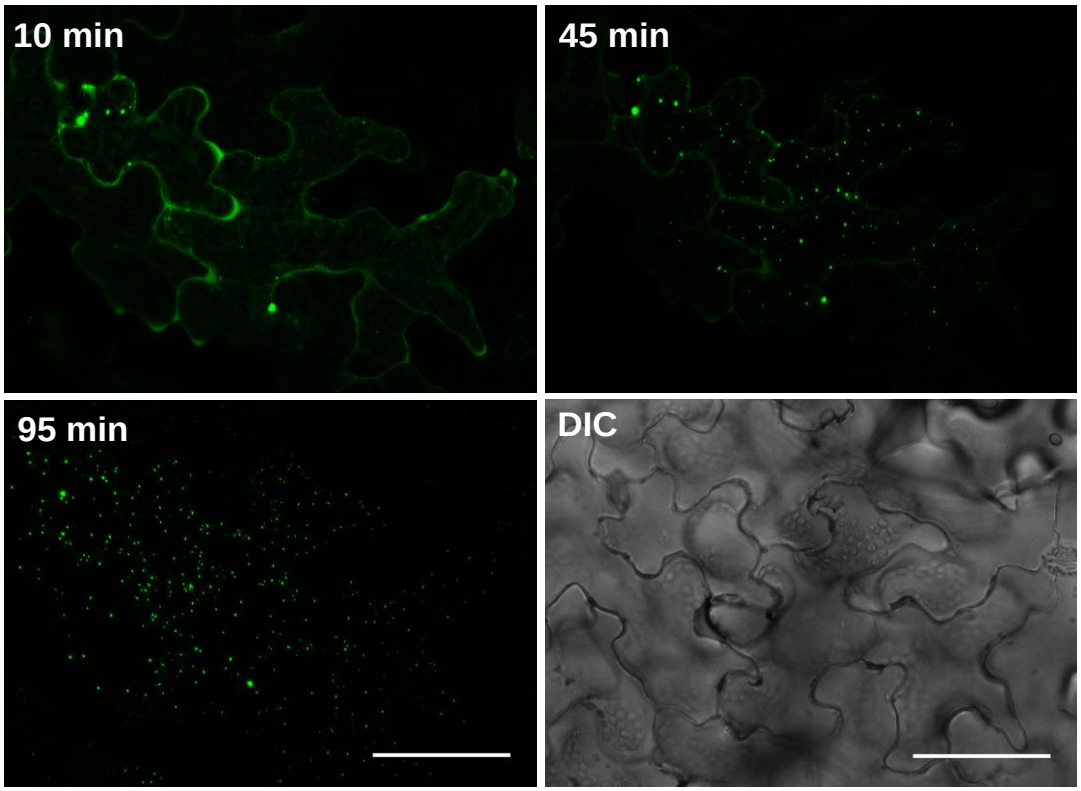

Figure 21 SGS3 localization time course in *N. benthamiana* leaves. Leaf sections of *N. benthamiana* were co-transfected with constructs that express rgsCaM-YFP and the SG-marker SGS3-CFP and were subjected to a hypoxia (durations indicated). Images are 2D projections from 20 optical sections with a 2 µm step size. Scale bar is 50 µm.

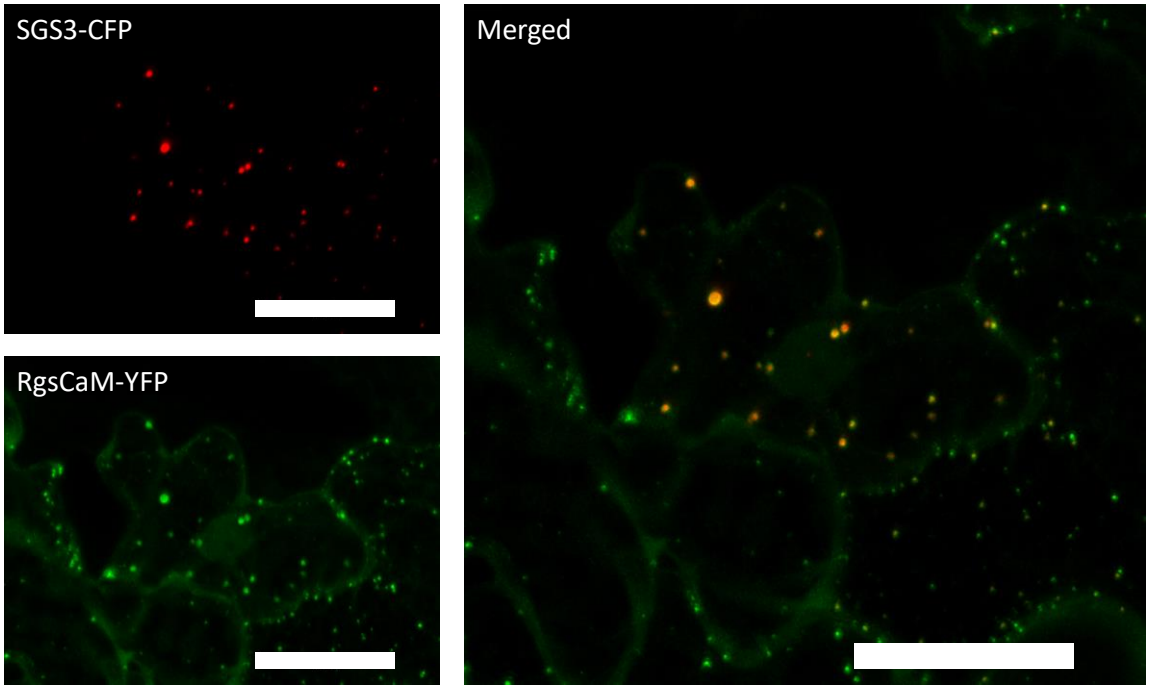

Figure 22 rgsCaM associates with cytosolic SGS3 granules. SGS3-CFP and rgsCaM-YFP were expressed in *N. benthamiana.* Images were taken at 1 hr of hypoxia and are shown as 2D projections of 22 optical sections with a step size of 1.5 µm. Scale bars are 30 µm.

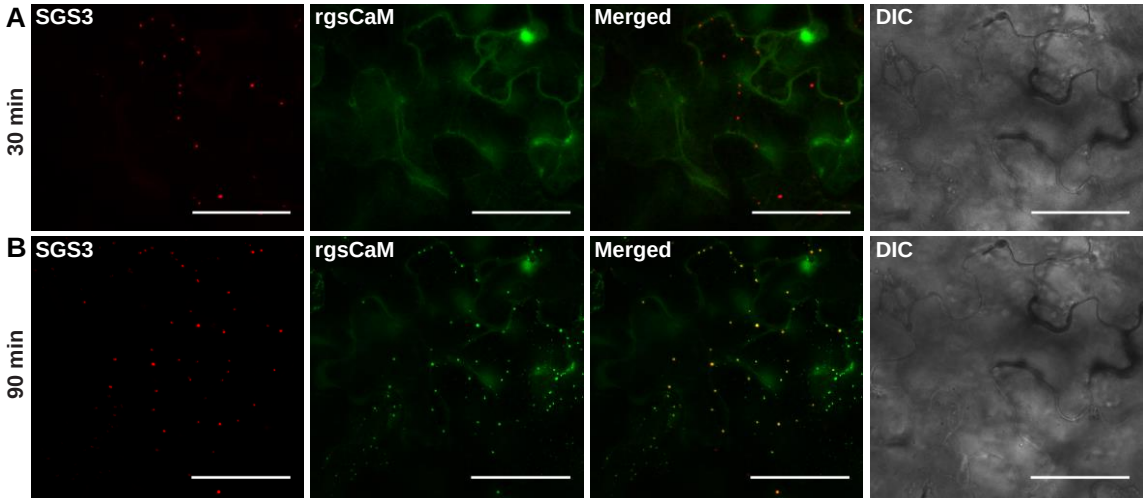

Figure 23 SGS3 granules form before rgsCaM granules. SGS3-CFP hypoxia-induced foci appear before rgsCaM-YFP foci (30 min), but with longer hypoxia duration (90 min) rgsCaM-YFP strongly colocalizes. Images are 2D projections of 6 optical sections with a step size of 2 µm. Scale bars are 50 µm.

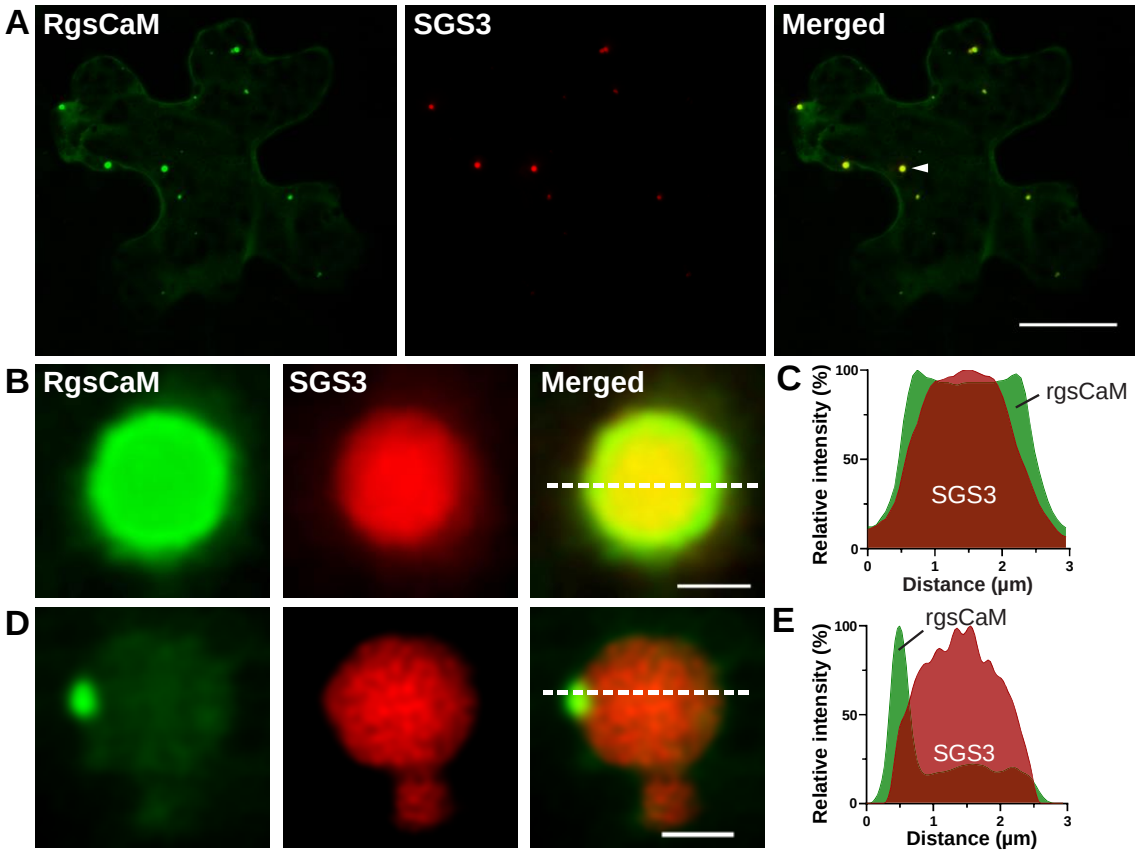

Figure 24 Colocalization of rgsCaM-CFP and SGS3-YFP. **A)** Representative co-expressing *N. benthamiana* cell following 1 hr 20 min of hypoxia. The images are 2D projections of 27 optical sections with a 1 µm step size. Scale bar is 30 µm. **B)** Enlargement of the granule in A marked with the arrowhead, shown with a 1 µm scale bar and a smoothing filter in LAS X. **C)** Line plot profile of fluorescence intensities through the dashed line in B. **D)** In a separate experiment, Lightning deconvolution was performed on SGS3 and rgsCaM bodies after 1 hr 20 min of hypoxia. Scale bar is 1 µm. **E)** Line plot profile of fluorescence intensities through the dashed line in D.

observed with SG and PB co-localization was observed in which a small rgsCaM granule appears to be bound at the periphery of an SGS3 body (Figure 24D-E). This indicates that while rgsCaM localizes within SGS3 granules, this does not preclude the peripheral localization that was observed for rgsCaM with Figure 15 and Figure 18.

3.4 Suppressor of Gene Silencing 3 shows strong co-localization with SG and increases rgsCaM localization to these structures

To investigate the potential relationship between hypoxia-induced SGS3 granules and PBs and SGs, co-localization experiments were conducted with DCP1 and RBP47B markers. Under hypoxic conditions, SGS3 and DCP1 localize to distinct cytosolic foci (Figure 27) and had low co-localization coefficients ($MCC_{DCP1:SGS3}$ = 0.11 and $MCC_{SGS3:DCP1}$ = 0.12). This agrees with previous findings with heat stress-induced SGS3 granules which showed that SGS3 bodies are distinct from PBs (Kumakura et al. 2009). In contrast, SGS3 nearly fully colocalizes with SGs (Figure 25; Figure 26), yielding high colocalization coefficients ($MCC_{RBP47B:SGS3}$ = 0.94 and $MCC_{SGS3:RBP47B}$ = 0.88). High resolution imaging of SGS3-YFP and RBP47-CFP bodies were virtually superimposable (Figure 26B-C), suggesting that hypoxia-induced SGS3 granules may be identical to SGs.

To test the hypothesis that SGS3 causes rgsCaM to relocalize to SGs, we conducted high resolution confocal imaging and deconvolution on a colocalization assay of SGS3-CFP, RBP47B-RFP, and rgsCaM-YFP, at 5 hr of hypoxia (Figure 28). This

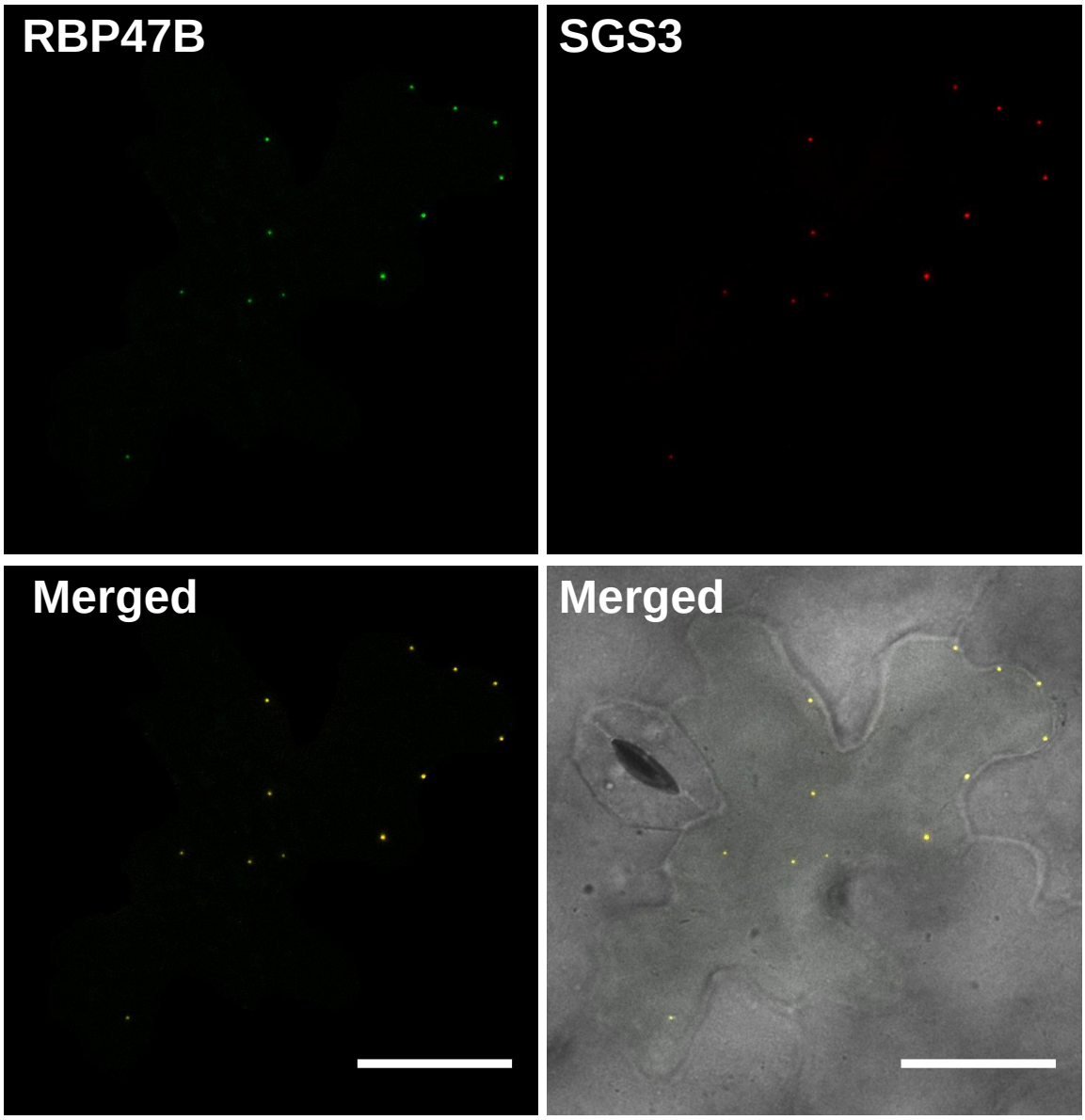

Figure 25 Colocalization of RBP47B and SGS3. Images were taken after 3 hr of hypoxia and are 2D projections of 20 optical sections with 1 µm step size. Scale bars are 30 µm.

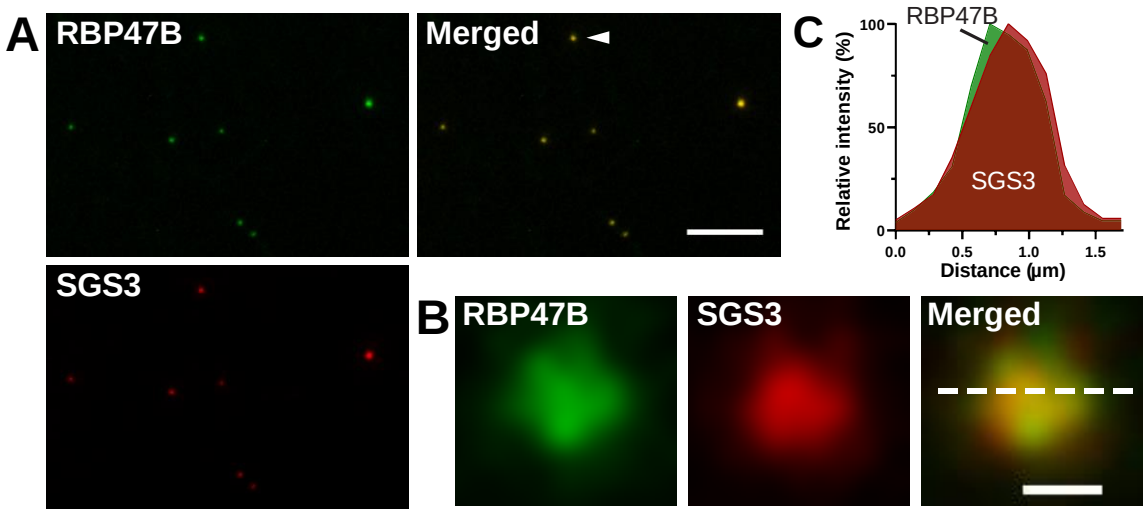

Figure 26 SGS3 and RBP47 colocalization in *N. benthamiana* cells. **A)** Representative co-expressing cell following 3 hr of hypoxia. Images are 2D projections of 20 optical sections with a step size of 1 µm. Scale bar is 10 µm. **B)** Magnification of the granule marked by the arrowhead in A, with a smoothing filter applied in Leica LAS X. Scale bar is 0.5 µm. **C)** Line plot profile though the dashed line in B, based on raw data.

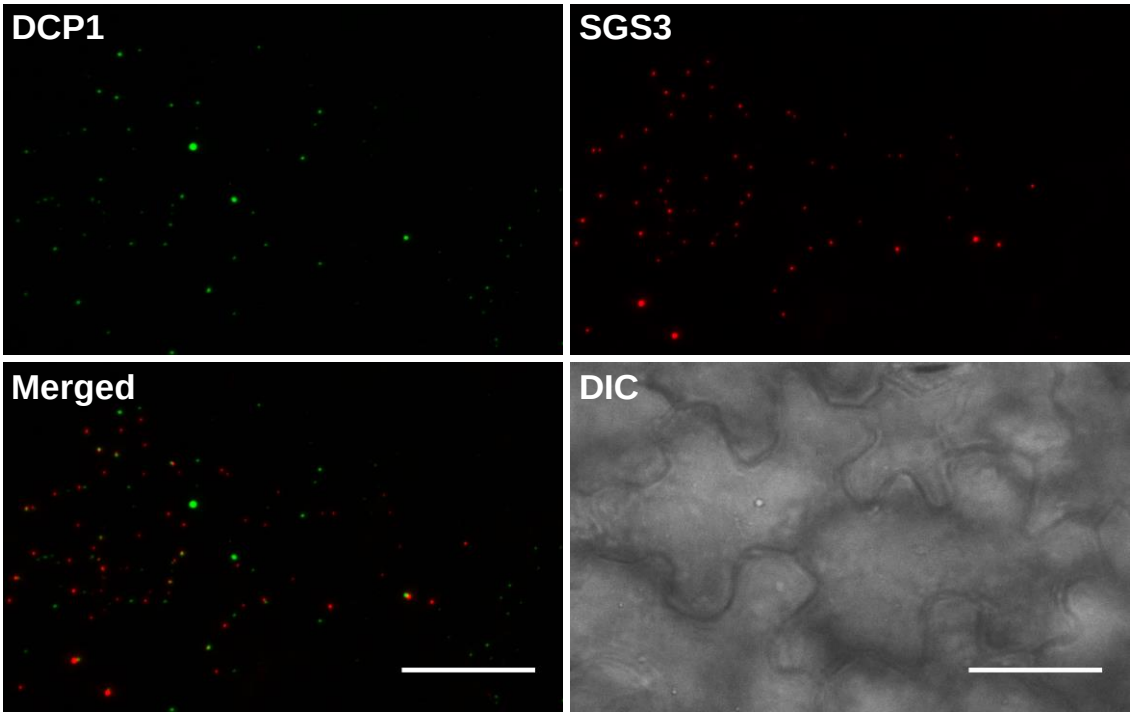

Figure 27 SGS3 and DCP1 colocalization in *N. benthamiana* leaves. Images are 2D projections of 20 optical sections with a step size of 1 µm. Scale bar is 50 µm. Hypoxia time was 4 hr. No deconvolution was performed.

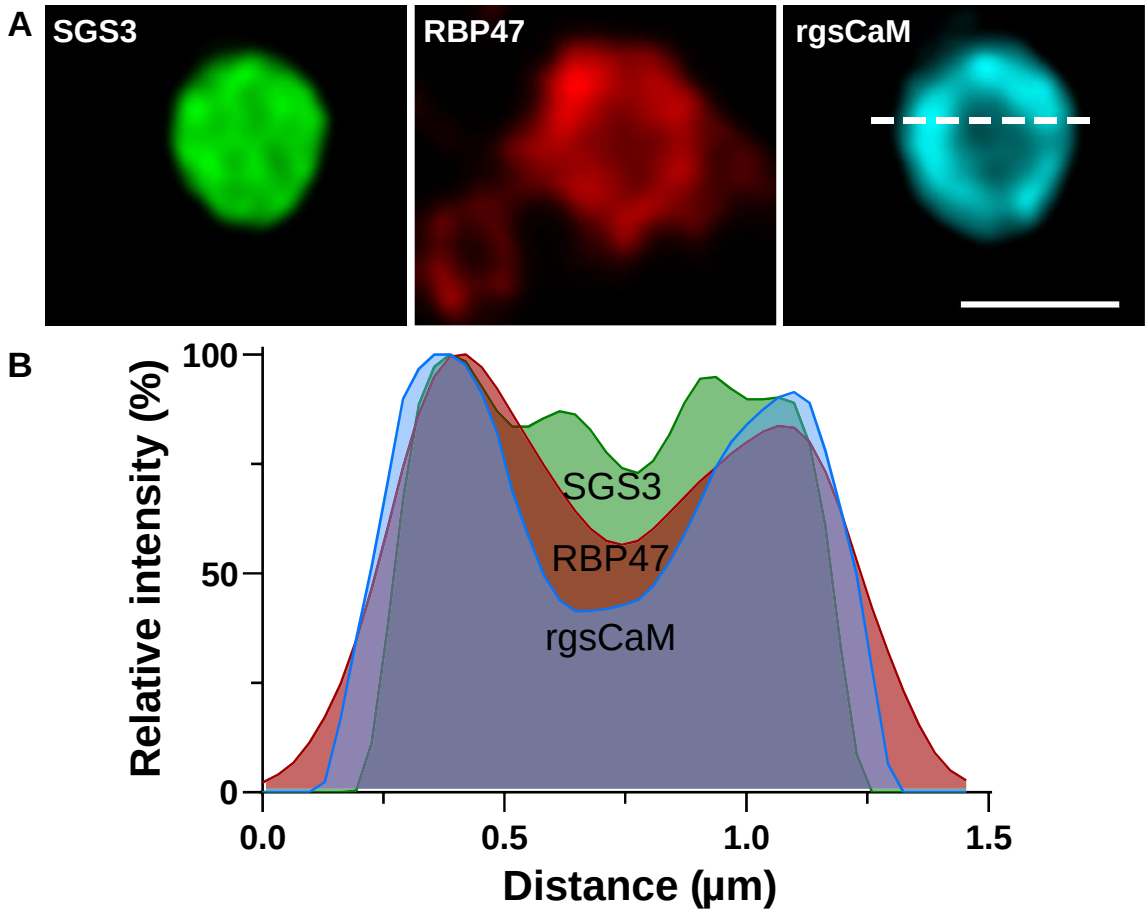

Figure 28 Colocalization of SGS3-CFP, RBP47-RFP and rgsCaM-YFP in *N. benthamiana*. A) Images were taken 5 hr after slide preparation and are 2D projection of 4 optical sections with a Z-step size of 0.13 µm. Scale bar is 1 µm. The Lightning deconvolution system was used, and an additional smoothing filter was applied in LAS X. B) Line plot through the dashed line in C generated from unfiltered data.

showed a different pattern with respect to rgsCaM and SGS3 than the shorter hypoxia durations in the previous colocalization experiments. Both RBP47 and rgsCaM show enhanced peripheral localization relative to an SGS3-enriched core (Figure 28A-B). Possible reasons for this will be discussed further in the discussion section.

Given the similarity between CML38 and rgsCaM, and previous observations of CML38 association with hypoxia-induced granules, we conducted a similar co-localization experiment with CML38 and SGS3 to determine if they co-localize. As shown in Figure 29, CML38 shows strong co-localization with SGS3, suggesting that, like rgsCaM, it may constitute an interaction target. As a negative control, we did the same experiment with Arabidopsis calmodulin 2 (CaM2) which is a *bona fide* calmodulin that is not found in the rgsCaM clade. Following 2 hr of hypoxia, CaM2 showed no colocalization with SGS3, and showed no granulation despite constitutive expression of SGS3 (Figure 30).

3.5 rgsCaM and CML38 are implicated in autophagy and contain putative ATG8-interacting motifs in their N-termini

In light of reports that rgsCaMs target direct-binding proteins (and those in the same complex) for autophagic degradation, our results showing SG and PB association may indicate that rgsCaMs function to degrade these mRNPs during hypoxia stress or recovery. Since rgsCaM was degraded along with its targets (Nakahara et al. 2012, Li et al. 2017), we also investigated whether rgsCaMs may act as autophagy cargo adaptors which directly bind to AUTOPHAGY RELATED GENE 8 (ATG8) on autophagosomes. ATG8 has a ubiquitin fold and is cleaved near its C- terminus and conjugated onto

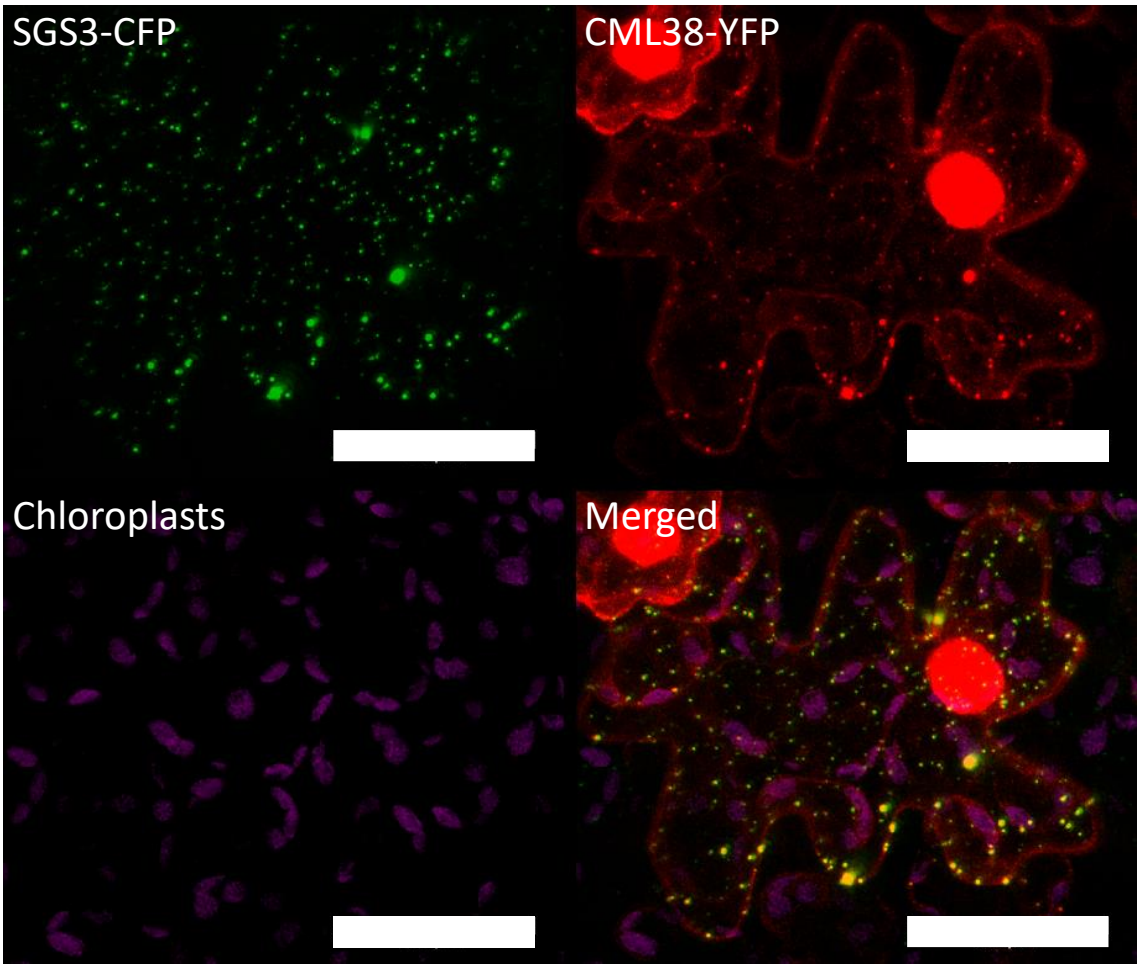

Figure 29 At-CML38 also colocalizes with SGS3 in hypoxia-induced cytosolic foci. *N. benthamiana* leaves were transfected to express SGS3-CFP and CML38-YFP. Images were taken after 40 min of hypoxia. Colocalization for the representative, central co-expressing cell has a Pearson's coefficient of 0.758. Scale bar is 30 μm.

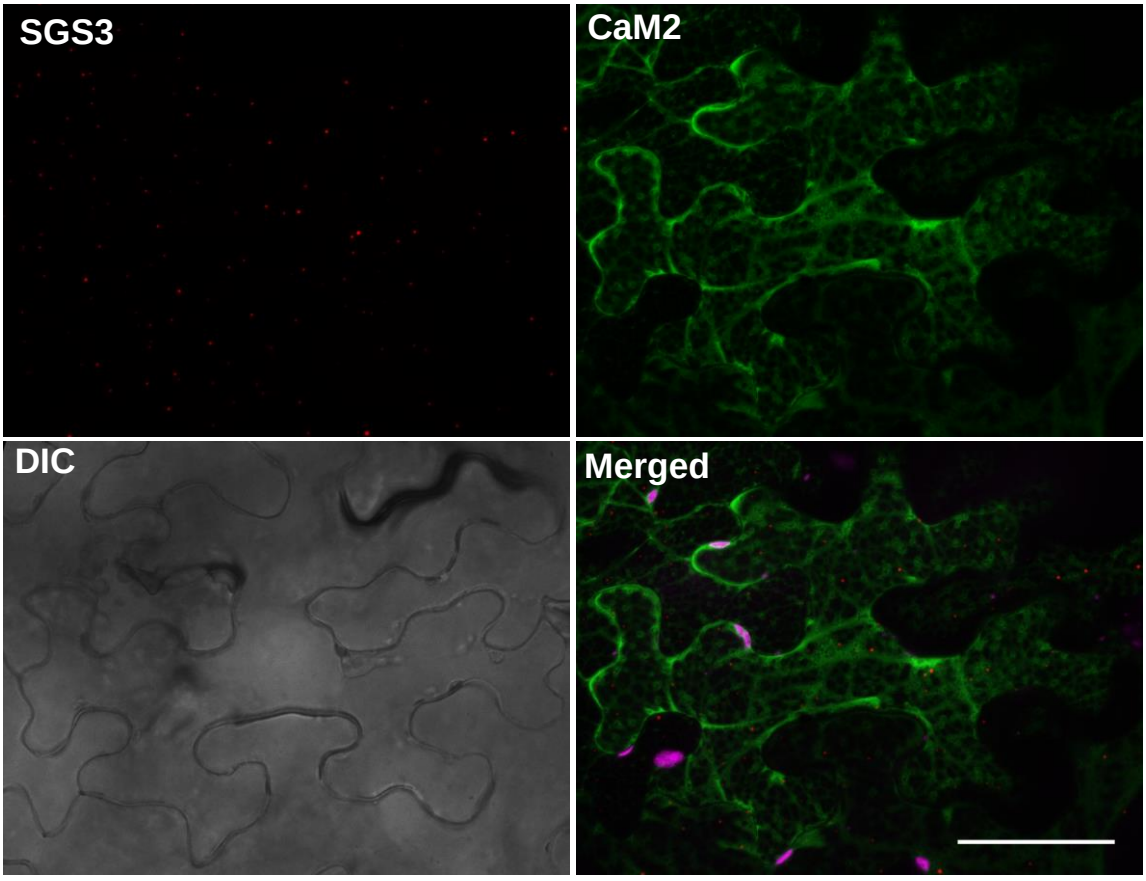

Figure 30 CaM2 does not localize to hypoxia-induced foci and does not colocalize with SGS3. Co-expression of SGS3-CFP (red) and CaM2-YFP (green) following 2 hr of hypoxia. Images are 2D projections of 13 optical sections with a step size of 1 µm. The merged panel adds chloroplast autofluorescence in magenta. Scale bar is 50 µm.

phosphatidyl ethanolamine in the growing phagophore during the biogenesis of the autophagosome (Stolz et al. 2014, Michaeli et al. 2016, Marshall et al. 2018). Once tethered to the phagophore membrane, ATG8 recruits cargo ATG8 proteins have a core ATG8 interacting motif (AIM) consisting of an aromatic amino acid residue, followed by any two residues, then an aliphatic, branched-chain residue, or [F,W,Y] X, X [L,I,V]. This motif is found in all canonical cargo adaptors (Tzfadia et al. 2013, Marshall et al. 2018). CML38, rgsCaM, as well as CML37, which falls in the same clade, all have putative AIM motifs in their N-terminal extensions (Figure 31). CML38 and rgsCaM both have FxxL sites at the same positions in their alignments, and CML39 contains an FxxxL at this position, suggesting it may have had a trinucleotide insertional mutation (Figure 31). The N-terminal domains show lower conservation than the CaM domains. The N-terminal domains of At-CML38 and Nt-rgsCaM are 28.3% similar (Table 2), while the full-length similarity is 57.89% (Figure 5B). It is also notable that S16 of Nt-rgsCaM (marked with a white box in Figure 31) is broadly conserved throughout the Solanaceae family (see Discussion section, Figure 49). The potential role of this site as a target for regulatory phosphorylation will be discussed later. This serine is not conserved throughout the Brassicaceae family, however, since both CML38 and CML39 lack this serine. Notably, CML38, 39 and 37 (all of the Arabidopsis rgsCMLs containing an N-terminal extension) have a serine aligning with S10 of CML38 (white box in Figure 31), which is a *bona fide* phosphorylation site (Wang et al. 2013), based on phosphoproteomics results obtained using the PhosPhAt search engine (Heazlewood et al. 2008, Durek et al. 2010, Zulawski et al. 2013).

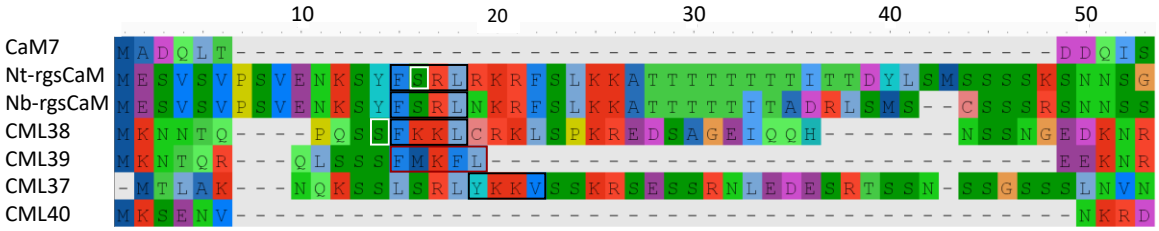

Figure 31 Multiple sequence alignment of N-terminal domains of rgsCaM-like proteins. Amino acid sequences for At-CaM7, Nt-rgsCaM, Nb-rgsCaM, At-CML38, At-CML39, At-CML37 and At-CML40 were aligned using the MUSCLE algorithm. Sequences prior to the E-helix of the first EF hand are shown, colored by amino acid properties. Black boxes indicate the putative ATG-interacting motifs (AIMs), and the red box indicates a possible vestigial AIM domain at the same position in CML39, containing an insertion disrupting the motif. The white box at Nt-rgsCaM S16 is discussed in text as

	CaM7	CML37	CML38	CML39	CML40	Nt-rgsCaM	Nb-rgsCaM
CaM7	-	6.12	11.90	19.05	27.27	5.66	7.84
CML37		-	34.69	10.20	4.08	41.51	46.15
CML38			-	27.91	11.90	28.30	31.37
CML39				-	23.81	11.32	11.76
CML40					-	7.55	7.84
Nt-rgsCaM						-	75.47

Table 2 Sequence similarity for N-terminal domains of rgsCaM-like proteins, with At-CaM7 as a calmodulin reference. Full-length protein sequences were aligned with the MUSCLE algorithm (see Materials and Methods), then sequences were truncated to include only the amino acids prior to the E-helix of the first EF-hand. The alignment was imported into the “Sim and Ident” tool (Bioinformatics.org) to produce percent similarity values.

3.6 rgsCaM colocalizes with autophagosome marker ATG8e and binds this protein through an AIM site

We hypothesize that rgsCaM-like proteins may act as autophagic cargo adaptors for the autophagic degradation of mRNPs (granulophagy) under stress. This hypothesis is based on the fact that rgsCaM caused multiple binding partners to be degraded by autophagy: HC-Pro (Nakahara 2012), AL2 (Yong Chung et al. 2014), SGS3 (Li et al 2017), and RDR6 (the latter by virtue of it being in complex with SGS3) (Li et al 2017). We first tested to see if rgsCaM colocalizes with the autophagosome marker YFP-ATG8e, which decorates the autophagosome membrane. Co-expression of YFP-ATG8e and rgsCaM-CFP indeed showed strong colocalization by 3 hr 45 min of hypoxia (Figure 32), with high Manders' colocalization coefficients ($MCC_{ATG8e:rgsCaM}$ = 0.83 and $MCC_{rgsCaM:ATG8e}$ = 0.84).

Having established colocalization, we investigated this further using ratiometric biomolecular fluorescence complementation (rBiFC) to test for direct interaction or close association, and to probe the putative AIM domain of rgsCaM. Ratiometric BiFC assays (rBiFC) utilized the pBiFC 2-in-1 plasmid system (Grefen et al. 2012) in *N. benthamiana* transfected leaves. BiFC assays test for *in vivo* association of two proteins of interest. Each protein is fused to one half of YFP. If the two proteins of interest interact *in vivo,* or are brought in close proximity, the YFP halves will also be brought together and will reform a stable, functional YFP. Observation of YFP fluorescence is indicative of association of the proteins of interest. The 2-in-1 plasmid system improves on conventional two-plasmid BiFC approaches in three important ways (for an example

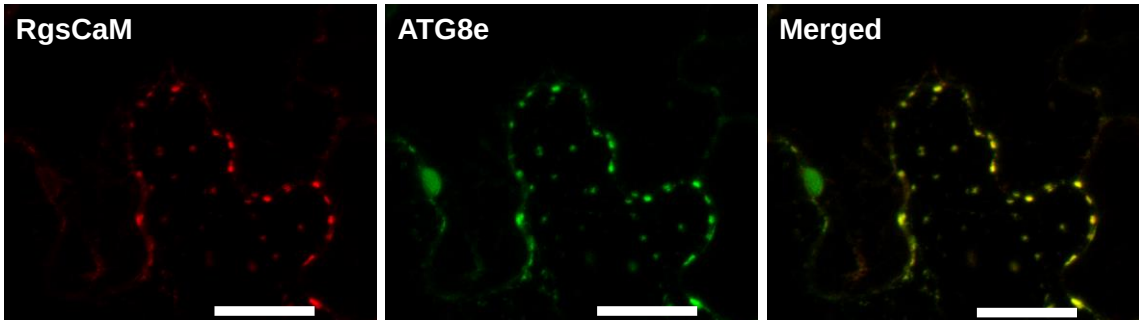

Figure 32 rgsCaM colocalizes with ATG8e under hypoxia. rgsCaM-CFP and YFP-ATG8e were co-expressed in *N. benthamiana*. Images were taken after 3hr 45 min of hypoxia and are shown as 2D projections from 18 optical sections with a 1 µm step size. Scale bars are 30 µm.

plasmid map see Figure 33). First, the 2-in-1 plasmids express both genes-of-interest from a single plasmid, ensuring each transfected cell expresses both genes-of-interest, and with equal copy number. Second, expression of a constitutive mRFP1 fluorescent protein identifies transfected cells even if they show no BiFC signal, providing confidence in negative results and transformation efficiency. Third, the mRFP1 provides a baseline level of fluorescence that allows quantitative comparison BiFC signal intensities of experimental samples against positive and negative controls (Grefen et al. 2012). The system consists of four plasmids, together providing each combination of fluorescent protein fusion position. The map for pBiFC NC 2-in-1 (Figure 33) fuses fluorescent protein fragments at the N-terminus of the first protein of interest and the C-terminus of the second protein of interest. The others are named “NN”, “CN”, and “CC” plasmids (Grefen et al. 2012)

For rBiFC analysis of ATG8e and rgsCaM interaction, a pBiFC NC ATG8e, rgsCaM construct was generated (Figure 34). This fuses the N-terminal portion of YFP (nYFP) at the N-terminus of ATG8e, and the C-terminal portion of YFP (cYFP) at the C-terminus of rgsCaM. ATG8e requires N-terminal fusions since it undergoes C-terminal cleavage as part of its maturation and attachment to phosphatidyl ethanolamine, which is required as part of phagophore generation (Marshall et al. 2018). From prior testing of localization constructs, rgsCaM localization is unaffected by N- or C-terminal fusions, but protein-protein interactions could be affected, so “NC” and “NN” plasmids were both made and tested. The “NC” and “NN” constructs showed the same results, indicating that the fusion position with respect to rgsCaM does not affect interaction with ATG8e by BiFC assay.

Figure 33 Representative vector map for a pBiFC 2-in-1 plasmid, pBiFC NC. Two gateway-compatible recombination cassettes are present. One gene-of-interest replaces the sequence between the *attR3* and *attR2* recombination sites. The *attR3* and *attR2* Gateway cassette contains the *LacZ* reporter gene for blue-white screening, under the control of the *PlacZ* promoter. In pBiFC NC, this site will introduce the protein coding sequence downstream of with the N-terminal fragment of YFP (*nYFP*), producing a fusion protein with nYFP at the N-terminus. The second gene-of-interest replaces the attR1 and attR4 cassette which contains a chloramphenicol resistance gene (*CmR*) and the *ccdB* suicide gene. Recombination at this site will produce a fusion protein with the c-terminal fragment of YFP (cYFP) at the C-terminus of the protein encoded by the second gene-of-interest. *RB* and *LB* indicate the right and left T-DNA borders flanking the sequence which transforms the plant cells. Both recombination sites contain an upstream CaMV *35S* promoter (*35S*), and a downstream *35S terminator* (*T35S*). The plasmid contains a bacterial spectinomycin resistance gene (*SpecR*) for selection. The constitutively expressed *35S:RFP* is also present with a *T35S* terminator. Hemagglutinin (HA) and cMyc epitope tags indicated, and are incorporated as translational fusions to the R3,R2 insert and the R1,R4 insert, respectively.

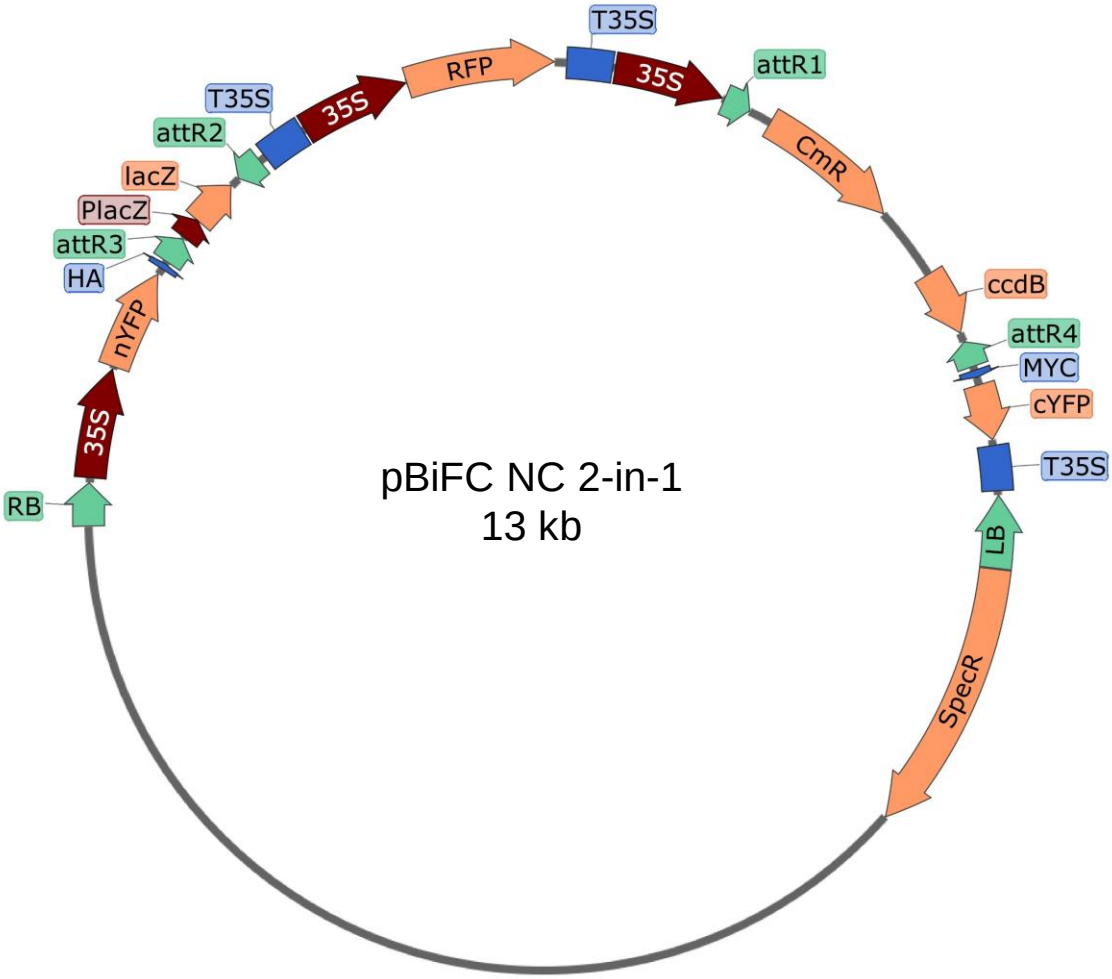
pBiFC NC 2-in-1
13 kb
T35S
35S
attR1
CmR
ccdB
attR4
MYC
cYFP
T35S
LB
SpecR
RB
35S
nYFP
HA
attR3
PlacZ
lacZ
attR2
T35S
35S
RFP

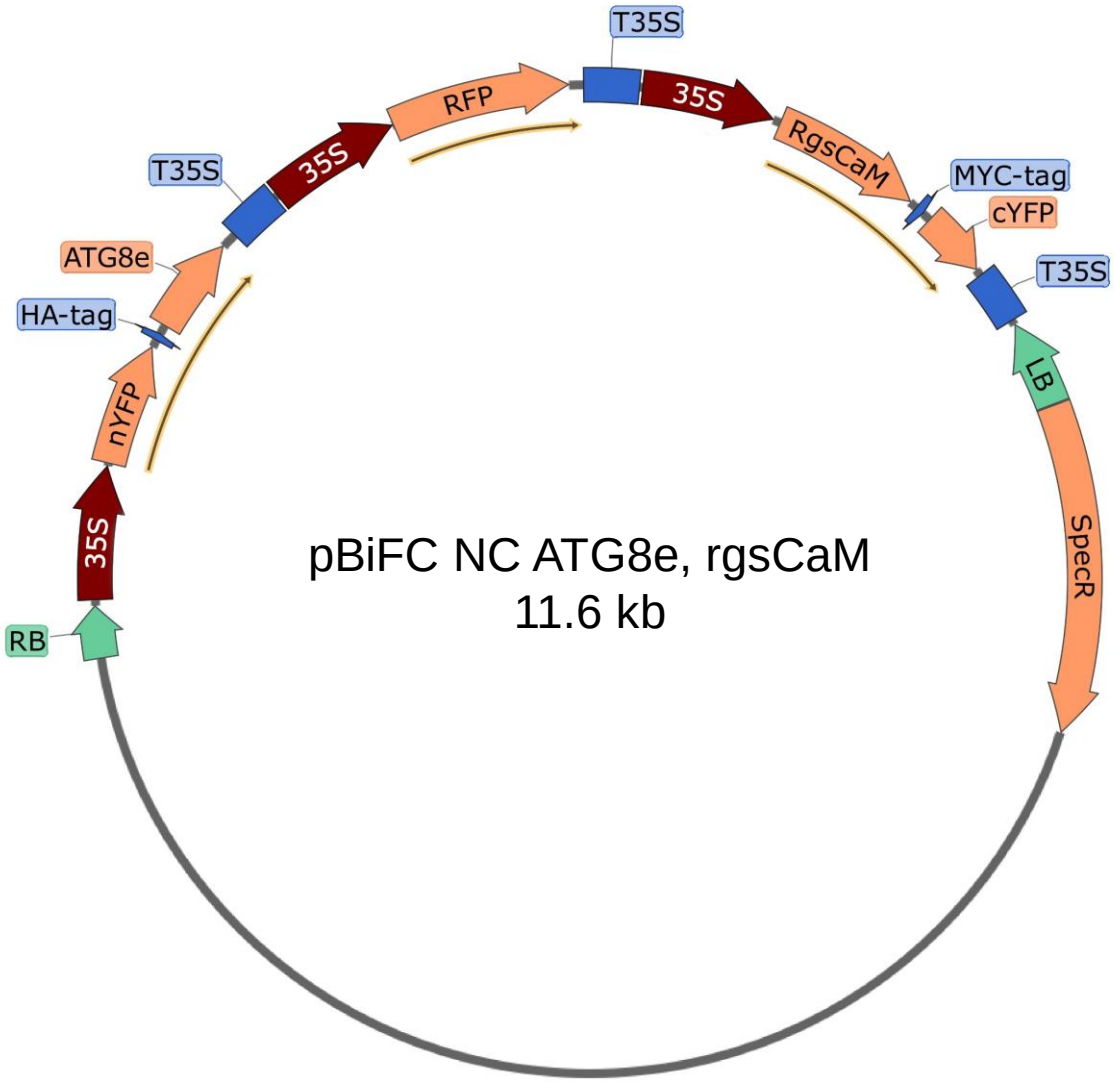

Figure 34 Representative vector map for the BiFC construct "pBiFC NC ATG8e, rgsCaM." This vector map represents the product of a successful multisite Gateway recombination with pBiFC NC and two donor plasmids, pDONR 221 L3,L2 ATG8e and pDONR 221 L1,L4 rgsCaM. The open reading frames for nYFP-HA-ATG8e, the constitutive mRFP1, and rgsCaM-MYC-cYFP are indicated with yellow-outlined black arrows. Other vector features are labeled as in (Figure 33).

To quantify the rBiFC signal, YFP and mRFP1 single optical section imaging was performed using standardized settings across all experimental samples. In ImageJ, individual cells were selected, and total brightness was measured. The ratio of YFP:mRFP1 fluorescence was calculated for each cell, was normalized to the average ratio of the sample with the highest BiFC fluorescence intensity (ATG8e, rgsCaM), and plotted as histograms. Transfection of *N. benthamiana* with pBiFC NC ATG8e, rgsCaM showed a robust BiFC signal (Figure 35) that suggests that the two proteins interact *in planta*. At-CaM2 was used as a negative control. The pairing of wt ATG8e and rgsCaM showed a robust BiFC signal, while ATG8e and CaM2 averaged <10% of this signal strength (Figure 35,Figure 36).

The high expression of two fusion proteins that closely co-localize but do not directly interact can lead to the formation of a stable YFP moiety and a BiFC signal (Kudla et al. 2016). As a result, good positive and negative controls are needed to ensure that an observed BiFC signal is the result of physical interaction of the two protein partners. The ideal negative control would be a site-directed mutant of the test protein that abolishes the interaction. To test the validity of the ATG8e/rgsCaM interaction, several controls and experiments were performed. With respect to specificity for ATG8e, rBiFC analysis also included two site-directed mutants. The ATG8e G118A mutant substitutes the conserved glycine which is required for cleavage and attachment to phosphatidyl ethanolamine, so this tests for the requirement of ATG8e lipidation for interaction. The G118A mutant failed to interact with rgsCaM (Figure 35), showing significantly lower BiFC signal than wt, and was indistinguishable from the CaM2 negative control (Figure 36A). The L52A mutant has a substitution in the ATG8e AIM

motif hydrophobic W binding pocket which prevents ATG8e from binding the aromatic residue of the AIM domain of cargo adaptors. This mutation is a conserved leucine residue that constitutes part of the W hydrophobic site that interacts with the first aromatic residue in the AIM motif with ATG8 and LC3 (the human homolog) proteins (Yamaguchi et al. 2010). Substitution of this leucine in ATG8e resulted in the inability of the protein to form an rBiFC signal when co-expressed with rgsCaM (Figure 35, Figure 36). These results suggest that disruption of the ATG8e W-site AIM binding region reduces the interaction with rgsCaM.

To test whether rgsCaM interacts with ATG8e using the putative AIM domain in its N-terminus, BiFC was assayed for ATG8e and an rgsCaM N-terminal truncation, as well as two rgsCaM site-directed mutants. The rgsCaM N-terminal truncation removes the N-terminal extension (amino acids 1-42), leaving just the calmodulin domain. Loss of the N-terminus prevented ATG8e interaction (Figure 35, Figure 36). To directly address whether the putative AIM sequence is involved in rgsCaM binding, two residues were substituted within this region. Conversion of the aromatic phenylalanine to alanine in the W region of the putative AIM domain (Figure 31) prevents ATG8e interaction (Figure 35, Figure 36). The rgsCaM S16A mutation substitutes a serine which is the first of the two non-conserved residues within the AIM motif, immediately downstream of the conserved phenylalanine (Figure 31). Mutation of serine 16 also caused a loss in ATG8e binding (Figure 35, Figure 36). These results indicate that the rgsCaM N-terminus is required for ATG8e interaction, and more specifically, disruption of the AIM motif, also prevent interaction. Taken together, the data suggests that the amino-

Figure 35 Bimolecular fluorescence complementation of wt and mutant or truncated forms of rgsCaM and ATG8e. Representative confocal images of single optical sections for rBiFC experiments. Positive BiFC signals are shown in green, while the constitutive mRFP1 for normalization is shown in red. AtCaM2 was used as a negative control for interaction with ATG8. G118A and L52A are ATG8 mutants, while F15A and S16A are rgsCaM mutants. The ΔN-rgsCaM excludes amino acids 1-42 from rgsCaM. Scale bars are 50 µm.

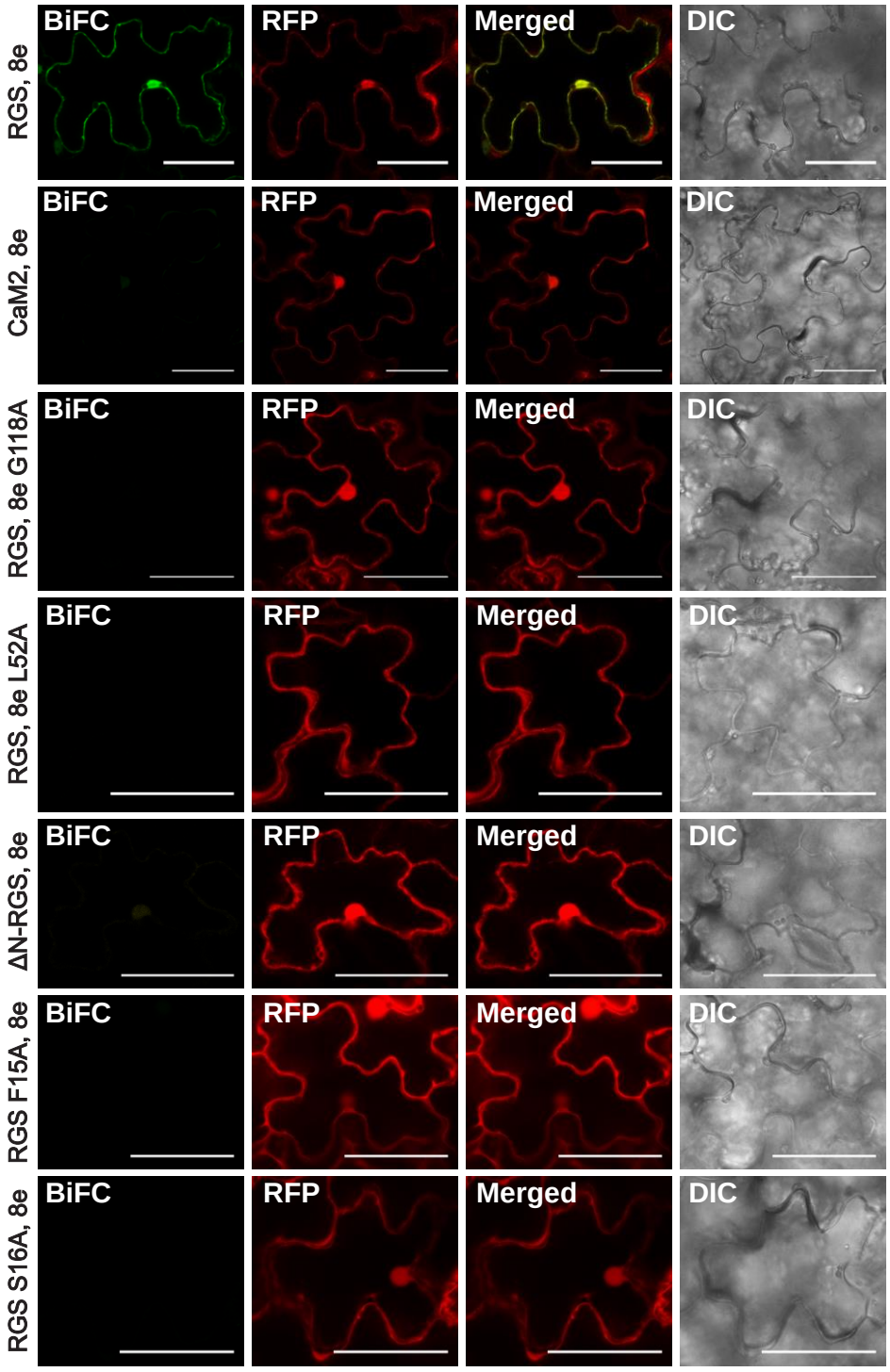
RGS, 8e
CaM2, 8e
RGS, 8e G118A
RGS, 8e L52A
ΔN-RGS, 8e
RGS F15A, 8e
RGS S16A, 8e
BiFC
RFP
Merged
DIC

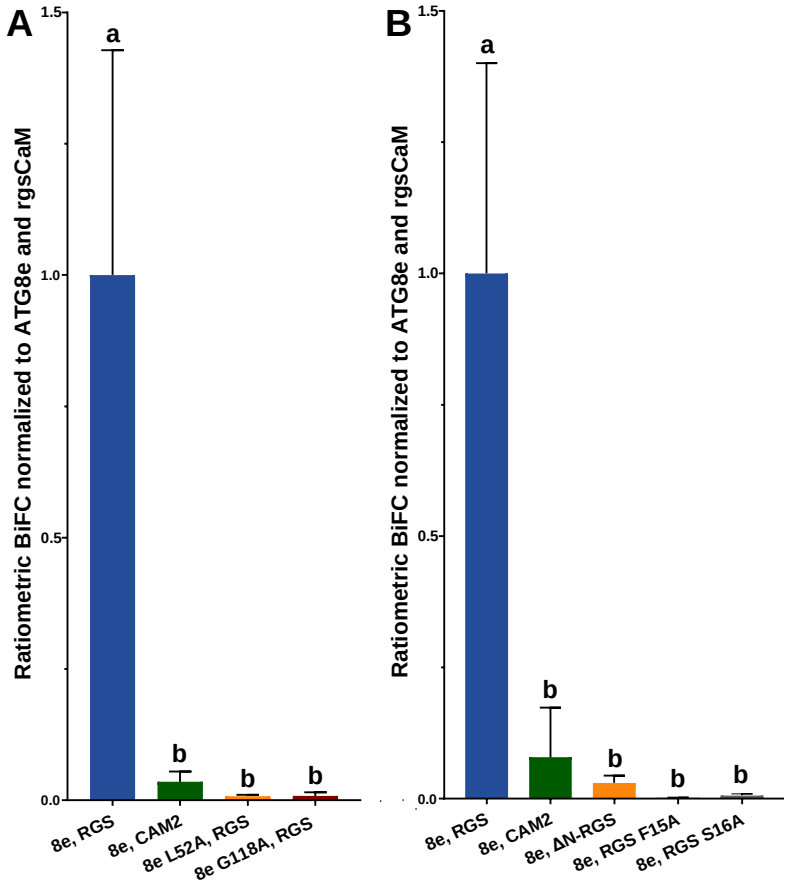

Figure 36 Quantification of rBiFC signals for wt and mutant forms of both rgsCaM and ATG8e. Ratios for cytosolic BiFC to constitutive RFP1 signals were determined for 20 cells across four biological replicates. Values were normalized to the highest ratio, which was rgsCaM with ATG8e. Error bars are standard deviation. **A)** By one-way ANOVA with multiple comparisons, the BiFC signal ratio for rgsCaM paired with ATG8e (a) is significantly higher than when rgsCaM is paired with the negative control AtCaM2 or either ATG8e mutant (b), with p values <0.0001. The samples labeled "b" are not significantly different from each other. **B)** BiFC quantification as in A, but testing ATG8e with the N-terminal truncation of rgsCaM (ΔN-RGS), or the F15A or S16A rgsCaM mutants.

terminus of rgsCaM contains a *bona fide* AIM domain that is characteristic of selective autophagy cargo receptors and which is necessary for binding to ATG8e.

3.7 Mutation of the putative ATG-interacting motif does not prevent rgsCaM granulation or colocalization to foci with ATG8e

Since rgsCaM F15A lost ATG8e interaction by BiFC, we wanted to know if this also prevented their colocalization. The F15A mutation was introduced into the CFP-localization plasmid, pEarleyGate 102. In this experiment, wt rgsCaM and F15A rgsCaM were co-expressed in *N. benthamiana.* Both the wt and mutant proteins co-localized to hypoxia-induced cytosolic foci (Figure 37). This colocalization was also conducted with the addition of a labeled ATG8e (Figure 38). This result also showed no difference between wt and F15A with respect to colocalization with ATG8e foci.

3.8 rgsCaM and ATG8e colocalize at the periphery of mRNP granules in late hypoxia

The evidence that rgsCaM interacts with ATG8e and that rgsCaM-containing bodies traffic to and from stable associations at the surface of mRNPs under hypoxia stress support the model that rgsCaM acts as an autophagic cargo adaptor for mRNP recycling under stress. To further test this model, we used high resolution imaging methods to investigate the spatial distribution of ATG8e and rgsCaM in relation to each other at the surface of an mRNP. Imaging was performed at high magnification and with detector settings to capture pixel data at the limit of the resolving power of the instrument (as determined by the LAS X software). To better resolve the differences between peripheral and internal mRNP localization, we investigated ATG8e and rgsCaM

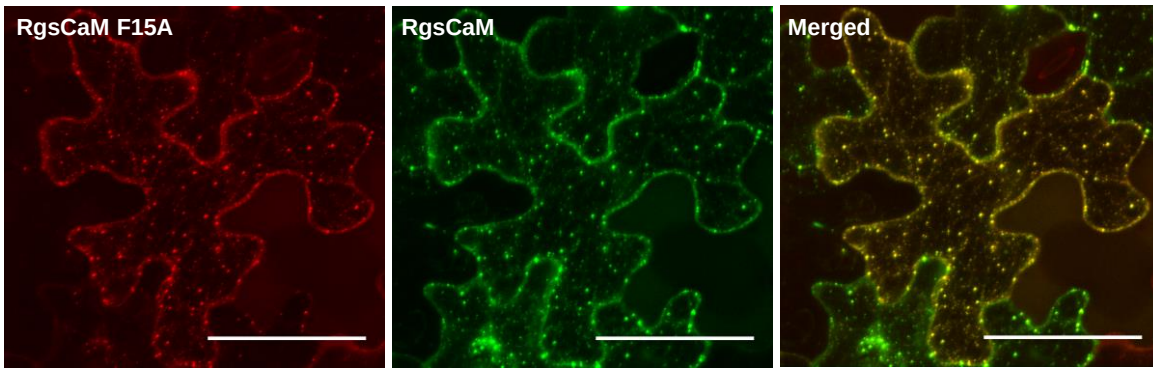

Figure 37 Mutation of rgsCaM putative AIM motif does not prevent granulation. rgsCaM F15A-CFP and rgsCaM-YFP were imaged following 3.5 hr hypoxia in transfected *N. benthamiana* leaves. Images were subjected to standard deconvolution and are 2D projections from 14 optical sections with a step size of 2 µm. Scale bars are 50 µm.

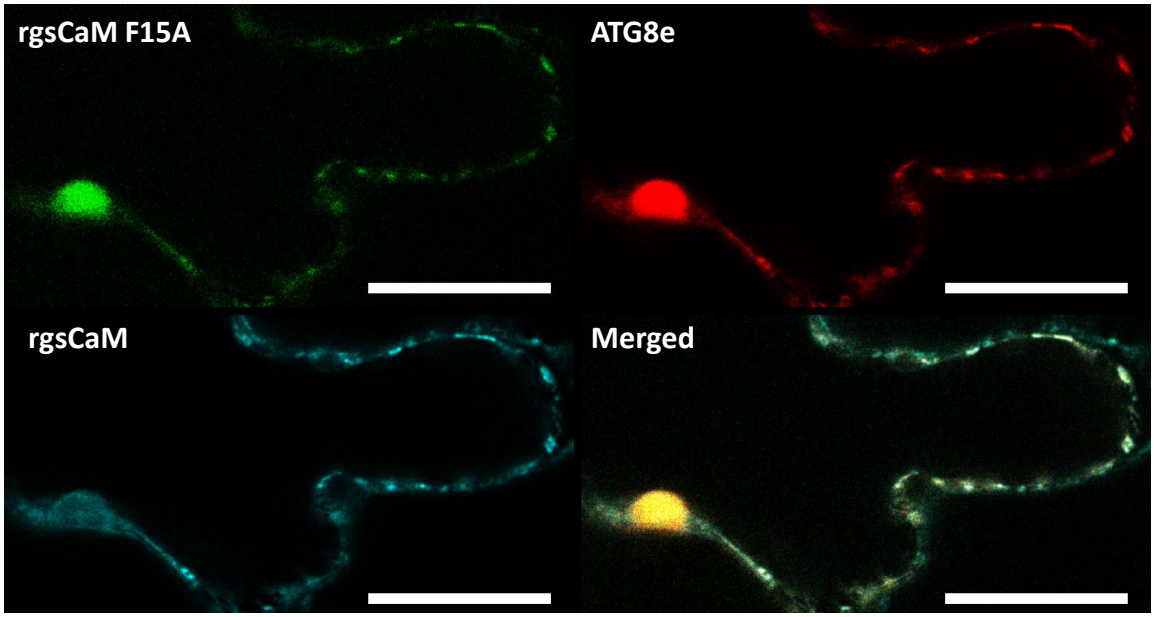

Figure 38 rgsCaM AIM domain mutation does not prevent ATG8e colocalization. rgsCaM F15A-CFP, YFP-ATG8e and rgsCaM-RFP were expressed in *N. benthamiana* and images after 4 hr of hypoxia. Images are from a single optical section. Scale bars are 20 µm.

localization with respect to processing bodies. PBs continue to increase in size during a sustained stress (Kedersha et al. 2005), so they become larger than single SGs under hypoxia. We imaged DCP1-CFP processing bodies at 5 hr of hypoxia, with co-expression of YFP-ATG8e and rgsCaM-mScarlet. The representative PB in Figure 39 A-B is 2-2.5 µm in diameter, and both rgsCaM and ATG8e showed enhanced localization to the PB periphery (Figure 39 A-B), which extends slightly beyond the DCP1-CFP signal (Figure 39 B).

3.9 The rgsCaM S16A mutant shows greater nuclear localization than wt

The subcellular localization of rgsCaM S16A relative to the wild type rgsCaM was investigated by co-expression analysis in *N. benthamiana*. S16A showed co-localization to hypoxia-induced cytosolic granules similar to wt rgsCaM, but showed a noticeable difference in nuclear localization (Figure 40). Nuclear localization was quantified by measuring the total fluorescence of the nucleus and the total non-nuclear fluorescence of each cell using ImageJ, based on single optical sections which passed through the nucleus. The results are shown in Figure 40C. S16A had an average of 21% greater nuclear signal than wt rgsCaM. A time series was also taken for the cell in Figure 40A, and the nuclear to non-nuclear ratios for wt and S16A did not change with the transition from non-granulated to granulated (ranging from 10 min to 2 hr of hypoxia. While the reason for the difference between wt and S16A rgsCaM localization is not clear, it does suggest that the amino terminal domain may function as a potential determinant in cytosolic/nuclear localization. Since the amino terminal domain of rgsCaM-like CMLs

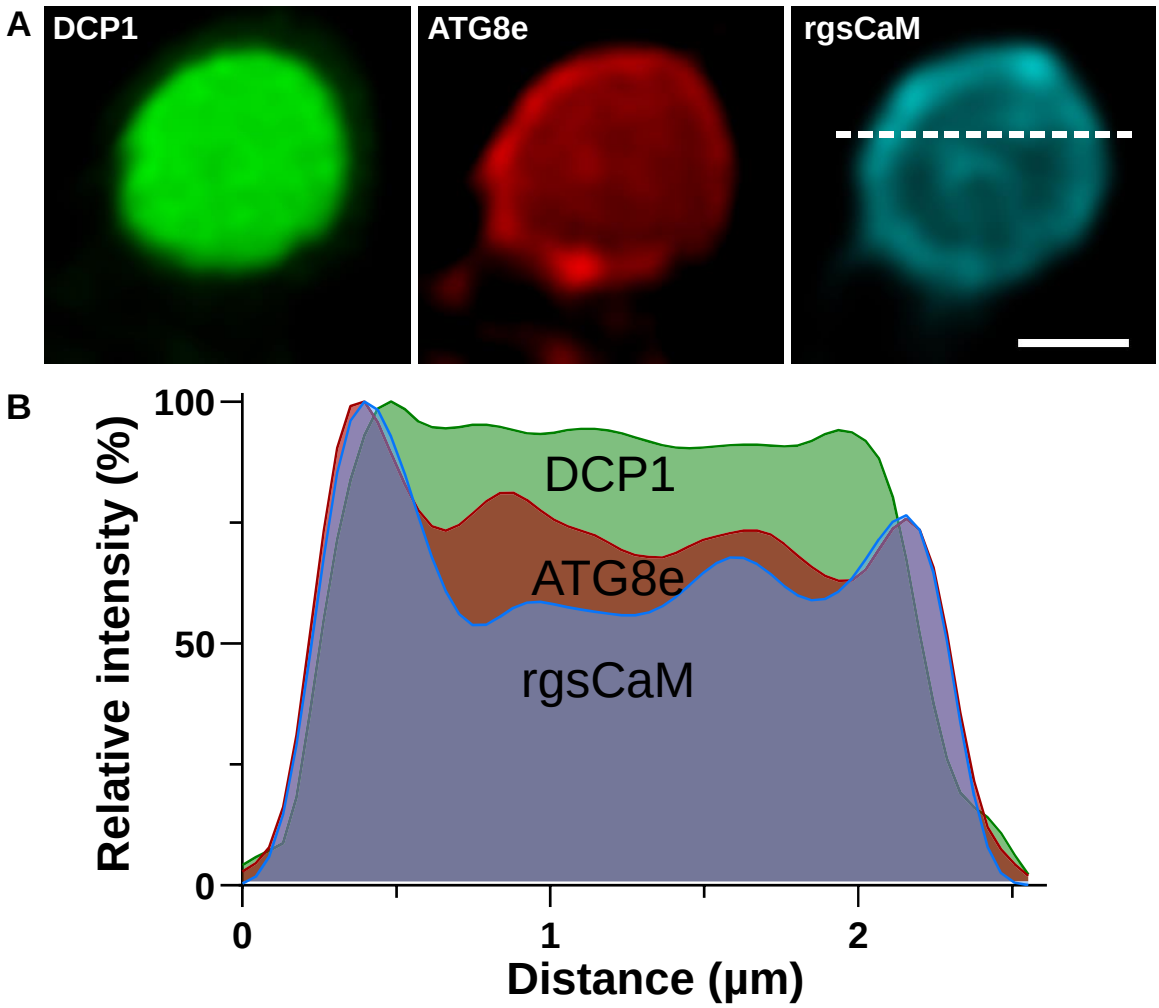

Figure 39 rgsCaM and ATG8e localization to the periphery of DCP1 and SGS3 bodies. **A)** Colocalization of DCP1-CFP, YFP-ATG8e and rgsCaM-mScarlet in *N. benthamiana*. Images are a 2D projection of 9 optical sections with a Z-step size of 0.2 μm, taken at 5 hr of hypoxia. The scale bar is 1 μm. These images were generated using the Lightning deconvolution system. The smooth rendering filter was applied in LAS X. **B)** Line plot through the dashed line in A generated from the unfiltered data.

contain sites for phosphorylation, the possibility that S16 is a regulatory phosphorylation site merits further investigation (see Discussion).

3.10 rgsCaM interacts with TuMV HC-Pro by BiFC and FRET

To validate our BiFC approach we tested for association of Nt-rgsCaM with TuMV HC-Pro. Nt-rgsCaM interaction with TuMV HC-Pro was previously demonstrated by SPR (Nakahara et al. 2012) and with TEV HC-Pro by yeast-two-hybrid (Anandalakshmi et al. 2000). TuMV HC-Pro and rgsCaM were cloned into pBiFC NC as previously described for other BiFC constructs. When introduced in to *N. benthamiana* by agroinfiltration, a robust BiFC signal was seen Figure 41. The HC-Pro and rgsCaM BiFC complex is largely excluded from the nucleus, and from cytosolic granules as compared to rgsCaM alone by 3 hr of hypoxia (compare to rgsCaM time series in Figure 14).

While the interactions of rgsCaM and HC-Pro homologs have been studied by BiFC (Lokdarshi 2015), SPR (Nakahara et al. 2012) and yeast two hybrid (Anandalakshmi et al. 2000), understanding the calcium-dependence of the HC-Pro interaction, interactions between rgsCaM and other binding partners, as well as the effect calcium has on the subcellular localization of these proteins, would be better studied by FRET. We developed clones for this purpose using the pFRET 2-in-one system (Grefen). pFRET TV CN was used to express rgsCaM fused to a c-terminal mTurquoise2, and TuMV HC-pro fused to an N-terminal venus. When co-expressed both, proteins range from no or few granules to abundant partially colocalizing cytosolic

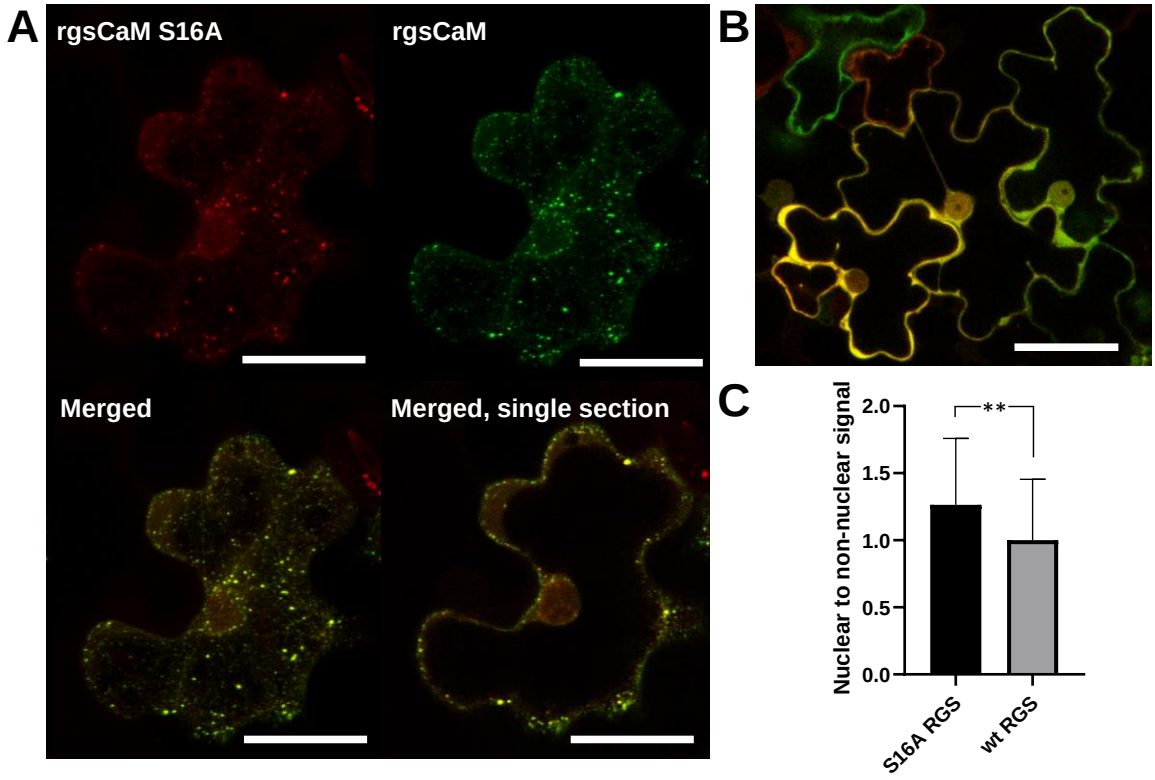

Figure 40 rgsCaM S16A shows greater nuclear localization than wt rgsCaM. (A) Representative S16A rgsCaM-CFP and wt rgsCaM-YFP co-expressing cell at 1 hr 40 min showing colocalization at cytosolic nuclei and relative nuclear localization. Images are 2D projections of 26 optical sections with a Z-step size of 1 µm. Scale bars are 30 µm. **(B)** representative cells with a single optical section through the nuclei at 1 hr hypoxia used for calculation of nuclear to non-nuclear fluorescence signals. Scale bar is 50 µm. **(C)** Nuclear to non-nuclear fluorescence signal ratios for S16A rgsCaM and wt rgsCaM. The samples are statistically significantly different based on a student t-test of paired values, with $p = 0.0056$, $n = 5$.

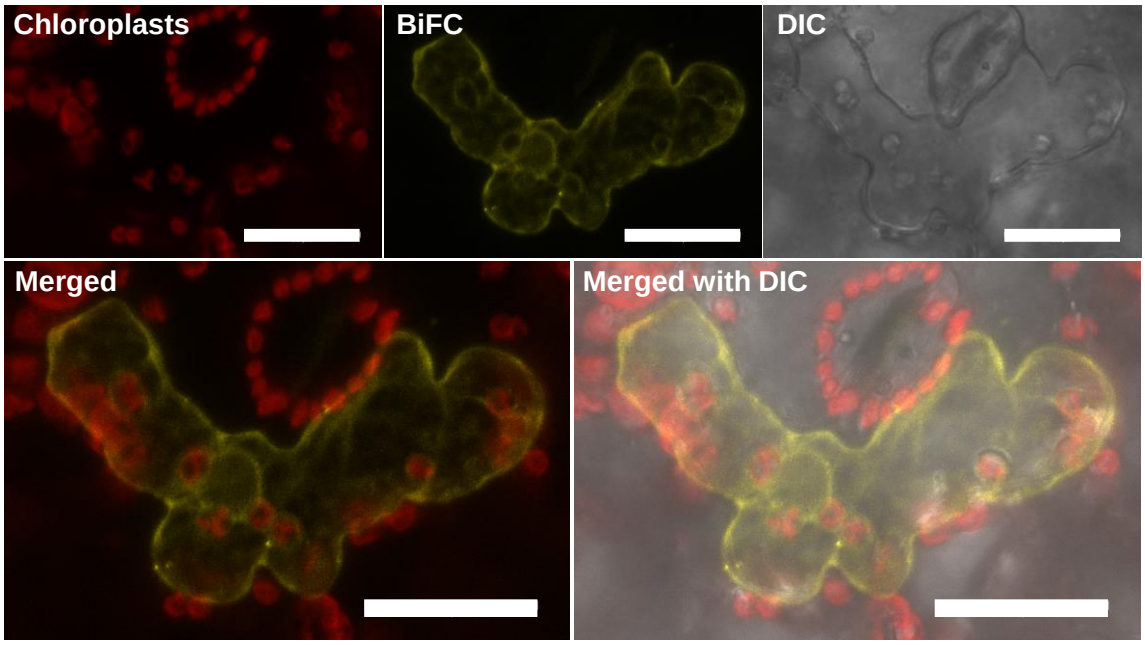

Figure 41 *In vivo* interaction of RgsCaM and TuMV HC-Pro by bimolecular fluorescence complementation. *N. benthamiana* leaves were infiltrated with the pBiFCt NC plasmid carrying YN-HC-Pro and RgsCaM-YC transgenes. Imaging is after 3 hr of hypoxia under the coverslip. Images are 2D max intensity projections from 7 optical sections with a step size of 2.6 µm.

granules as seen in Figure 42. Although this was not specifically tested, rgsCaM also appears to have a more pronounced nuclear localization when co-expressed with HC-Pro as compared to rgsCaM alone (see Figure 14), although nuclear exclusion was seen for HC-Pro and rgsCaM BiFC complexes (Figure 41).

Förster resonance energy transfer (FRET) is used as a technique for measuring the distance between two different fluorophores (Hecker et al. 2015). In biology, fluorescent proteins are often fused to proteins of interest and the degree of FRET is used as a proxy for assessing the physical interactions of those proteins *in vivo.* This can either be done in steady state conditions or in response to a stimulus. In FRET, two fluorescent proteins with spectral overlap are used, one acts as the donor and the other as the acceptor. The microscope excites the donor at its excitation wavelength. Normally the fluorescent protein would then emit a photon at its emission wavelength. However, if a nearby fluorescent protein happens to be excited at the wavelength that the donor would emit its photon, the energy can transfer directly to this acceptor protein without emitting a photon. The acceptor protein is then excited, and will emit a photon at its emission wavelength, which will necessarily be longer than that of the donor. FRET efficiency decays rapidly with increased distance, following an inverse sixth power function (Hecker et al. 2015). FRET is effective at detecting proximities of less than 10 nm, which is typical of complexed proteins (Hecker et al. 2015).

Acceptor photobleaching FRET (AB FRET) is one manner of measuring FRET (Hecker et al. 2015). In AB FRET, a preliminary fluorescence image is captured for the donor, and separately for the acceptor, each using their specific excitation wavelengths.

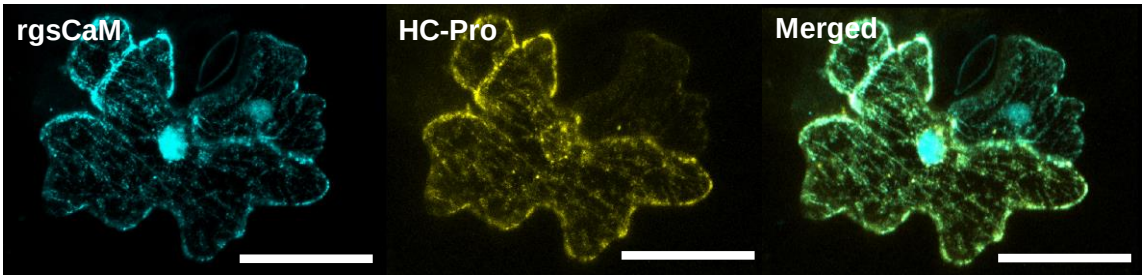

Figure 42 rgsCaM and HC-Pro partially co-localize to cytosolic foci under hypoxia. pFRET TV CN carrying rgsCaM and HC-Pro inserts was transfected into *N. benthamiana* leaves. Images are taken after 1 hr 20 min of hypoxia and are shown as 2D projections of a Z-series. Scale bars are 30 µm.

Next, a specified region within the microscope field of view is photobleached for the FRET acceptor protein. This is performed using high laser intensity at the excitation wavelength of the acceptor for several seconds. Once bleached, a fluorescent protein can no longer accept excitation energy from photons or by resonance energy transfer. This is verified by capturing a new image of the acceptor fluorescence. Then, the donor protein is excited at its fluorescence emission is captured. If two fusion proteins were interacting, or in a comparable close physical proximity, then in the original image some of the excitation energy of the donor would have been transferred to the acceptor rather than being emitted as a photon at the emission wavelength of the donor. However, after acceptor photobleaching, this energy transfer cannot occur, so that energy will instead be emitted as photons. Effectively, the emission of the donor protein will become brighter after photobleaching, in an amount a dependent on the FRET distance between fluorophores (Hecker et al. 2015).

Acceptor photobleaching FRET (AB FRET) was successful in detecting the *in-vivo* association of Nt-rgsCaM and TuMV HC-Pro (Figure 43). The FRET signal within the area of acceptor photobleaching shows greater FRET signal than the background in unbleached areas (Figure 43E). The maximum FRET efficiency in this area is 0.72, with much of the signal being around 0.3, which appear as red and green on the heat map, respectively (Figure 43). A FRET efficiency of 0.72 corresponds to a fluorophore distance of 4.96 nm, and 0.3 corresponds to 6.68 nm (see materials and methods). For reference, GFP is 4.2 nm in length, and 2.4 nm wide (Hink et al. 2000). The proof of concept performed here demonstrates that this tool should be useful in future

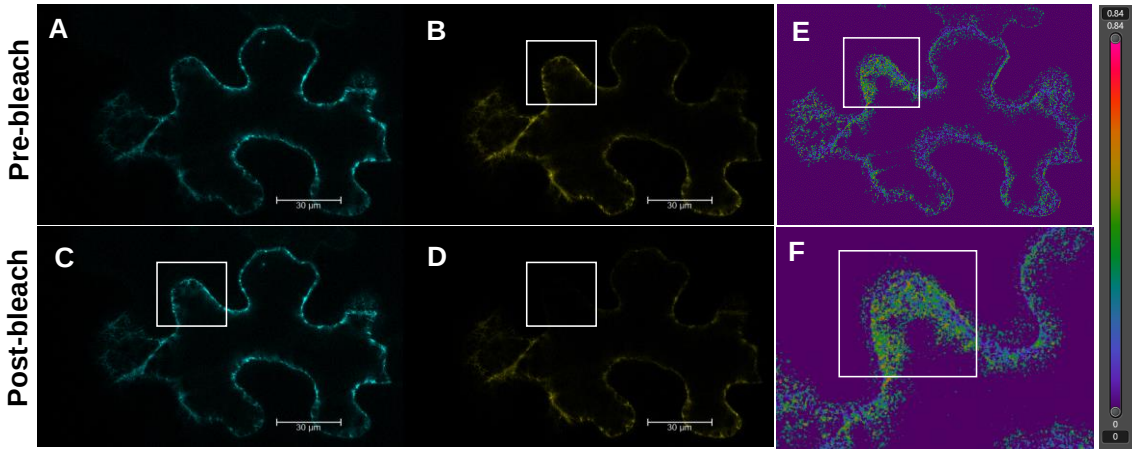

Figure 43 Acceptor photobleaching FRET for rgsCaM-mTRQ2 and Venus-HC-Pro. rgsCaM-mTRQ2 (**A**) and Venus-HC-Pro (**B**) were imaged before acceptor photobleaching, and after photobleaching (**C**, **D** respectively). The photobleached area is indicated in the white boxes, and the result of bleaching can be seen in **D**. FRET efficiency is shown in a heat map in **E**, and magnified in **F**. The heatmap scale is shown at right. FRET efficiencies in the indicated area range from around 0.3 (green) to a maximum of 0.72 (red).

experiments to examine the calcium-dependence of the *in-vivo* associations of HC-Pro and rgsCaM. AB FRET as shown here can be used to investigate FRET under different steady-state conditions, but real-time observations of interaction dynamics can also be done using this tool with sensitized emission FRET (Hecker et al. 2015).

3.11 Loss of CML38 delays systemic Turnip mosaic virus infection in Arabidopsis

Since rgsCaM is an endogenous suppressor of gene silencing, one would expect that if it were constitutively expressed viruses would infect and spread more easily. There are some reports which support this. For instance, the Geminivirus Tomato golden mosaic virus showed enhanced infectivity with constitutive expression of CML39 in Arabidopsis (Yong Chung et al. 2014). The same was shown for Nb-rgsCaM and the Geminivirus Tomato yellow leaf curl China virus and the Bromovirus Cucumber mosaic virus (Li et al. 2014). In contrast, overexpression of Nt-rgsCaM was reported to decrease infectivity of Cucumber mosaic virus, based on viral protein accumulation at up to 4 days post-inoculation (Nakahara et al. 2012). Thus, while most reports suggest that constitutive expression of an rgsCaM will increase infectivity, this has not been not universal.

We tested Arabidopsis lines with constitutive expression of At-CML38 (35S:CML38-YFP from (Lokdarshi et al. 2016)), a cml38ko T-DNA insertion line (Salk_066538C), and wt plants for their rates of systemic infection with the potyvirus Turnip mosaic virus. Rosette leaves were inoculated by agroinfiltration with bacteria containing an infectious clone of TuMV strain UK1 which expresses free GFP (Lellis et

al. 2002). GFP fluorescence was used as a proxy for infection progress, and the first day at which each plant showed GFP in an uninoculated leaf was recorded as the time of systemic infection (see Materials and Methods). Surprisingly, the *35S::CML38-YFP* constitutive expression line (CML38 OX) showed a significant delay in viral infection (2 ± 0.5 days). The cml38ko line showed the same infectivity as wt plants (Figure 44). This result suggests a more complex role for CML38 than just an endogenous suppressor of silencing. CML38 delay of TuMV infection could suggest that CML38 induces TuMV components for degradation through autophagy (see Discussion).

3.12 Development of a novel fluorescent hypoxia biosensor based on oxygen-dependent N-degron-mediated proteolysis

During course of this work, the induction of hypoxia is used as a mechanism for the initiation of granule formation for live cell imaging. One issue with this approach, and with any approach for measuring the oxygen status of cells from an organismal context, is the inability to assess the oxygen concentration in a non-invasive manner. In this section of my thesis, a separate project on the design and engineering of a gain-of-function oxygen sensor based on the N-degron system is described.

The use and development of genetically-encoded biosensors in plants has grown dramatically in recent years (see recent reviews (Gjetting et al. 2013, Hilleary et al. 2018, Walia et al. 2018), with applications in both basic research and agricultural monitoring. We developed a genetically-encoded fluorescent biosensor which can quantitatively report on the hypoxia status of individual cells.

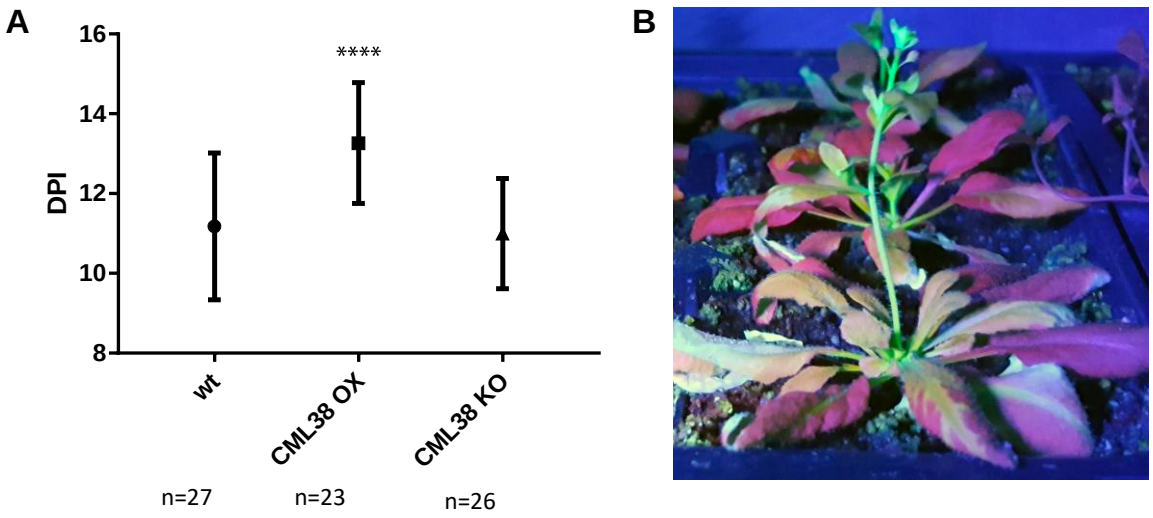

Figure 44 Constitutive expression of the rgsCaM-like protein CML38 in Arabidopsis delays TuMV systemic infection. TuMV-GFP expression was initiated by agroinfiltration of two rosette leaves with agrobacterium (GV3101) carrying the pCB TuMV-GFP plasmid. (A) The average number of days post-inoculation (DPI) at which GFP was observed in a tissue other than the inoculated rosette leaves (systemic infection) is displayed for wt, CML38 OX (*35S:CML38-YFP*), and cml38 ko lines. Day 0 was defined as 24 hr after agroinfiltration to account for the time needed for transfection. The number of plants in the experiment which became infected after 15 dpi (n) is displayed for each line. Error bars are standard deviations. T-test analysis comparing either wt or cml38ko to the CML38 OX line yielded P values <0.0001. wt and cml38ko were not significantly different from one another. (B) A representative plant showing systemic infection with TuMV-GFP under 395 nm UV light.

This hypoxia sensor takes advantage of the oxygen-dependent, N-degron-mediated proteolysis of the *Arabidopsis thaliana* group seven ethylene-responsive transcription factor (ERF-VII) RAP2.12 (Weits et al. 2014). In support of its role in activating the transcription of hypoxia-induced genes, the constitutively expressed RAP2.12 transcription factor is rapidly degraded under normoxia, yet accumulates under hypoxia. The N-terminus of RAP2.12 contains a cysteine immediately following the initial methionine. According to the N-end rule, cysteine is a highly stabilizing amino acid (Weits et al. 2014). However, the N-degron of RAP2.12 is subject to an oxygen-dependent oxidation by plant cysteine oxidases (PCO1 and PCO2). When O_2 is available, PCOs convert cysteine to cysteine sulphinic acid (CSA). CSA is subsequently targeted by ariginyl transferases (ATE1 and ATE2), resulting in the addition of an N-terminal arginine, which is highly destabilizing (Weits et al. 2014). Because of this two-step process, cysteine is also referred to as a tertiary destabilizing residue (Weits et al. 2014). The first 28 amino acids of RAP2.12 was previously demonstrated to be sufficient for the oxygen-dependent degradation (Weits et al. 2014), so we have placed this at the N-terminus of our fluorescent reporter.

For detection, our reporter contains three copies of the venus fluorescent protein along with the SV40 nuclear localization signal. A similar approach was used to generate a boric acid biosensor (Fukuda et al. 2018). Confining the fluorescence signal to the nucleus will facilitate easy fluorescence quantification for individual cells, without time-consuming selection at cell boundaries. The approximately circular nature of nuclei also lends itself to automatic detection by analysis software. Since PCOs are localized

to both the nucleus and cytosol, so this mechanism will function both before and after the reporter localizes to the nucleus (Weits et al. 2014).

The hypoxia sensor was tested in *N. benthamiana.* A plant expression vector was generated which expresses the hypoxia sensor under the control of the constitutive Cauliflower mosaic virus (CaMV) 35S promoter (pEarleyGate 100 *35S::RAP2.12*$_{1\text{-}28}$*-NLS-3xVenus;* see materials and methods). Agrobacteria containing the sensor construct were infiltrated into *N. benthamiana* leaves. Two leaf discs were prepared. The sample in Figure 45A was prepared in 10mM Tris pH 7, while the sample in Figure 45B was also supplemented with 8 units mL^{-1} of EC-Oxyrase reagent (Oxyrase, Inc.). EC-Oxyrase is a commercial enzymatic reagent which scavenges dissolved oxygen and converts it to water (Oxyrase, Inc.). The two samples were imaged with the same microscope settings within 10 minutes of each other. In the absence of Oxyrase, there was no discernable fluorescence from the hypoxia sensor (Figure 45A). In contrast, the sample treated with the hypoxia-inducing reagent showed a nuclear-localized florescence signal (Figure 45B). These results indicated that the oxygen-dependent degradation of the sensor was performing as expected in tobacco.

Quantifying a dynamic fluorescence signal without a stable reference is problematic. While this would be reasonable when comparing cells within the same experiment and within the same tissue, transgene expression may differ by cell- type. Further, excitation and emission light would suffer from penetration differences depending on how deep the tissue is. To overcome these limitations, we incorporated a

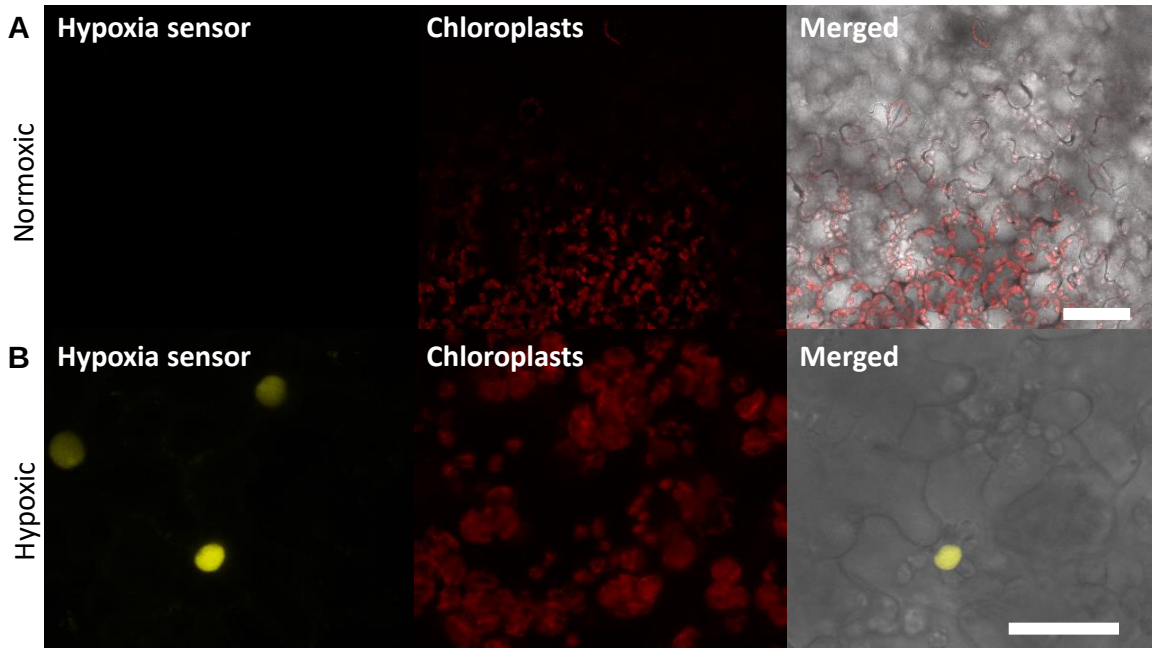

Figure 45 Hypoxia sensor validation in *N. benthamiana*. (A) Fluorescence signal from the YFP channel for the hypoxia sensor along with chloroplast autofluorescence and these signals merged with DIC in the absence of treatment with the commercial enzymatic oxygen scavenging reagent EC-Oxyrayse (Oxyrase, Inc.) Scale bar is 50 µm. **(B)** As in A, except with 8 units mL^{-1} EC-Oxyrase to accelerate hypoxia. Scale bar is 30 µm.

second open reading frame into the hypoxia sensor, which constitutively expresses a nuclear-localized mScarlet fluorescent protein (*35S::NLS-mScarlet*). Under normoxia, the hypoxia sensor is expressed under the *35S* promoter, but is degraded. In contrast, the mScarlet will not undergo oxygen-dependent degradation. This allows quantification of a cell's hypoxia by computing the fluorescence ratio of nuclear venus to nuclear mScarlet. This construct was called pHypox 2 (for map see Figure 46).

pHypox 2 was transfected and tested in *N. benthamiana*, and successfully expressed the sensor and the constitutive mScarlet reporter (Figure 47). Additionally, the reporter showed a hypoxia-induced expression following 2 hr of hypoxia. Both fluorescent proteins showed the expected nuclear localization (Figure 47). The results demonstrate the feasibility of using the N-degron approach to generate a hypoxia sensor. The next step is to incorporate the sensor genetic module into stable transgenic plants to evaluate its suitability at the organismal level.

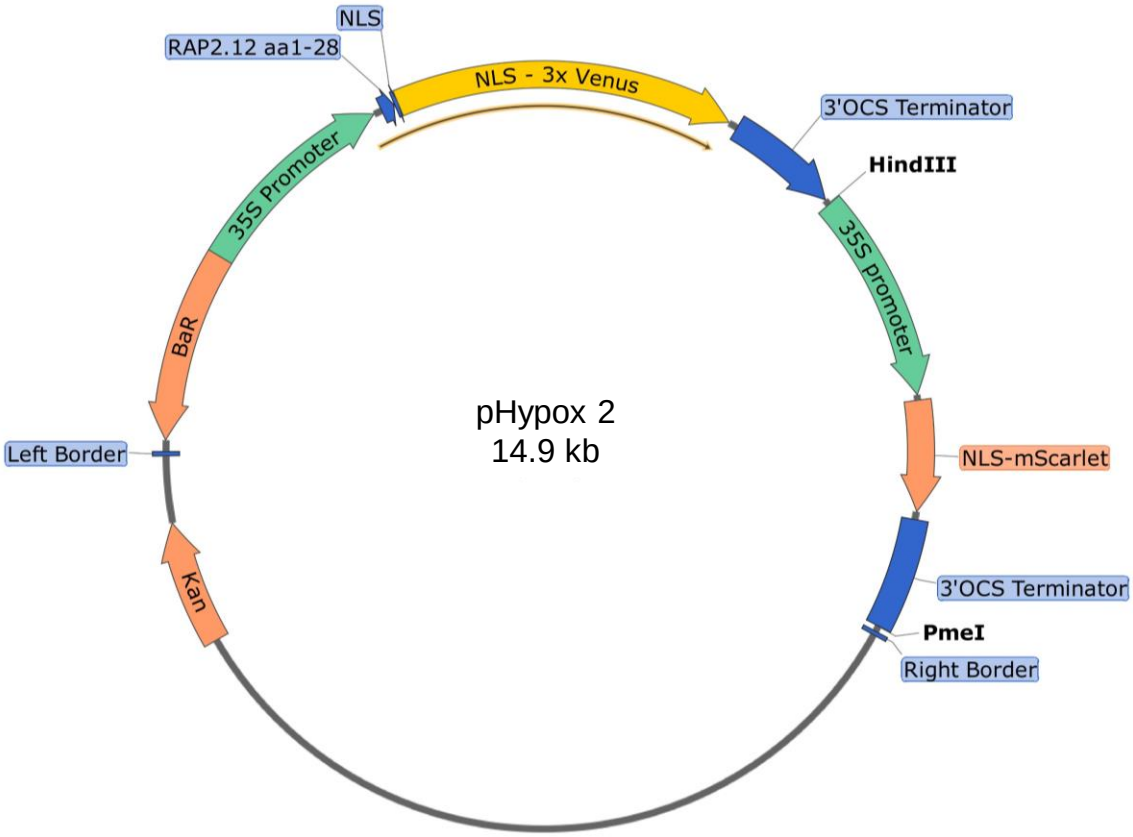

Figure 46 Plasmid map of pHypox 2 for *in vivo* ratiometric hypoxia quantification. Plasmid product following recombination of pDONR/Zeo Hypoxia sensor with pEarleyGate 100, and subsequent insertion of a *35S::NLS-mScarlet* construct between the *HindIII* and *PmeI* sites. The left and right T-DNA borders flank the sequence which transforms plant cells. "*Kan*" is the bacterial selectivity gene for kanamycin resistance. "*Bar*" is the plant selectivity resistance gene to the glufosinate herbicide. The *35S* promoters and 3' *OCS* (octopine synthase) transcriptional terminators flank the sensor and the constitutive *NLS-mScarlet*. The translational fusion for the hypoxia sensor is indicated with the yellow-outlined arrow.

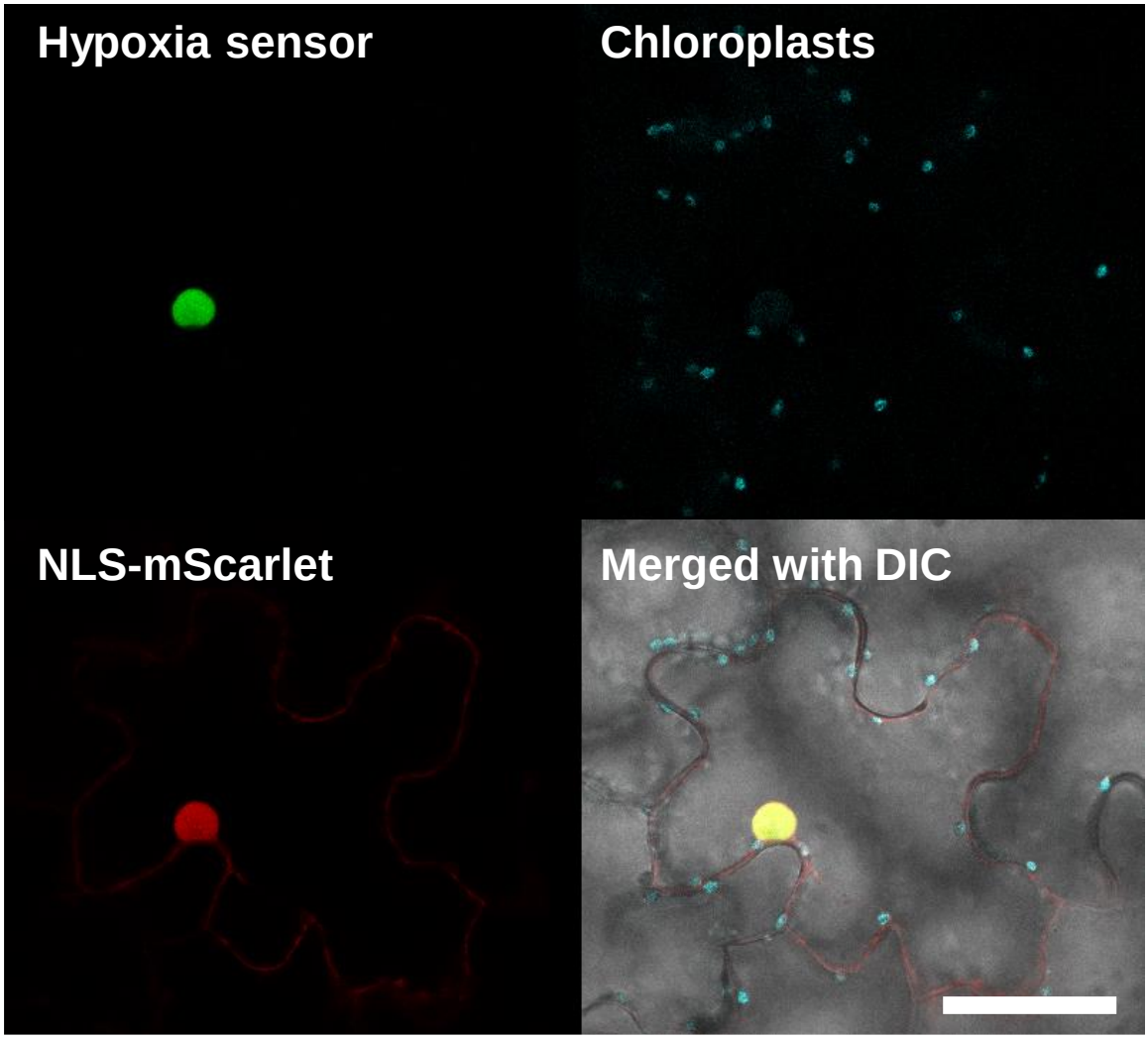

Figure 47 Expression of pHypox 2 in *N. benthamiana*. Representative transfected leaf cell 2 hr after wet-mounting the leaf disc under a coverslip (hypoxia). The hypoxia sensor is shown in green, the nuclear-localized mScarlet is shown in red, the chloroplast autofluorescence is shown in cyan, and these channels merged with DIC is also shown. The scale bar is 50 µm.

Chapter 5: Discussion

4.1 rgsCaM and CML38 are homologous, stress-induced, mRNP localizing proteins

Calcium signaling and calcium-sensing proteins are critical components of the responses to plant abiotic stress, including flooding/hypoxia (Sedbrook et al. 1996, Lokdarshi et al. 2016), salt (Choi et al. 2016), heavy metals and drought (Virdi et al. 2015). Plants have substantially diversified the family of calmodulins and EF hand-containing calcium sensors, with Arabidopsis having seven CaMs and 50 CMLs (McCormack et al. 2003). These CMLs are divergent from conventional calmodulins, and are structurally diverse, having from one to six Ca^{2+}-binding EF-hand domains, and some with additional domains (McCormack et al. 2003). The importance of this diversification in environmental stress adaptation is evident from the fact that 35 of these 50 CMLs have been shown to be transcriptionally upregulated under various stress responses (McCormack et al. 2005).

Among the collection of CMLs that are induced by stress responses are the phylogenetically related proteins Arabidopsis *CML38* and its homolog tobacco *rgsCaM*. *CML38* is acutely induced at the transcriptional level by hypoxia, with transcript levels accumulating to over 300-fold that of unstressed plants. This is accompanied by rises in protein levels which are undetectable in unstressed plants (Lokdarshi et al. 2016). CML38 was also shown to be upregulated by Turnip mosaic virus (TuMV) or transgenic expression of the TuMV suppressor of silencing Helper-Component Proteinase (HC-Pro) (Endres et al. 2010). The same was shown with respect to *Nt-rgsCaM* and Tobacco

etch virus HC-Pro (Anandalakshmi et al. 2000), which suggests that rgsCaM and CML38 may possess a conserved function as a target for HC-Pro. This is supported in the present work by FRET measurements that demonstrates the interaction of TuMV HC-Pro and rgsCaM *in planta*. Interestingly, it was further shown that *CML38* upregulation by HC-Pro required the ethylene responsive transcription factor RAV2 (Endres et al. 2010). Since ethylene signaling is a major component of the plant hypoxia response (Bailey-Serres et al. 2012, Fukao et al. 2019), these findings suggest that ethylene signaling may be a point of convergence between the plant stress responses to hypoxia and TuMV infection, leading to the downstream upregulation of rgsCaM and CML38.

The structural analysis of the rgsCaM-like clade supports functional conservation between rgsCaM and CML38. The close sequence similarity among the Arabidopsis CMLs clustering with with tobacco rgsCaM, CML37, 38, 39 and 41, and in some reports also CML40, result in their clustering within a phylogenetic clade (Figure 5). In addition to sequence similarity, they also have common structural features that differentiate them from *bona fide* calmodulins. rgsCaM, CML37, 38, 40, and to a lesser extent CML39, all have N-terminal extensions beyond the calmodulin domain containing the EF-hands (Figure 2 and Figure 31). As compared to calmodulins, the third EF-hand of these CMLs have significant substitutions deviating from the EF-hand calcium binding loop motif, with substitutions that are predicted to disrupt or abolish high affinity calcium binding. For instance, all rgsCMLs in Figure 48 have a substitution at the invariant first position aspartate which is conserved in virtually all functional EF hands and contribute a side chain oxygen to calcium coordination (Nakayama et al. 1994). CML37, 38, and 39 lack the conserved glycine at position five, and all a lacking the conserved glutamate residue

at the last position of 12 which is essential for high affinity calcium binding (Figure 48) (Nakayama et al. 1994). This analysis shows that all of these rgsCaM-like proteins likely have their third EF-hand disrupted in a manner that would affect calcium binding. All but CML40 have some amount of N-terminal extension.

As discussed earlier, there is ample evidence that rgsCaM is an endogenous suppressor of gene silencing, but this is less clear for CML38. Preliminary findings showed that overexpression of CML38 in Arabidopsis does not produce obvious HC-Pro-like morphological defects (Foreman 2012), unlike with overexpression of rgsCaM in tobacco (Anandalakshmi et al. 2000). However, HC-Pro-expressing plants with only one functional copy of *CML38* show a reduced HC-Pro phenotype (Foreman 2012). CML38 is also functionally linked to the suppression of silencing activities of HC-Pro, since it was shown that haploinsufficiency of *CML38* impairs the ability of HC-Pro to suppress virus-induced and transgene silencing, but not the miRNA pathway (Foreman 2012). CML38 was also reported to interact *in vivo* with TuMV HC-Pro by bimolecular fluorescence complementation (BiFC) (Lokdarshi 2015).

4.2 CML38 delays TuMV infection

Based on results obtained here as well as previous results (Foreman, 2012), it is apparent that there are conflicting effects of CML38 on TuMV infection. Cml38ko and constitutive expression lines were compared to wt in a TuMV infection assay, with the surprising finding that CML38 constitutive expression delayed systemic infection. This observation was surprising since we hypothesized that CML38 would act as an endogenous suppressor of gene silencing and therefore constitutive expression would

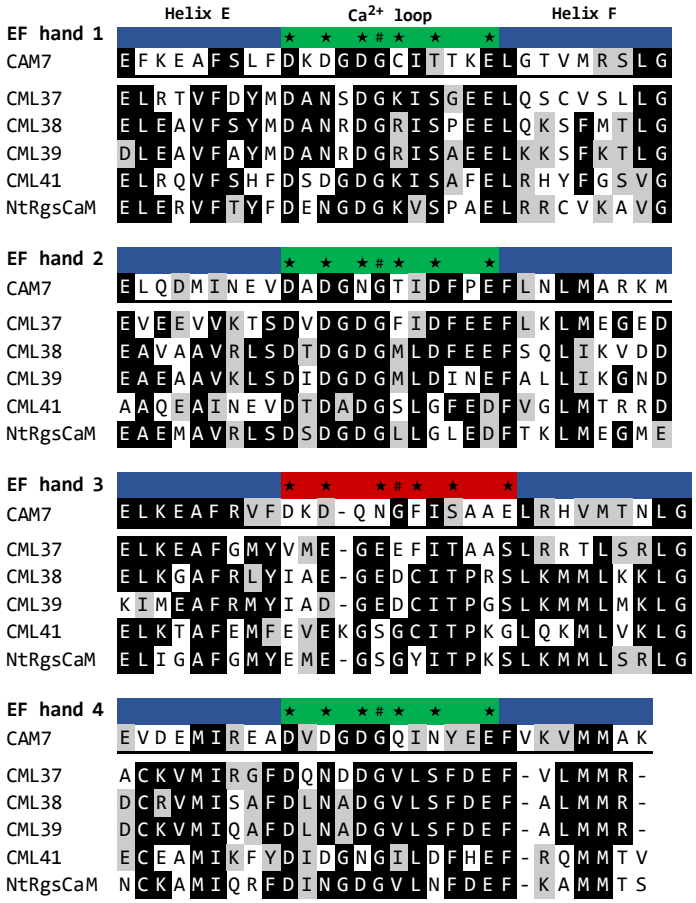

Figure 48 The disrupted third EF-hands of rgsCaM-like proteins. A multiple sequence alignment of CML37, 38, 39 and 41, along with Nt-rgsCaM and At-CaM7 as a CaM reference. The sequences were aligned using MUSCLE (Edgar 2004). The α-helical regions of the EF-hand motifs are shown in blue. The 12 amino acids of the binding loop are shown in green. The predicted disrupted EF3 binding loops are shown in red. Positions 1, 3, 5, 7, 9 and 12 in each loop contribute oxygen atoms which are involved in Ca^{2+} coordination and are shown with stars, and the conserved glycine residue at position 6 is shown with "#". This G6 is required for flexibility and a turn in the backbone of the loop. Residue shading indicates >50% identity (black) or >50% similarity (grey).

allow viruses to replicate more quickly. One reason for CML38-induced delay in viral infection, based on the autophagy model proposed here, is that CML38 could promote degradation of viral targets. CML38 interacts with the TuMV viral suppressor of silencing, HC-Pro (Lokdarshi 2015), similar to as rgsCaM, which interacts with TEV HC-Pro (Anandalakshmi et al. 2000, Nakahara et al. 2012). HC-Pro interacts with other viral proteins, including VPg, the viral protein linked to the viral genome (Ala-Poikela et al. 2011). Since rgsCaMs can degrade proteins in complex with their direct targets (Li et al. 2017), interaction of CML38 with HC-Pro and other viral proteins and genomes could provide a route for autophagic degradation.

In support of this role for CML38 in inducing the autophagic degradation of TuMV and a delay in systemic infection, a recent study has also identified selective autophagy as antiviral for TuMV (Hafren et al. 2018). Autophagy has a well-established role in targeting foreign pathogens for degradation, including viruses (Frankel et al. 2017). This is called xenophagy (Frankel et al. 2017). However, it is also well-established that some animal viruses have evolved to hijack autophagy to promote viral replication. For example, polio, measles, influenza and hepatitis C all capitalize on phagophores as a source of membranes for their viral replication complexes. Degradation is prevented by disrupting fusion to the lysosome, inhibiting lysosomal function, or evolving resistance to the lysosomal hydrolases and low pH conditions (Frankel et al. 2017). This is not the case for TuMV, however. TuMV HC-Pro is targeted for xenophagy by the Arabidopsis autophagy cargo adaptor NBR1, along with the associating viral proteins, viral genome, and host factors (Hafren et al. 2018). However, viral proteins antagonize the selective autophagy by NBR1. Upregulation of NBR1 also upregulates bulk autophagy, which

promotes cell survival and delays cell death, allowing more time for viral replication (Hafren et al. 2018).

Since CML38 delayed TuMV infection, this could be due to it successfully degrading its binding partner HC-Pro through selective autophagy, along with its associated viral cargo. At the same time, CML38 is induced by TuMV HC-Pro (Endres et al. 2010), possibly for a necessary role in suppressing antiviral silencing. One can speculate that if CML38 functions as a suppressor of gene silencing for TuMV, while also causing some amount of degradation of TuMV components, there may be a tradeoff between suppressing host defenses and suffering impaired, but ultimately successful replication. When CML38 degrades SGS3, this promotes viral replication, but when it degrades HC-Pro it is inhibitory.

4.3 rgsCaM targets mRNP bodies under hypoxia stress

Major findings from this work show that rgsCaM (Figure 14) and CML38 (Figure 8) localize to cytosolic foci that are induced in response to hypoxia stress. The two homologs differ somewhat in how these foci interact with or overlap with other mRNP bodies. CML38 was shown to localize within SGs (Figure 9) and PBs (Figure 12) (Lokdarshi et al. 2016). In contrast, rgsCaM localized principally to bodies that were independent of SGs and PBs, but these were often seen in association with these other bodies at the periphery (Figure 15 and Figure 18). Live-cell videos were also recorded showing rgsCaM bodies traffic to and dock at the surface of PBs (Figure 20). For reference, Table 3 and Table 4 shows a compilation of all colocalization quantifications

from representative images for Pearson's correlation coefficients and Mander's co-localization coefficients, respectively.

SGS3 granules have been described as siRNA bodies because SGS3, RDR6, and AGO7 are found here (Jouannet et al. 2012). These have been proposed to act as potential sites of SG nucleation since they acquire SG-marker proteins under heat stress (Jouannet et al. 2012). This identification that SGS3 bodies become SGs makes it surprising that rgsCaM did not localize within SGs, since a direct binding partner, SGS3, should reside there. We performed colocalizations with rgsCaM and SGS3, as well as SGS3 and RBP47 or DCP1 to try to understand the overlap between these granule types.

With respect to SGS3 granules, under hypoxia both rgsCaM and CML38 strongly colocalized to hypoxia-induced cytosolic SGS3 bodies (Figure 22 and Figure 29), and the signals were indistinguishable. We also verified that hypoxia-induced SGS3 granules are indeed SGs, by showing that the localizations of SGS3 and RBP47B were also indistinguishable. Together with the prior similar findings with respect to heat stress (Jouannet et al. 2012), the proposal that SGS3 bodies nucleate SG formation may be generalizable to other abiotic stresses, or possibly any condition which induces SG formation. Our results showed that co-expression of rgsCaM with SGS3 appears to relocalize rgsCaM within SGs rather than to the periphery. This effect was more obvious during co-expression that when rgsCaM was transfected alone and suggests that overexpression of SGS3 may recruit rgsCaM to SGs. This finding is consistent with

Table 3 Pearson's correlation coefficients

	RBP47	DCP1	SGS3	ATG8e
RgsCaM	0.478	0.368	0.578	0.882
RBP47	-	-	0.66	-
DCP1	-	-	0.171	-

Table 4 Mander's co-localization coefficients

	MCC
DCP1:rgsCaM	0.961
rgsCaM:DCP1	0.081
RBP47:rgsCaM	0.115
rgsCaM:RBP47	0.181
RBP47:SGS3	0.937
SGS3:RBP47	0.88
rgsCaM:ATG8e	0.84
ATG8e:rgsCaM	0.827
rgsCaM:SGS3	0.954
SGS3:rgsCaM	0.865
DCP1:SGS3	0.106
SGS3:DCP1	0.12

SGS3 acting as a direct binding partner of rgsCaM and CML38. Since rgsCaM is shown to degrade SGS3 by autophagy, this further suggests that SGS3 may recruit rgsCaM to SGs under hypoxia and lead to the degradation of SGs.

4.4 rgsCaM interaction with ATG8 resembles that of autophagy cargo adaptors

Autophagy, literally “self-eating,” is a mechanism by which cells degrade and recycle material from the cytosol (Zaffagnini et al. 2016). The material degraded by this pathway can be organelles, such as damaged mitochondria or excess peroxisomes, protein aggregates, mRNP bodies, ribosomes, or even pathogens (Zaffagnini et al. 2016). Initially studied in yeast, autophagy was identified as a degradation pathway activated by nutrient deprivation. This nutrient deprivation-triggered autophagy is also called bulk autophagy and is thought to be non-specific in its targeting. Bulk autophagy is now known to be constitutively active at low levels to turnover cellular content, but is greatly upregulated during stresses (Stolz et al. 2014), including hypoxia (Chen et al. 2015). In contrast, selective autophagy recruits specific cargo for degradation. This recruitment is mediated by autophagic cargo adaptors proteins, that bind the phagophore as well as their cargo. Autophagy involves a specialized vesicle called a phagophore, which expands and fuses around its cargo, enveloping it in a double membrane that forms the autophagosome. The autophagosome is trafficked to the vacuole via microtubules with the help of RAB7 (Marshall et al. 2018), and finally fuses to the vacuole (or lysosome in animals) where the inner vesicle membrane is released (an autophagic body) and is subsequently enzymatically degraded and recycled

(Michaeli et al. 2016). Recovered sugars, amino acids, lipids and nucleotides travel back into the cytosol via specific permeases (Marshall et al. 2018).

Autophagosome biogenesis is a complex process involving many “autophagy related proteins” (ATGs). Autophagy is controlled by developmental cues, stresses (unfolded protein response, oxidative stress, heat stress, salt/osmotic stress, hypoxia), and nutrient availability, including reduced carbon and nitrogen (Marshall et al. 2018). The key positive regulator is SUCROSE NON-FERMENTING 1-RELATED KINASE 1 (SnRK1), which is a protein complex forming an AMP-activated protein kinase (Marshall et al. 2018). SnRK1 phosphorylates ATG1 kinase, enabling it to complex with ATG13, ATG101 and ATG11. Together, they regulate downstream ATG proteins which in turn activate three processes of autophagosome formation (Marshall et al. 2018). They activate membrane delivery to the membrane site where the phagophore forms (often the ER membrane, where they phosphorylate and activates ATG9), vesicle nucleation (activates a complex containing ATG6), and phagophore expansion and closure (targets ATG5, ATG12, and ATG16) (Marshall et al. 2018). Autophagy-related 5 (ATG5) is recruited to portions of the ER membrane when autophagy is active, and it forms a ring-like structure to constrict a portion of membrane which will later separate from the donor membrane. ATG5 also plays a role in recruiting ATG8, which is plays a central role in selective autophagy as it binds to cargo adaptor proteins which deliver appropriate cargo to the phagophore (Michaeli et al. 2016).

ATG8 has a ubiquitin fold and is cleaved near its C-terminus by ATG4 peptidase to expose a C-terminal glycine. In a process closely analogous to ubiquitination, ATG8

undergoes ATP-dependent activation by ATG7, is transferred onto ATG3, and is lastly conjugated onto phosphatidyl ethanolamine by the ATG5, ATG12 and ATG16 complex. This conjugation involves the formation of an ester linkage between the ATG8 C-terminal glycine and the PE amino group (Stolz et al. 2014, Michaeli et al. 2016, Marshall et al. 2018). ATG8 then recruits proteins containing BIN/AMPHIPHYSIN/RYS (BAR) domains and SRC HOMOLOGY-3 (SH3) domains which induce membrane curvature and phagophore production (Marshall et al. 2018). ATG8 recruits cargo destined for autophagy by binding an ATG8-interacting motif (AIM) on a cargo adaptor protein. The cargo adaptors in-turn bind their cargo. Following autophagosome formation and fusion to the vacuole, the cargo, the cargo adaptor and ATG8 on the inner membrane are degraded following vacuole fusion (Marshall et al. 2018).

Given the energy crisis associated with hypoxia, one would predict that autophagy may play an important role in recycling nutrients during prolonged low oxygen stress. In support of this, it has been shown that flooding stress transcriptionally upregulates autophagy related genes (ATGs), increases the number of autophagosomes visible by microscopy, and increases autophagic turnover, as evidenced by increased turnover of GFP-ATG8e (Chen et al. 2015). Further, five different mutants of autophagy-related genes were tested and all show pronounced increases in sensitivity to hypoxia as indicated by reduced survivability compared to wt (Chen et al. 2015). Given this evidence that autophagy is an important component of hypoxia survival, our work suggests that the rgsCaMs may be critical components in this process, by targeting material stored in SGs and PBs for recycling during this energy crisis.

Nt-rgsCaM was first reported to degrade the viral suppressors of silencing HC-Pro (potyviruses) and 2b (bromoviruses) by autophagy (Nakahara et al. 2012). Later, the same was shown for Nb-rgsCaM and the endogenous PTGS proteins NbSGS3 and NbRDR6 (Li et al. 2017). Further, BiFC assays demonstrated that the EF1 and EF2 domains of Nb-rgsCaM interact with the zinc-finger and coiled-coil domains of NbSGS3. However, Nb-rgsCaM did not directly interact with RDR6 (Li et al. 2017), suggesting that RDR6 degradation by rgsCaM is mediated through its interaction with SGS3. In agreement with these findings, overexpression of Nb-rgsCaM in *N. benthamiana* reduced the number of SGS3 granules, and co-expression of Nb-SGS3 and rgsCaM yielded lower rgsCaM protein levels than rgsCaM expression alone, indicating that rgsCaM becomes degraded itself as it induces SGS3 degradation (Li et al. 2017)

During the course of this study, evidence emerged which suggests that rgsCaMs target their binding partners for degradation by autophagy (Nakahara et al. 2012, Li et al. 2017). To investigate the connections between autophagy and rgsCaM granules, we performed colocalizations with the autophagy marker ATG8e. ATG8e strongly colocalized with rgsCaM in cytosolic foci (Figure 32). Since ATG8e resides at the surface of the growing phagophore, colocalization with rgsCaM implies that rgsCaM may act as a bridge between the phagophore and SGs and PBs, to which rgsCaM granules dock under stress. This hypothesis was further supported with a colocalization in which rgsCaM and ATG8e were co-expressed with an mRNP marker, DCP1 for processing bodies in this case (Figure 39). rgsCaM and ATG8e both appeared at the periphery of the PB, apparently surrounding it (Figure 39). These results are consistent with the

behavior of autophagic cargo adaptors, which bind ATG8e and recruit cargo to the phagophore.

To test the cargo adaptor model, direct interaction between rgsCaM and ATG8e was investigated by ratiometric BiFC. Wt rgsCaM and ATG8e showed a robust BiFC signal when compared to the negative control CaM2, a *bona fide* CaM (Figure 35 and Figure 36). To probe if the putative rgsCaM AIM motif is required for its interaction with ATG8e, we first tested a truncation of rgsCaM that retains the calcium sensor domains but lacks the N-terminal extension. This pairing showed nearly undetectable BiFC fluorescence that was indistinguishable from the negative control (Figure 35 and Figure 36). We next tested two site-directed mutants of the AIM motif. The F15A mutant substituted the aromatic amino acid of the AIM for an alanine. As with the N-terminal truncation, this disruption of the AIM motif abolished interaction with ATG8e (Figure 35 and Figure 36) The second mutation site, S16A, overlaps with the AIM motif, but resides at one of the positions which can be any amino acid. This substitution also prevented interaction (Figure 35 and Figure 36). The potential significance of the S16A mutation will be discussed in the next section.

Two mutants of ATG8e were also tested with wt rgsCaM. G118A substituted the glycine which is required for conjugation to the phagophore membrane. L52A is an equivalent mutation to the described L50A in the animal homolog of ATG9, LC3. This mutation disrupts the ATG8 hydrophobic W binding pocket that binds the aromatic amino acid of cargo adaptor AIM motifs (Yamaguchi et al. 2010). This mutation also prevents lipidation, since ATG3 (the E2 ubiquitin conjugation analog) must bind to ATG8 via its

own AIM motif to catalyze lipid conjugation. Since both G118A and L52A showed no interaction with ATG8e (Figure 35 and Figure 36), ATG8e conjugation to the phagophore membrane appears to be a requirement for interaction with rgsCaM. Taken together, the BiFC analysis of the rgsCaM and ATG8e interaction strongly suggests a direct interaction between the rgsCaM ATG8-interacting motif and lipidated ATG8e. The robust rgsCaM-ATG8e BiFC signal was lost when ATG8e could not be lipidated or when the region of the AIM motif of rgsCaM was disrupted or removed (Figure 35 and Figure 36). The F15A rgsCaM mutant is the most informative here. This phenylalanine would be critical for an AIM motif, which requires an aromatic residue at this position (Tzfadia et al. 2013, Marshall et al. 2018). Substitution with an alanine maintains the hydrophobic properties, but none-the-less shows a dramatic loss in ATG8e binding, providing evidence that this site is a *bona fide* AIM domain.

While rgsCaM and CML38 contain conserved FxxL motifs, most, but not all, plant AIMs also contain neighboring acidic residues (Tzfadia et al. 2013), which are absent in rgsCaM and CML38. Acidic residues around the AIM participate in electrostatic contacts with lysines and arginines found in the ATG8 binding pocket (Liu et al. 2018). More specifically, there is a preference for one or more acidic amino acids within the range of three positions upstream of the [F,W,Y], to two positions downstream from the [L,I,V] position, including the two non-specific bases in the middle (Tzfadia et al. 2013). Not only do rgsCaM and CML38 lack acidic residues in this region, there are several basic residues (Figure 31). Interestingly, there are examples of AIMs which are regulated by phosphorylation in plants under abiotic stress (Nolan et al. 2017). The growth-promoting, brassinosteroid-responsive transcription factor BRI1-EMS SUPRESSOR 1

(BES1) is degraded with the help of the autophagy cargo adaptor protein DOMINANT SUPPRESSOR IF KAR 2 (DSK2) (Nolan et al. 2017). The AIMs of the DSK2 cargo adaptor are inactive until serine and threonine residues around the AIMs are phosphorylated by BRASSINOSTEROID INSENSITIVE 2 (BIN2) kinase (Nolan et al. 2017). Drought and starvation stress induce BIN2 to initiate this process leading to the autophagic degradation of this growth-promoting transcription factor (Nolan et al. 2017), and to energy conservation. It is tempting to speculate that a similar approach could regulate the AIM domain of rgsCaM, leading to the autophagic degradation and recycling of mRNP content during the hypoxia energy crisis.

We investigated if the rgsCaM AIM motif is regulated by phosphorylation at S16 within the AIM motif. S16 was selected because of its position within the AIM, but also because CML38 contains a *bona fide* phosphorylation site (S10) just two amino acids upstream from this position of the alignment (Wang et al. 2013), and both fall immediately next to the aromatic amino acid of the AIM (Figure 31). Further, the rgsCaM S16 position is a conserved serine in all Solanaceae family members examined (Figure 49). When S16 rgsCaM was tested with ATG8e, this abolished the BiFC signal. S16A does still localize to hypoxia-induced foci (Figure 40), suggesting that this mutation is not disruptive to its cargo binding. While this position is not critical for the core AIM motif, it is conserved, and may serve to provide negative electrostatics following stress-induced phosphorylation, enabling binding to ATG8. Testing an rgsCaM phosphomimic mutation (S16D) for BiFC with ATG8e will be an essential next step in testing this hypothesis.

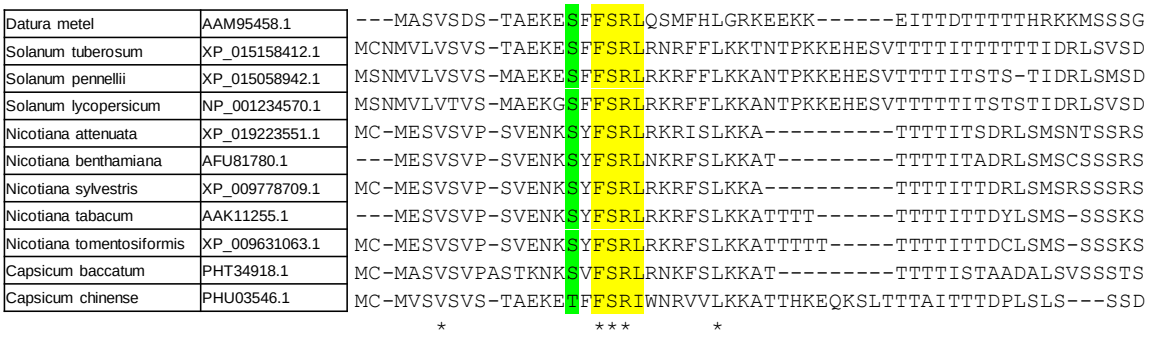

Figure 49 Multiple sequence alignment of rgsCaM homologs of the Solanaceae family. The sequences upstream of the E-helix of the first EF hand are shown (N-terminal domains) for rgsCaM homologs from the indicated Solanaceae species. Accession numbers are shown. The FXXL, or FXXI AIM motifs are highlighted in yellow. The F16 of rgsCaM is the second amino acid in the yellow sequence and is conserved in all Solanaceae rgsCaM homologs. The serine or threonines two positions upstream from the AIM is highlighted in green and represents another potential conserved phosphorylation site. Asterisks indicate positions which are identical across all homologs.

. In support of the hypothesis of rgsCaM AIM regulation, there are examples of plant proteins with AIM domains that are activated during hypoxia (Zhan et al. 2018). For example, S-nitroso-glutathione reductase 1 (GSNOR1) contains an AIM motif which is structurally inaccessible for ATG8 binding during normoxia (Zhan et al. 2018). During hypoxia, nitric oxide (NO) induces S-nitrosylation of C10 of GSNOR1 (Zhan et al. 2018). This cysteine nitrosylation induces a conformational change that exposes the AIM domain and allows GSNOR1 to bind ATG8, thus becoming recruited for selective autophagy (Zhan et al. 2018). While this mechanism relies on nitrosylation rather than phosphorylation, it does provide precedent for AIM regulation during hypoxia.

4.5 rgsCaM S16 affects nuclear localization

Examination of the subcellular localization of S16A rgsCaM reveals that similar to rgsCaM it localizes to hypoxia-induced foci. However, we noticed that it also shows significantly greater nuclear localization than wt rgsCaM (Figure 40). While the significance of this observation is not yet clear, it does suggest that the N-terminal domain also influences nuclear localization. Based on our proposed model, phosphorylation of rgsCaM at S16 would cause it to interact with lipidated ATG8, which is a cytosolic protein (Stolz et al. 2014). This could provide additional recruitment to the cytosolic compartment as one possible explanation.

Several lines of evidence suggest nuclear functions for rgsCaMs. Over-expression of rgsCaM in *N. tabacum* plants undergoing sense-transgene silencing showed perturbed splicing of the silenced gene (Shin et al. 2014). In lines undergoing sense-transgene silencing of the ω-3 fatty acid desaturase (*Nt-FAD3*) gene, the

endogenous *Nt-FAD3* transcripts showed splicing defects including intron retention and loss of some exons (Shin et al. 2014). This silenced line was crossed to rgsCaM-overexpressing plants, and most of these lines (70%), showed the expected reversal of the transgene silencing, and reduced *Nt-FAD3* siRNAs (Shin et al. 2014). However, the remaining (30%) failed to reverse silencing. Instead, these non-reversal lines showed a different pattern of *Nt-FAD3* intron retention than the lines without rgsCaM-over-expression, suggesting rgsCaM could be influencing splicing (Shin et al. 2014). Stress granule association of rgsCaM and CML38 is also suggestive of nuclear roles. This is because many of the SG RNA-binding proteins, including the RNA-recognition motif (RRM) proteins are normally found in the nucleus and are involved in RNA splicing and processing (Albà et al. 1998). This creates another potential link between rgsCaMs and RNA splicing. rgsCaM also appears to show changes in nuclear localization induced by HC-Pro (discussed below).

4.6 rgsCaM as a calcium sensor

While the role of calcium in the regulation of rgsCaM is unknown, the results here suggest that there is a stress-induced signal that regulates rgsCaM. While some SGS3 granules are constitutively present, at early timepoints of hypoxia rgsCaM does not appear to interact with SGS3 at SGS3-associated granules (Figure 23). Further, SGS3 granules increase in number in response to hypoxia prior to rgsCaM granulation (Figure 23). However, once rgsCaM does granulate, they appear in the same sites (Figure 23). If the SGS3 and rgsCaM interaction were not regulated, one would expect rgsCaM to reside in those SGS3 granules in the absence of stress. Since rgsCaM is a calmodulin-

like protein, and changes in cytosolic calcium are known to punctuate the various steps of hypoxia initiation, sustained duration and reoxygenation (Sedbrook et al. 1996), a calcium signal is an obvious candidate. Sustained calcium spiking throughout hypoxia (Sedbrook et al. 1996) could induce rgsCaM and CML38 localization to mRNP bodies and enable the interaction with SGS3. BiFC assays showed that SGS3 interacts with the first two EF hands of rgsCaM (Li et al. 2017). While the role of calcium in this interaction is not yet clear, the fact that SGS3 interacts with the rgsCaM lobe containing two functional EF hands allows for this possibility.

There are some observations that would tend to challenge whether the calcium regulatory paradigm of canonical calmodulins applies to rgsCaM. First, all rgsCaM-like proteins have one disrupted EF-hand (Figure 48), which would be predicted to lower calcium binding affinity. Second, in a biophysical study of recombinant rgsCaM, the K_d values for calcium binding events were found to be above the range of calcium sensors (Makiyama et al. 2016), although the possibility of influences from *in vivo* binding partners on calcium binding were raised (Makiyama et al. 2016). While these results are consistent with predictions of a disrupted EF hand, the *in vivo* calcium affinities could be influenced, possibly by protein-protein interactions, as the authors suggest (Makiyama et al. 2016). Third, when rgsCaM and SGS3 were co-transfected into *N. benthamiana* by Li *et. al* (2017), Western blotting indicated that rgsCaM induced the autophagic turnover of SGS3 in the absence of any other stress. FRET-based *in vivo* studies on the interactions between rgsCaM and its binding partners (SGS3, HC-Pro, ATG8) coupled with calcium manipulations can help to identify if any of the known interactions (or localizations) are affected by calcium.

4.7 Model: rgsCaM induces mRNP recycling during stress

The results presented here lead me to propose a model in which rgsCaM-like proteins may act as cargo adaptors for the recruitment of mRNP bodies to phagophores under stress (Figure 50). The following model description references the lettered portions of Figure 50. **(a)** Regulator of gene silencing calmodulin-like proteins (rgsCMLs) have been shown to accumulate transcript and protein under stress conditions: CML38 with hypoxia and potyviruses, and rgsCaM with potyviruses. Stresses, including hypoxia and viral infection, commonly activate calcium signaling, which, according to the calmodulin paradigm, will activate calcium sensor proteins resulting in activation of downstream targets. **(b)** A direct target of rgsCaM, suppressor of gene silencing 3 (SGS3) resides in siRNA bodies and/or stress granules. **(c)** siRNA bodies contain SGS3 and RDR6, key proteins of the silencing pathway which produces secondary viral siRNAs (vsiRNAs) for antiviral systemic immunity, as well as tasiRNAs. Upon hypoxia stress, SG proteins including RRMs join siRNA bodies becoming SGs. **(d)** rgsCaM has diffuse cytosolic localization in unstressed cells, but localizes to the periphery of SGs and processing bodies (PBs) in response to hypoxia stress. Whether viral infection causes a similar redistribution is unknown. However, HC-Pro has been shown to localize to cytosolic foci (del Toro et al. 2014). **(e)** rgsCaM is known to induce the autophagic degradation of several direct interacting partners (Nakahara et al. 2012, Li et al. 2017), including SGS3 (Li et al. 2017), along with those in complex. We provide evidence that rgsCaM contains an ATG-interacting motif for binding autophagy related protein 8e (ATG8e), which recruits cargo for autophagy. We propose that rgsCaM and

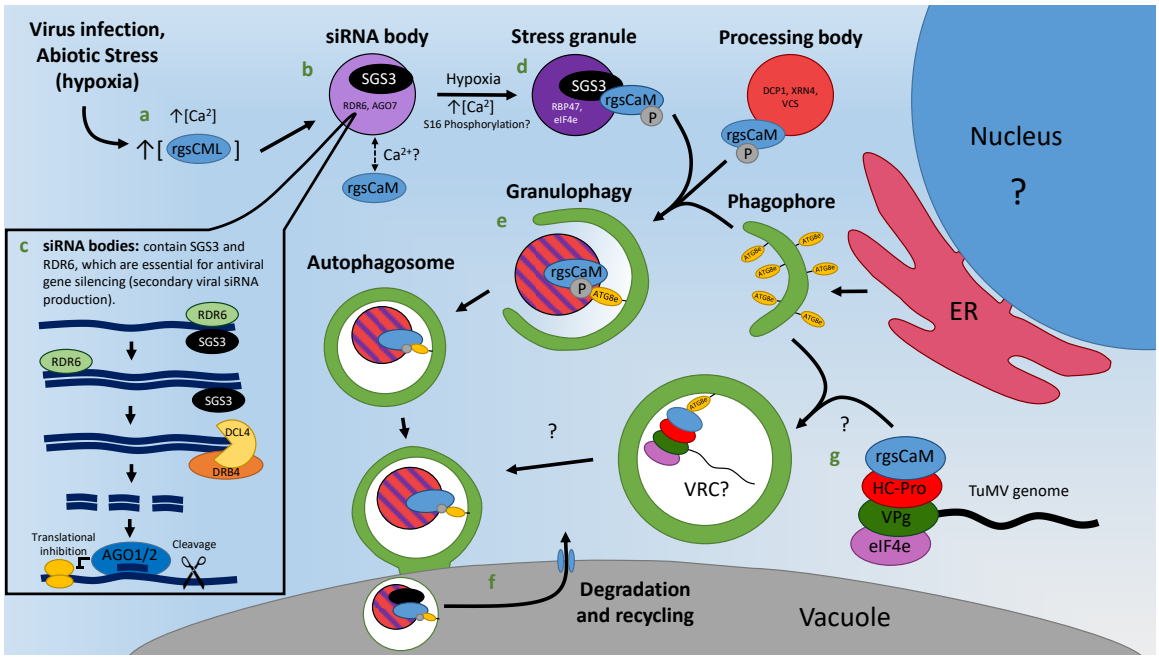

Figure 50 Model for rgsCaMs as autophagic cargo adaptors for stress-induced degradation of mRNP bodies. See main text for complete description. Stress induces expression of rgsCaMs. Nt-rgsCaM is upregulated by potyviruses while At-CML38 is upregulated by hypoxia and potyviruses. rgsCaM is an endogenous suppressor of silencing which targets SGS3, which is in the context of siRNA granules containing key enzymes of the antiviral and endogenous silencing pathway shown. rgsCaM associates with siRNA bodies after hypoxia, but not before, suggesting the possibility of a calcium signal regulating this interaction. rgsCaM associates at the periphery of SGs and PBs under hypoxia. rgsCaM interacts with ATG8e on phagophores and recruits mRNPs as cargo for degradation in the vacuole and recycling. rgsCaM may require phosphorylation at S16 for ATG8e binding. rgsCaM also interacts with potyviral HC-Pro, and so suggests a similar mechanism may lead to recruitment of viral components to autophagosomes, leading to degradation of TuMV, but other viruses may hijack the autophagosome as a viral replication center. Letters are referenced in the main text.

its homolog CML38 act as autophagy cargo adaptors for the recruitment of mRNPs (siRNA bodies/SGs and PBs) into autophagosomes (granulophagy) under stress. **(f)** Autophagic degradation of these mRNPs can recycle material to prolong survival under the hypoxia energy crisis and may also play roles in controlling gene expression at the RNA level. **(g)** The plant potyvirus Turnip mosaic virus expresses a suppressor of gene silencing called helper component proteinase (HC-Pro) which binds rgsCaM (Anandalakshmi et al. 2000), (Figure 41). HC-Pro induces expression of and requires rgsCaM/CML38 for some of its suppression of silencing activities (Endres et al. 2010, Foreman 2012). Activation of rgsCaM leads to the autophagic degradation of siRNA granules and suppresses plant antiviral silencing. HC-Pro also interacts with a network of other viral proteins, including VPg, the viral protein linked to the genome (Ala-Poikela et al. 2011). This raises the possibility that rgsCaM could also recruit viral proteins and genomes into autophagosomes. If these autophagosomes fuse to the lysosome it would delay infection. Alternatively, viruses could inhibit lysosomal fusion and hijack this process as a means of delivering membrane to isolate viral replication complexes from host silencing machinery. The former degradation hypothesis is supported by our observation that CML38 constitutive expression in Arabidopsis delays TuMV infection. Since DNA geminiviruses have been reported to have accelerated infection in response to constitutive rgsCaM expression (Li et al. 2014, Yong Chung et al. 2014), this may be specific to TuMV.

Granulophagy is an established means of clearing SGs and PBs in mammals and yeast (Frankel et al. 2017), but has not yet been demonstrated in plants. In yeast, mutants in late stages of autophagy show an accumulation of RNA granules (Frankel et

al. 2017). Human cells have also been shown to target SGs for lysosomal degradation by autophagy (Frankel et al. 2017). The yeast ATPase Cdc48 and the human homolog vasolin-containing protein (VCP) play critical roles in granulophagy (Buchan et al. 2013). Cdc48 forms a hexamer with a central pore containing its ATPase domains. Each Cdc48 monomer binds cofactor proteins at the N- and C-termini, which reside on either end of the barrel-shaped hexamer. The cofactors provide substrate targeting and catalytic roles. Cdc48 is primarily involved in adding and removing ubiquitins, remodeling protein complexes with its ATPase activity, and in extracting proteins from complexes for degradation (Baek et al. 2013). It is involved in numerous processes, including autophagy, protein degradation, apoptosis, DNA replication, DNA repair, and gene expression (Baek et al. 2013). In yeast and in humans, loss of Cdc48/VCP leads to increased numbers of SGs (Buchan et al. 2013). Cdc48 is implicated protein inclusion body diseases, such as Parkinson and Huntington diseases (Baek et al. 2013). During nutrient starvation, Cdc48 with its cofactor Ubx1 bind to lipidated ATG8 and are thought to play a role in autophagosome closure around its cargo. Cdc48-mediated extraction of ATG8 from the phagophore membrane is proposed to contribute to this closure. Cdc48 is also implicated in autophagy of ribosomes (ribophagy) and mitochondria (mitophagy) (Baek et al. 2013). Given its broad role in autophagy, and granulophagy in particular, Cdc48 likely contributes to the granulophagy function proposed for rgsCaM/CML38. In support of this, Cdc48A was one of the proteins identified in a CML38 immunoprecipitation from hypoxia-treated Arabidopsis seedlings (Lokdarshi et al. 2016). Since rgsCaM appears to directly bind ATG8e, no specific role in this cargo adaptor

model is proposed for Cdc48, but its potential involvement is are an area of interest in future work.

In human cells, granulophagy of SGs is also promoted by phosphorylation (Krisenko et al. 2015). The tyrosine kinase SYK becomes phosphorylated in response to treatment with sodium arsenite (Krisenko et al. 2015). Arsenite treatment leads to oxidative stress and induction of SGs (Basu et al. 2017). Following phosphorylation, and with the help of its partner Grb7, Syk is recruited to SGs, where it phosphorylates proteins in and around the SG (Krisenko et al. 2015). Syk activity promotes autophagosome formation and SG degradation (Krisenko et al. 2015). If a similar mechanism occurs in plants, this could provide the S16 phosphorylation of rgsCaM bound at the periphery SGs or PBs.

4.8 The suppression of silencing of rgsCaMs

As discussed in section 1.4.2, rgsCaM suppresses virus-induced gene silencing, sense transgene silencing and silencing by endogenous trans-acting siRNA, however additional silencing pathways use RDR6 and SGS3 which have not yet been studied for suppression by rgsCaMs. These include the naturally antisense RNAs (natsiRNAs) and a type of transcriptional gene silencing (TGS) siRNA, the epigenetically activated siRNAs (easiRNAs) (Bologna et al. 2014). The degree of dependence of these biogenesis pathways on RDR6 will likely determine the degree to which these pathways are affected by rgsCaM, but these can be further investigated.

rgsCaM may suppress RNA-directed DNA methylation (transcriptional gene silencing). Along with RNA silencing, TGS is an important arm of the defense against

DNA viruses (Kumar 2019). Since rgsCaM degrades SGS3 and RDR6, rgsCaM can suppress the biogenesis of both secondary viral siRNAs and endogenous tasiRNAs, owing to their convergent pathways following the action of RDR6 and SGS3. Interestingly, tasiRNAs from the *TAS1c* and *TAS3a* loci have been shown to induce DNA methylation at their respective *TAS* loci as part of a feedback inhibition mechanism (Wu et al. 2012). This methylation requires SGS3 and RDR6 *(Wu et al. 2012)*. Secondary viral siRNA produced by this same pathway, from the RNA intermediates of DNA viruses, could also be involved in TGS against viral DNA, and rgsCaM-induced degradation of SGS3 and RDR6 would be expected to inhibit this process. The potential roles of rgsCaMs in TGS should be further investigated.

4.9 Future directions for rgsCaM-like proteins

Many aspects of how rgsCaM and its homologs function with respect to mRNPs remain unresolved. While rgsCaM bodies were seen to dock onto SGs and PBs, the identity of other proteins within these rgsCaM bodies is unknown. The requirement of calcium for rgsCaM localization to cytosolic granules and for interaction with SGS3 also need to be investigated. Experiments with ionophores in transfected protoplasts could address this, as could investigating rgsCaM localizations and BiFC interactions in a mutant with disruptions introduced to all EF hands. Beyond these, many additional research questions arise. Does rgsCaM co-immunoprecipitate with ATG8e? Does this change when calcium or EGTA is present in the buffer? Does the S16D rgsCaM mutant show a positive BiFC with ATG8e? Is this signal higher than wt rgsCaM as would be predicted by the model? What kinase is responsible? How does TuMV infection affect

SG formation and rgsCaM localization? What are the nuclear functions of rgsCaM and CML38? Which of the other Arabidopsis rgsCaM-like proteins can suppress VIGS or S-PTGS? What stresses induce rgsCaM expression in tobacco? Granulophagy with rgsCaM as a cargo adaptor can be further tested. Does treatment with autophagy inhibitors increase the number of rgsCaM granules under hypoxia? Does silencing or knock-out of rgsCaM increase the number of SGs or PBs seen or the abundance of representative resident proteins under hypoxia? What happens during reoxygenation? Do ATG8e and rgsCaM co-localizing foci undergo rapid degradation?

4.10 The pHypox 2 construct is a promising system for reporting in vivo hypoxia

A secondary project in this work was to generate genetically-encoded hypoxia sensor. The pHypox 2 plasmid produced here encodes a nuclear-localized YFP sensor that is designed to be constitutively expressed, but rapidly degraded in the presence of dissolved oxygen. The first 28 amino acids of the sensor come from the RAP2.12 ERF group VII transcription factor, which has evolved as a direct oxygen sensor (Licausi et al. 2011). The N-terminal residue following methionine cleavage is a cysteine, which is a tertiary destabilizing residue in the N-degron system of proteolytic degradation (Weits et al. 2014). When oxygen is present, plant cysteine oxidases (PCO) oxidize the cysteine, and subsequent action of an arginyl transferase attaches an N-terminal arginine, which is a highly destabilizing N-degron (Weits et al. 2014). The arginyated protein is then rapidly degraded by the ubiquitin proteasome system (Weits et al. 2014). In addition to the N-degron from RAP2.12, the hypoxia sensor contains a nuclear localization signal and three tandem YFP moieties.

The hypoxia sensor should be rapid and quantitative biosensor for oxygen. Since the engineered hypoxia sensor is regulated post-translationally by a direct oxygen sensing mechanism, it should show a rapid response when compared to promoter-based systems, such as an *ADH1* promoter expressing YFP. The system is also designed to be quantitative. Since both the sensor and a constitutive mScarlet fluorescent protein are expressed from 35S promoters, they should show similar expression levels relative to each other within every cell where they are expressed, even when different tissues show different expression levels. Results thus far have shown that the sensor is undetectable in normal oxygen conditions but becomes visible when oxygen is depleted. The mScarlet protein also expressed under both normoxic and hypoxic conditions, and shows nuclear localization. Although there is some residual cytosolic mScarlet, this should not pose a problem so long as the ratio of nuclear to cytosolic mScarlet is stable across tissues. The results indicate that the sensor should function as intended, with hypoxia-dependent YFP fluorescence, and ratiometric quantification based on YFP:mScarlet signal strength in nuclei.

The pHypox 2 oxygen sensor construct has successfully reported on the hypoxia status in transfected plants, but the greatest utility will be in stable transgenic lines. To further asses the promise of this system as a tool in biological research, transgenic Arabidopsis lines have been generated, and T2 plants are undergoing selection. A probable course for this characterization will be discussed. Several homozygous transgenic lines, as well as a small number of their respective heterozygous parent lines for comparison, will be characterized. Evaluating both homo- and heterozygous plants will assess the potential uses of this construct as a sensor-expressing genetic

background for transformations (homozygous) or for crosses to other lines (initially heterozygous). This range of lines will be important to see if expression levels influence the range of the hypoxia sensor sensitivity, or if nearby enhancers might affect expression consistency among tissues. Of primary interest will be to determine the dynamic range of the sensor. Given that the RAP2.12 transcription factor serves to activate hypoxia stress-response genes, the sensitivity is likely already tuned to the tipping point at which plants experience stress, but this will need to be carefully assessed.

This sensor would be especially useful for mapping naturally-occurring microaerobic environments, such as rapidly metabolizing cells, or the nitrogen-fixing symbiotic root nodules of legumes, which employ an oxygen diffusion barrier protect their nitrogenase from oxidation (Minchin 1997). Another application could be to see which cell-types experience hypoxia the earliest. Since this system provides cell-specific reporting on oxygen levels, this reporter would be ideal for experiments at the cellular level which need to be related to oxygen levels. For instance, from our experiments with imaging plant cells under hypoxia, it is evident that the time of SG formation is clearly variable cell-to-cell within a tissue, with each cell perceiving this at slightly different times. However, this time of SG formation may correlate well to a specific fluorescence ratio of the hypoxia reporter, allowing experiments to be tightly calibrated to oxygen levels, and requiring smaller sample sizes to obtain statistically significant results. Further reaching goals would be to demonstrate the sensor's utility in agricultural crops for research in the laboratory as well as in the field. It may also be possible to modify the oxygen sensitivity of the reporter, by mutagenizing the N-terminal RAP2.12

sequence to affect the affinity of the N-degron for cellular E3 ligases. Other approaches could be to affect the expression level of the reporter or the plant cysteine oxidases.

List of references

Adenot, X., T. Elmayan, D. Lauressergues, S. Boutet, N. Bouche, V. Gasciolli and H. Vaucheret (2006). "DRB4-dependent TAS3 trans-acting siRNAs control leaf morphology through AGO7." Curr Biol **16**(9): 927-932.

Ala-Poikela, M., E. Goytia, T. Haikonen, M. L. Rajamaki and J. P. Valkonen (2011). "Helper component proteinase of the genus Potyvirus is an interaction partner of translation initiation factors eIF(iso)4E and eIF4E and contains a 4E binding motif." J Virol **85**(13): 6784-6794.

Albà, M. M. and M. Pagès (1998). "Plant proteins containing the RNA-recognition motif." Trends in Plant Science **3**(1): 15-21.

Anandalakshmi, R., R. Marathe, X. Ge, J. M. Herr, Jr., C. Mau, A. Mallory, G. Pruss, L. Bowman and V. B. Vance (2000). "A calmodulin-related protein that suppresses posttranscriptional gene silencing in plants." Science **290**(5489): 142-144.

Anandalakshmi, R., G. J. Pruss, X. Ge, R. Marathe, A. C. Mallory, T. H. Smith and V. B. Vance (1998). "A viral suppressor of gene silencing in plants." Proc Natl Acad Sci U S A **95**(22): 13079-13084.

Anderson, P. and N. Kedersha (2009). "Stress granules." Curr Biol **19**(10): R397-398.

Baek, G. H., H. Cheng, V. Choe, X. Bao, J. Shao, S. Luo and H. Rao (2013). "Cdc48: a swiss army knife of cell biology." J Amino Acids **2013**: 183421.

Bailey-Serres, J., T. Fukao, D. J. Gibbs, M. J. Holdsworth, S. C. Lee, F. Licausi, P. Perata, L. A. Voesenek and J. T. van Dongen (2012). "Making sense of low oxygen sensing." Trends Plant Sci **17**(3): 129-138.

Bailey-Serres, J., S. C. Lee and E. Brinton (2012). "Waterproofing crops: effective flooding survival strategies." Plant Physiol **160**(4): 1698-1709.

Bailey-Serres, J., R. Sorenson and P. Juntawong (2009). "Getting the message across: cytoplasmic ribonucleoprotein complexes." Trends Plant Sci **14**(8): 443-453.

Bajar, B. T., E. S. Wang, S. Zhang, M. Z. Lin and J. Chu (2016). "A Guide to Fluorescent Protein FRET Pairs." Sensors (Basel) **16**(9).

Basu, M., S. C. Courtney and M. A. Brinton (2017). "Arsenite-induced stress granule formation is inhibited by elevated levels of reduced glutathione in West Nile virus-infected cells." PLoS Pathog **13**(2): e1006240.

Bender, K. W. and W. A. Snedden (2013). "Calmodulin-Related Proteins Step Out from the Shadow of Their Namesake." Plant Physiology **163**(2): 486-495.

Bhullar, S., S. Datta, S. Advani, S. Chakravarthy, T. Gautam, D. Pental and P. K. Burma (2007). "Functional analysis of cauliflower mosaic virus 35S promoter: re-evaluation of the role of subdomains B5, B4 and B2 in promoter activity." Plant Biotechnol J **5**(6): 696-708.

Biekofsky, R. R., S. R. Martin, J. P. Browne, P. M. Bayley and J. Feeney (1998). "Ca2+ coordination to backbone carbonyl oxygen atoms in calmodulin and other EF-hand proteins: 15N chemical shifts as probes for monitoring individual-site Ca2+ coordination." Biochemistry **37**(20): 7617-7629.

Bindels, D. S., L. Haarbosch, L. van Weeren, M. Postma, K. E. Wiese, M. Mastop, S. Aumonier, G. Gotthard, A. Royant, M. A. Hink and T. W. Gadella, Jr. (2017).

"mScarlet: a bright monomeric red fluorescent protein for cellular imaging." Nat Methods **14**(1): 53-56.

Bologna, N. G. and O. Voinnet (2014). "The diversity, biogenesis, and activities of endogenous silencing small RNAs in Arabidopsis." Annu Rev Plant Biol **65**: 473-503.

Bolte, S. and F. P. Cordelieres (2006). "A guided tour into subcellular colocalization analysis in light microscopy." J Microsc **224**(Pt 3): 213-232.

Borges, F. and R. A. Martienssen (2015). "The expanding world of small RNAs in plants." Nat Rev Mol Cell Biol **16**(12): 727-741.

Branco-Price, C., K. A. Kaiser, C. J. Jang, C. K. Larive and J. Bailey-Serres (2008). "Selective mRNA translation coordinates energetic and metabolic adjustments to cellular oxygen deprivation and reoxygenation in Arabidopsis thaliana." Plant J **56**(5): 743-755.

Brunkard, J. O., T. M. Burch-Smith, A. M. Runkel and P. Zambryski (2015). "Investigating Plasmodesmata Genetics with Virus-Induced Gene Silencing and an Agrobacterium-Mediated GFP Movement Assay." Plasmodesmata: Methods and Protocols **1217**: 185-198.

Buchan, J. R., R.-M. Kolaitis, J. P. Taylor and R. Parker (2013). "Eukaryotic Stress Granules Are Cleared by Autophagy and Cdc48/VCP Function." Cell **153**(7): 1461-1474.

Cai, X., X. Wang, S. Patel and D. E. Clapham (2015). "Insights into the early evolution of animal calcium signaling machinery: a unicellular point of view." Cell Calcium **57**(3): 166-173.

Chantarachot, T. and J. Bailey-Serres (2018). "Polysomes, Stress Granules, and Processing Bodies: A Dynamic Triumvirate Controlling Cytoplasmic mRNA Fate and Function." Plant Physiol **176**(1): 254-269.

Chen, L., B. Liao, H. Qi, L. J. Xie, L. Huang, W. J. Tan, N. Zhai, L. B. Yuan, Y. Zhou, L. J. Yu, Q. F. Chen, W. Shu and S. Xiao (2015). "Autophagy contributes to regulation of the hypoxia response during submergence in Arabidopsis thaliana." Autophagy **11**(12): 2233-2246.

Chin, D. and A. R. Means (2000). "Calmodulin: a prototypical calcium sensor." Trends Cell Biol **10**(8): 322-328.

Choi, W. G. (2009). Nodulin 26-like Intrinsic Protein NIP2;1 and NIP7;1: Characterization of Transport Functions and Roles in Developmental and Stress Responses in Arabidopsis. PhD PhD Diss., University of Tennessee.

Choi, W. G., R. Hilleary, S. J. Swanson, S. H. Kim and S. Gilroy (2016). "Rapid, Long-Distance Electrical and Calcium Signaling in Plants." Annu Rev Plant Biol **67**: 287-307.

Clapham, D. E. (2007). "Calcium signaling." Cell **131**(6): 1047-1058.

Contento, A. L., Y. Xiong and D. C. Bassham (2005). "Visualization of autophagy in Arabidopsis using the fluorescent dye monodansylcadaverine and a GFP-AtATG8e fusion protein." Plant J **42**(4): 598-608.

del Toro, F., F. T. Fernandez, J. Tilsner, K. M. Wright, F. Tenllado, B. N. Chung, S. Praveen and T. Canto (2014). "Potato virus Y HCPro localization at distinct, dynamically related and environment-influenced structures in the cell cytoplasm." Mol Plant Microbe Interact **27**(12): 1331-1343.

Dunn, K. W., M. M. Kamocka and J. H. McDonald (2011). "A practical guide to evaluating colocalization in biological microscopy." Am J Physiol Cell Physiol **300**(4): C723-742.

Durek, P., R. Schmidt, J. L. Heazlewood, A. Jones, D. MacLean, A. Nagel, B. Kersten and W. X. Schulze (2010). "PhosPhAt: the Arabidopsis thaliana phosphorylation site database. An update." Nucleic Acids Res **38**(Database issue): D828-834.

Earley, K. W., J. R. Haag, O. Pontes, K. Opper, T. Juehne, K. Song and C. S. Pikaard (2006). "Gateway-compatible vectors for plant functional genomics and proteomics." Plant J **45**(4): 616-629.

Earley, K. W., J. R. Haag, O. Pontes, K. Opper, T. Juehne, K. M. Song and C. S. Pikaard (2006). "Gateway-compatible vectors for plant functional genomics and proteomics." Plant Journal **45**(4): 616-629.

Echevarria-Zomeno, S., E. Yanguez, N. Fernandez-Bautista, A. B. Castro-Sanz, A. Ferrando and M. M. Castellano (2013). "Regulation of Translation Initiation under Biotic and Abiotic Stresses." Int J Mol Sci **14**(3): 4670-4683.

Edgar, R. C. (2004). "MUSCLE: multiple sequence alignment with high accuracy and high throughput." Nucleic Acids Res **32**(5): 1792-1797.

Endres, M. W., B. D. Gregory, Z. Gao, A. W. Foreman, S. Mlotshwa, X. Ge, G. J. Pruss, J. R. Ecker, L. H. Bowman and V. Vance (2010). "Two plant viral suppressors of silencing require the ethylene-inducible host transcription factor RAV2 to block RNA silencing." PLoS Pathog **6**(1): e1000729.

Foreman, M. W. (2012). The Role of Endogenous Arabidopsis Proteins In Rna Silencing and Hc-Pro-Mediated Suppression of Silencing.

Frankel, L. B., M. Lubas and A. H. Lund (2017). "Emerging connections between RNA and autophagy." Autophagy **13**(1): 3-23.

Frisch, D. A., L. W. Harris-Haller, N. T. Yokubaitis, T. L. Thomas, S. H. Hardin and T. C. Hall (1995). "Complete sequence of the binary vector Bin 19." Plant Mol Biol **27**(2): 405-409.

Fromm, M., L. P. Taylor and V. Walbot (1985). "Expression of Genes Transferred into Monocot and Dicot Plant-Cells by Electroporation." Proceedings of the National Academy of Sciences of the United States of America **82**(17): 5824-5828.

Fukao, T., B. E. Barrera-Figueroa, P. Juntawong and J. M. Pena-Castro (2019). "Submergence and Waterlogging Stress in Plants: A Review Highlighting Research Opportunities and Understudied Aspects." Front Plant Sci **10**: 340.

Fukuda, M., S. Wakuta, J. Kamiyo, T. Fujiwara and J. Takano (2018). "Establishment of genetically encoded biosensors for cytosolic boric acid in plant cells." Plant J.

Gilmore, A. M. (2013). "Luminescence : the instrumental key to the future of nanotechnology."

Giuntoli, B., S. C. Lee, F. Licausi, M. Kosmacz, T. Oosumi, J. T. van Dongen, J. Bailey-Serres and P. Perata (2014). "A trihelix DNA binding protein counterbalances hypoxia-responsive transcriptional activation in Arabidopsis." PLoS Biol **12**(9): e1001950.

Gjetting, S. K., A. Schulz and A. T. Fuglsang (2013). "Perspectives for using genetically encoded fluorescent biosensors in plants." Front Plant Sci **4**: 234.

Goold, H. D., P. Wright and D. Hailstones (2018). "Emerging Opportunities for Synthetic Biology in Agriculture." Genes (Basel) **9**(7).

Grefen, C. and M. R. Blatt (2012). "A 2in1 cloning system enables ratiometric bimolecular fluorescence complementation (rBiFC)." Biotechniques **53**(5): 311-314.

Gutierrez-Beltran, E., P. N. Moschou, A. P. Smertenko and P. V. Bozhkov (2015). "Tudor staphylococcal nuclease links formation of stress granules and processing bodies with mRNA catabolism in Arabidopsis." Plant Cell **27**(3): 926-943.

Hafren, A., S. Ustun, A. Hochmuth, S. Svenning, T. Johansen and D. Hofius (2018). "Turnip Mosaic Virus Counteracts Selective Autophagy of the Viral Silencing Suppressor HCpro." Plant Physiol **176**(1): 649-662.

Hattori, Y., K. Nagai, S. Furukawa, X. J. Song, R. Kawano, H. Sakakibara, J. Wu, T. Matsumoto, A. Yoshimura, H. Kitano, M. Matsuoka, H. Mori and M. Ashikari (2009). "The ethylene response factors SNORKEL1 and SNORKEL2 allow rice to adapt to deep water." Nature **460**(7258): 1026-1030.

Heazlewood, J. L., P. Durek, J. Hummel, J. Selbig, W. Weckwerth, D. Walther and W. X. Schulze (2008). "PhosPhAt: a database of phosphorylation sites in Arabidopsis thaliana and a plant-specific phosphorylation site predictor." Nucleic Acids Res **36**(Database issue): D1015-1021.

Hecker, A., N. Wallmeroth, S. Peter, M. R. Blatt, K. Harter and C. Grefen (2015). "Binary 2in1 Vectors Improve in Planta (Co)localization and Dynamic Protein Interaction Studies." Plant Physiol **168**(3): 776-787.

Hilleary, R., W. G. Choi, S. H. Kim, S. D. Lim and S. Gilroy (2018). "Sense and sensibility: the use of fluorescent protein-based genetically encoded biosensors in plants." Curr Opin Plant Biol **46**: 32-38.

Hink, M. A., R. A. Griep, J. W. Borst, A. van Hoek, M. H. Eppink, A. Schots and A. J. Visser (2000). "Structural dynamics of green fluorescent protein alone and fused with a single chain Fv protein." J Biol Chem **275**(23): 17556-17560.

Hofgen, R. and L. Willmitzer (1988). "Storage of competent cells for Agrobacterium transformation." Nucleic Acids Res **16**(20): 9877.

IPCC (2018). Global Warming of 1.5°C. An IPCC Special Report on the impacts of global warming of 1.5°C above pre-industrial levels and related global greenhouse gas emission pathways, in the context of strengthening the global response to the threat of climate change, sustainable development, and efforts to eradicate poverty.

Isabelle, M., J. P. Gagne, I. E. Gallouzi and G. G. Poirier (2012). "Quantitative proteomics and dynamic imaging reveal that G3BP-mediated stress granule assembly is poly(ADP-ribose)-dependent following exposure to MNNG-induced DNA alkylation." Journal of Cell Science **125**(19): 4555-4566.

Jones, D. T., W. R. Taylor and J. M. Thornton (1992). "The rapid generation of mutation data matrices from protein sequences." Comput Appl Biosci **8**(3): 275-282.

Jones, H. (1995). Plant gene transfer and expression protocols. Totowa, N.J., Humana Press.

Jouannet, V., A. B. Moreno, T. Elmayan, H. Vaucheret, M. D. Crespi and A. Maizel (2012). "Cytoplasmic Arabidopsis AGO7 accumulates in membrane-associated siRNA bodies and is required for ta-siRNA biogenesis." EMBO J **31**(7): 1704-1713.

Karimi, M., B. De Meyer and P. Hilson (2005). "Modular cloning in plant cells." Trends Plant Sci **10**(3): 103-105.

Kedersha, N. and P. Anderson (2009). "Regulation of translation by stress granules and processing bodies." Prog Mol Biol Transl Sci **90**: 155-185.

Kedersha, N., M. R. Cho, W. Li, P. W. Yacono, S. Chen, N. Gilks, D. E. Golan and P. Anderson (2000). "Dynamic shuttling of TIA-1 accompanies the recruitment of mRNA to mammalian stress granules." J Cell Biol **151**(6): 1257-1268.

Kedersha, N., G. Stoecklin, M. Ayodele, P. Yacono, J. Lykke-Andersen, M. J. Fitzler, D. Scheuner, R. J. Kaufman, D. E. Golan and P. Anderson (2005). "Stress granules and processing bodies are dynamically linked sites of mRNP remodeling." Journal of Cell Biology **169**(6): 871-884.

Khong, A. and R. Parker (2018). "mRNP architecture in translating and stress conditions reveals an ordered pathway of mRNP compaction." J Cell Biol **217**(12): 4124-4140.

Kimball, S. R., R. L. Horetsky, D. Ron, L. S. Jefferson and H. P. Harding (2003). "Mammalian stress granules represent sites of accumulation of stalled translation initiation complexes." American Journal of Physiology-Cell Physiology **284**(2): C273-C284.

Kodama, Y. (2016). "Time Gating of Chloroplast Autofluorescence Allows Clearer Fluorescence Imaging In Planta." PLoS One **11**(3): e0152484.

Koncz, C. and J. Schell (1986). "The Promoter of Tl-DNA Gene 5 Controls the Tissue-Specific Expression of Chimeric Genes Carried by a Novel Type of Agrobacterium Binary Vector." Molecular & General Genetics **204**(3): 383-396.

Krisenko, M. O., R. L. Higgins, S. Ghosh, Q. Zhou, J. S. Trybula, W. H. Wang and R. L. Geahlen (2015). "Syk Is Recruited to Stress Granules and Promotes Their Clearance through Autophagy." J Biol Chem **290**(46): 27803-27815.

Kudla, J. and R. Bock (2016). "Lighting the Way to Protein-Protein Interactions: Recommendations on Best Practices for Bimolecular Fluorescence Complementation Analyses." Plant Cell **28**(5): 1002-1008.

Kumakura, N., A. Takeda, Y. Fujioka, H. Motose, R. Takano and Y. Watanabe (2009). "SGS3 and RDR6 interact and colocalize in cytoplasmic SGS3/RDR6-bodies." FEBS Lett **583**(8): 1261-1266.

Kumar, R. V. (2019). "Plant Antiviral Immunity Against Geminiviruses and Viral Counter-Defense for Survival." Front Microbiol **10**: 1460.

Layzell, D. B., S. Hunt and G. R. Palmer (1990). "Mechanism of Nitrogenase Inhibition in Soybean Nodules : Pulse-Modulated Spectroscopy Indicates that Nitrogenase Activity Is Limited by O(2)." Plant Physiol **92**(4): 1101-1107.

Lelandais-Briere, C., L. Naya, E. Sallet, F. Calenge, F. Frugier, C. Hartmann, J. Gouzy and M. Crespi (2009). "Genome-Wide Medicago truncatula Small RNA Analysis Revealed Novel MicroRNAs and Isoforms Differentially Regulated in Roots and Nodules." Plant Cell **21**(9): 2780-2796.

Lellis, A. D., K. D. Kasschau, S. A. Whitham and J. C. Carrington (2002). "Loss-of-susceptibility mutants of Arabidopsis thaliana reveal an essential role for eIF(iso)4E during potyvirus infection." Current Biology **12**(12): 1046-1051.

Li, F., C. Huang, Z. Li and X. Zhou (2014). "Suppression of RNA silencing by a plant DNA virus satellite requires a host calmodulin-like protein to repress RDR6 expression." PLoS Pathog **10**(2): e1003921.

Li, F., N. Zhao, Z. Li, X. Xu, Y. Wang, X. Yang, S. S. Liu, A. Wang and X. Zhou (2017). "A calmodulin-like protein suppresses RNA silencing and promotes geminivirus infection by degrading SGS3 via the autophagy pathway in Nicotiana benthamiana." PLoS Pathog **13**(2): e1006213.

Licausi, F., M. Kosmacz, D. A. Weits, B. Giuntoli, F. M. Giorgi, L. A. Voesenek, P. Perata and J. T. van Dongen (2011). "Oxygen sensing in plants is mediated by an N-end rule pathway for protein destabilization." Nature **479**(7373): 419-422.

Licausi, F., M. Kosmacz, D. A. Weits, B. Giuntoli, F. M. Giorgi, L. A. C. J. Voesenek, P. Perata and J. T. van Dongen (2011). "Oxygen sensing in plants is mediated by an N-end rule pathway for protein destabilization." Nature **479**: 419.

Liu, J., M. A. Valencia-Sanchez, G. J. Hannon and R. Parker (2005). "MicroRNA-dependent localization of targeted mRNAs to mammalian P-bodies." Nat Cell Biol **7**(7): 719-723.

Liu, L. and X. Chen (2016). "RNA Quality Control as a Key to Suppressing RNA Silencing of Endogenous Genes in Plants." Molecular Plant **9**(6): 826-836.

Liu, X. M., A. Yamasaki, X. M. Du, V. C. Coffman, Y. Ohsumi, H. Nakatogawa, J. Q. Wu, N. N. Noda and L. L. Du (2018). "Lipidation-independent vacuolar functions of Atg8 rely on its noncanonical interaction with a vacuole membrane protein." Elife **7**.

Lokdarshi, A. (2015). Calmodulin-like protein 38: a component of ribonucleoprotein particles during hypoxic stress responses in Arabidopsis. PhD, University of Tennessee.

Lokdarshi, A., W. C. Conner, C. McClintock, T. Li and D. M. Roberts (2016). "Arabidopsis CML38, a Calcium Sensor That Localizes to Ribonucleoprotein Complexes under Hypoxia Stress." Plant Physiol **170**(2): 1046-1059.

Lokdarshi, A., W. C. Conner, C. McClintock, T. Li and D. M. Roberts (2016). "Arabidopsis CML38, a Calcium Sensor That Localizes to Ribonucleoprotein Complexes under Hypoxia Stress." Plant Physiology **170**(2): 1046-1059.

Makiyama, R. K., C. A. H. Fernandes, T. R. Dreyer, B. S. Moda, F. F. Matioli, M. R. M. Fontes and I. G. Maia (2016). "Structural and thermodynamic studies of the tobacco calmodulin-like rgs-CaM protein." International Journal of Biological Macromolecules **92**: 1288-1297.

Maldonado-Bonilla, L. D. (2014). "Composition and function of P bodies in Arabidopsis thaliana." Front Plant Sci **5**: 201.

Manders, E. M., J. Stap, G. J. Brakenhoff, R. van Driel and J. A. Aten (1992). "Dynamics of three-dimensional replication patterns during the S-phase, analysed by double labelling of DNA and confocal microscopy." J Cell Sci **103 (Pt 3)**: 857-862.

Marshall, R. S. and R. D. Vierstra (2018). "Autophagy: The Master of Bulk and Selective Recycling." Annu Rev Plant Biol **69**: 173-208.

Martinez, G., P. Wolff, Z. Wang, J. Moreno-Romero, J. Santos-Gonzalez, L. L. Conze, C. DeFraia, R. K. Slotkin and C. Kohler (2018). "Paternal easiRNAs regulate parental genome dosage in Arabidopsis." Nat Genet **50**(2): 193-198.

McCormack, E. and J. Braam (2003). "Calmodulins and related potential calcium sensors of Arabidopsis." New Phytologist **159**(3): 585-598.

McCormack, E., Y. C. Tsai and J. Braam (2005). "Handling calcium signaling: Arabidopsis CaMs and CMLs." Trends Plant Sci **10**(8): 383-389.

Michaeli, S., G. Galili, P. Genschik, A. R. Fernie and T. Avin-Wittenberg (2016). "Autophagy in Plants--What's New on the Menu?" Trends Plant Sci **21**(2): 134-144.

Minchin, F. R. (1997). "Regulation of oxygen diffusion in legume nodules." Soil Biology and Biochemistry **29**(5): 881-888.

Muller, M. and S. Munne-Bosch (2015). "Ethylene Response Factors: A Key Regulatory Hub in Hormone and Stress Signaling." Plant Physiol **169**(1): 32-41.

Mustroph, A., M. E. Zanetti, C. J. Jang, H. E. Holtan, P. P. Repetti, D. W. Galbraith, T. Girke and J. Bailey-Serres (2009). "Profiling translatomes of discrete cell populations resolves altered cellular priorities during hypoxia in Arabidopsis." Proc Natl Acad Sci U S A **106**(44): 18843-18848.

Nakahara, K. S., C. Masuta, S. Yamada, H. Shimura, Y. Kashihara, T. S. Wada, A. Meguro, K. Goto, K. Tadamura, K. Sueda, T. Sekiguchi, J. Shao, N. Itchoda, T. Matsumura, M. Igarashi, K. Ito, R. W. Carthew and I. Uyeda (2012). "Tobacco calmodulin-like protein provides secondary defense by binding to and directing degradation of virus RNA silencing suppressors." Proc Natl Acad Sci U S A **109**(25): 10113-10118.

Nakamura, H., M. R. Shin, T. Fukagawa, M. Arita, T. Mikami and H. Kodama (2014). "A tobacco calmodulin-related protein suppresses sense transgene-induced RNA silencing but not inverted repeat-induced RNA silencing." Plant Cell Tissue and Organ Culture **116**(1): 47-53.

Nakayama, S. and R. H. Kretsinger (1994). "Evolution of the EF-hand family of proteins." Annu Rev Biophys Biomol Struct **23**: 473-507.

Nolan, T. M., B. Brennan, M. Yang, J. Chen, M. Zhang, Z. Li, X. Wang, D. C. Bassham, J. Walley and Y. Yin (2017). "Selective Autophagy of BES1 Mediated by DSK2 Balances Plant Growth and Survival." Dev Cell **41**(1): 33-46 e37.

OpenWetWare. (2018, 10 December 2018). "'Round-the-horn site-directed mutagenesis." from https://openwetware.org/mediawiki/index.php?title=%27Round-the-horn_site-directed_mutagenesis&oldid=1055958.

Popescu, S. C., G. V. Popescu, S. Bachan, Z. M. Zhang, M. Seay, M. Gerstein, M. Snyder and S. P. Dinesh-Kumar (2007). "Differential binding of calmodulin-related proteins to their targets revealed through high-density Arabidopsis protein microarrays." Proceedings of the National Academy of Sciences of the United States of America **104**(11): 4730-4735.

Protter, D. S. W. and R. Parker (2016). "Principles and Properties of Stress Granules." Trends Cell Biol **26**(9): 668-679.

Pumplin, N. and O. Voinnet (2013). "RNA silencing suppression by plant pathogens: defence, counter-defence and counter-counter-defence." Nat Rev Microbiol **11**(11): 745-760.

Rhoads, A. R. and F. Friedberg (1997). "Sequence motifs for calmodulin recognition." FASEB J **11**(5): 331-340.

Samaha, H., V. Delorme, F. Pontvianne, R. Cooke, F. Delalande, A. Van Dorsselaer, M. Echeverria and J. Saez-Vasquez (2010). "Identification of protein factors and U3 snoRNAs from a Brassica oleracea RNP complex involved in the processing of pre-rRNA." Plant Journal **61**(3): 383-398.

Schneider, C. A., W. S. Rasband and K. W. Eliceiri (2012). "NIH Image to ImageJ: 25 years of image analysis." Nat Methods **9**(7): 671-675.

Schwarz, D. S., G. Hutvagner, T. Du, Z. Xu, N. Aronin and P. D. Zamore (2003). "Asymmetry in the assembly of the RNAi enzyme complex." Cell **115**(2): 199-208.

Sculthorpe, C. D. (1967). The biology of aquatic vascular plants. London,, Edward Arnold.

Sedbrook, J. C., P. J. Kronebusch, G. G. Borisy, A. J. Trewavas and P. H. Masson (1996). "Transgenic AEQUORIN reveals organ-specific cytosolic Ca2+ responses to anoxia and Arabidopsis thaliana seedlings." Plant Physiol **111**(1): 243-257.

Sen, G. L. and H. M. Blau (2005). "Argonaute 2/RISC resides in sites of mammalian mRNA decay known as cytoplasmic bodies." Nat Cell Biol **7**(6): 633-636.

Sesma, A., C. Castresana and M. M. Castellano (2017). "Regulation of Translation by TOR, eIF4E and eIF2alpha in Plants: Current Knowledge, Challenges and Future Perspectives." Front Plant Sci **8**: 644.

Shin, M. R., M. Natsuume, T. Matsumoto, M. Hanaoka, M. Imai, K. Iijima, S. Oka, E. Adachi and H. Kodama (2014). "Sense Transgene-Induced Post-Transcriptional Gene Silencing in Tobacco Compromises the Splicing of Endogenous Counterpart Genes." Plos One **9**(2).

Shukla, V., L. Lombardi, S. Iacopino, A. Pencik, O. Novak, P. Perata, B. Giuntoli and F. Licausi (2019). "Endogenous Hypoxia in Lateral Root Primordia Controls Root Architecture by Antagonizing Auxin Signaling in Arabidopsis." Mol Plant **12**(4): 538-551.

Siomi, H. and M. C. Siomi (2009). "On the road to reading the RNA-interference code." Nature **457**(7228): 396-404.

Sorenson, R. and J. Bailey-Serres (2014). "Selective mRNA sequestration by OLIGOURIDYLATE-BINDING PROTEIN 1 contributes to translational control during hypoxia in Arabidopsis." Proceedings of the National Academy of Sciences of the United States of America **111**(6): 2373-2378.

Steffens, A., B. Jaegle, A. Tresch, M. Hulskamp and M. Jakoby (2014). "Processing-body movement in Arabidopsis depends on an interaction between myosins and DECAPPING PROTEIN1." Plant Physiol **164**(4): 1879-1892.

Stewart, W. N. and G. W. Rothwell (1993). Paleobotany and the evolution of plants. New York, Cambridge University Press.

Stolz, A., A. Ernst and I. Dikic (2014). "Cargo recognition and trafficking in selective autophagy." Nat Cell Biol **16**(6): 495-501.

Subbaiah, C. C., D. S. Bush and M. M. Sachs (1994). "Elevation of cytosolic calcium precedes anoxic gene expression in maize suspension-cultured cells." Plant Cell **6**(12): 1747-1762.

Subbaiah, C. C., J. Zhang and M. M. Sachs (1994). "Involvement of intracellular calcium in anaerobic gene expression and survival of maize seedlings." Plant Physiol **105**(1): 369-376.

Tamura, K., G. Stecher, D. Peterson, A. Filipski and S. Kumar (2013). "MEGA6: Molecular Evolutionary Genetics Analysis version 6.0." Mol Biol Evol **30**(12): 2725-2729.

Tasaki, T., S. M. Sriram, K. S. Park and Y. T. Kwon (2012). "The N-end rule pathway." Annu Rev Biochem **81**: 261-289.

Thevenaz, P., U. E. Ruttimann and M. Unser (1998). "A pyramid approach to subpixel registration based on intensity." IEEE Trans Image Process **7**(1): 27-41.

Tzfadia, O. and G. Galili (2013). "The Arabidopsis exocyst subcomplex subunits involved in a golgi-independent transport into the vacuole possess consensus autophagy-associated atg8 interacting motifs." Plant Signal Behav **8**(10): doi: 10 4161/psb 26732.

van Dongen, J. T. and F. Licausi (2015). "Oxygen sensing and signaling." Annu Rev Plant Biol **66**: 345-367.

van Steensel, B., E. P. van Binnendijk, C. D. Hornsby, H. T. van der Voort, Z. S. Krozowski, E. R. de Kloet and R. van Driel (1996). "Partial colocalization of glucocorticoid and mineralocorticoid receptors in discrete compartments in nuclei of rat hippocampus neurons." J Cell Sci **109 (Pt 4)**: 787-792.

Virdi, A. S., S. Singh and P. Singh (2015). "Abiotic stress responses in plants: roles of calmodulin-regulated proteins." Front Plant Sci **6**: 809.

Voesenek, L. A. and J. Bailey-Serres (2015). "Flood adaptive traits and processes: an overview." New Phytol **206**(1): 57-73.

Walia, A., R. Waadt and A. M. Jones (2018). "Genetically Encoded Biosensors in Plants: Pathways to Discovery." Annu Rev Plant Biol **69**: 497-524.

Wang, X., Y. Bian, K. Cheng, L. F. Gu, M. Ye, H. Zou, S. S. Sun and J. X. He (2013). "A large-scale protein phosphorylation analysis reveals novel phosphorylation motifs and phosphoregulatory networks in Arabidopsis." J Proteomics **78**: 486-498.

Wang, X. B., J. Jovel, P. Udomporn, Y. Wang, Q. Wu, W. X. Li, V. Gasciolli, H. Vaucheret and S. W. Ding (2011). "The 21-nucleotide, but not 22-nucleotide, viral secondary small interfering RNAs direct potent antiviral defense by two cooperative argonautes in Arabidopsis thaliana." Plant Cell **23**(4): 1625-1638.

Weber, C., L. Nover and M. Fauth (2008). "Plant stress granules and mRNA processing bodies are distinct from heat stress granules." Plant Journal **56**(4): 517-530.

Weits, D. A., B. Giuntoli, M. Kosmacz, S. Parlanti, H. M. Hubberten, H. Riegler, R. Hoefgen, P. Perata, J. T. van Dongen and F. Licausi (2014). "Plant cysteine oxidases control the oxygen-dependent branch of the N-end-rule pathway." Nat Commun **5**: 3425.

White, M. D., J. Kamps, S. East, L. J. Taylor Kearney and E. Flashman (2018). "The plant cysteine oxidases from Arabidopsis thaliana are kinetically tailored to act as oxygen sensors." J Biol Chem **293**(30): 11786-11795.

Willmann, M. R., M. W. Endres, R. T. Cook and B. D. Gregory (2011). "The Functions of RNA-Dependent RNA Polymerases in Arabidopsis." Arabidopsis Book **9**: e0146.

Wu, L., L. Mao and Y. Qi (2012). "Roles of dicer-like and argonaute proteins in TAS-derived small interfering RNA-triggered DNA methylation." Plant Physiol **160**(2): 990-999.

Xu, K., X. Xu, T. Fukao, P. Canlas, R. Maghirang-Rodriguez, S. Heuer, A. M. Ismail, J. Bailey-Serres, P. C. Ronald and D. J. Mackill (2006). "Sub1A is an ethylene-response-factor-like gene that confers submergence tolerance to rice." Nature **442**(7103): 705-708.

Yamaguchi, M., N. N. Noda, H. Nakatogawa, H. Kumeta, Y. Ohsumi and F. Inagaki (2010). "Autophagy-related protein 8 (Atg8) family interacting motif in Atg3 mediates the Atg3-Atg8 interaction and is crucial for the cytoplasm-to-vacuole targeting pathway." J Biol Chem **285**(38): 29599-29607.

Yan, C., Z. Yan, Y. Wang, X. Yan and Y. Han (2014). "Tudor-SN, a component of stress granules, regulates growth under salt stress by modulating GA20ox3 mRNA levels in Arabidopsis." J Exp Bot **65**(20): 5933-5944.

Yong Chung, H., G. Lacatus and G. Sunter (2014). "Geminivirus AL2 protein induces expression of, and interacts with, a calmodulin-like gene, an endogenous regulator of gene silencing." Virology **460-461**: 108-118.

Yuan, P., E. Jauregui, L. Du, K. Tanaka and B. W. Poovaiah (2017). "Calcium signatures and signaling events orchestrate plant-microbe interactions." Curr Opin Plant Biol **38**: 173-183.

Zaffagnini, G. and S. Martens (2016). "Mechanisms of Selective Autophagy." J Mol Biol **428**(9 Pt A): 1714-1724.

Zhan, N., C. Wang, L. Chen, H. Yang, J. Feng, X. Gong, B. Ren, R. Wu, J. Mu, Y. Li, Z. Liu, Y. Zhou, J. Peng, K. Wang, X. Huang, S. Xiao and J. Zuo (2018). "S-Nitrosylation Targets GSNO Reductase for Selective Autophagy during Hypoxia Responses in Plants." Mol Cell **71**(1): 142-154 e146.

Zhou, R., L. M. Benavente, A. N. Stepanova and J. M. Alonso (2011). "A recombineering-based gene tagging system for Arabidopsis." Plant J **66**(4): 712-723.

Zhu, J. K. (2016). "Abiotic Stress Signaling and Responses in Plants." Cell **167**(2): 313-324.

Zulawski, M., R. Braginets and W. X. Schulze (2013). "PhosPhAt goes kinases--searchable protein kinase target information in the plant phosphorylation site database PhosPhAt." Nucleic Acids Res **41**(Database issue): D1176-1184.

Vita

Craig Conner was born in 1985 in Chattanooga, Tennessee. He attended the University of Tennessee in Knoxville in 2003 and graduated in 2007 with a biological sciences degree, from the department of Biochemistry & Cellular and Molecular Biology. After a period working with his family's business, he spent a year doing research in the lab of Dr. Jae Park at the University of Tennessee. This work resulted in his first publication on the neuropeptide corazonin in the fly species, *Musca domestica*, and solidified his interest in scientific research. Craig began his graduate education in the Biochemistry & Cellular and Molecular Biology at the University of Tennessee in 2010.

Craig did his PhD research in the lab of Daniel Roberts and has worked on projects relating to plant calcium sensor proteins of the "regulator of gene silencing" family. Craig's early research investigated roles for these calcium sensors in the nitrogen-fixing root nodules of *Medicao truncatula,* and towards the biochemical assessment of regulator of gene silencing calmodulin from *Nicotiana tabacum*. Following the lab's initial publication on the Arabidopsis homolog as a component of hypoxia-induced stress granules, on which he was a co-author, Craig decided that our understanding of this protein family could best be advanced by furthering our understanding of the cell biology of these proteins. This research produced the results and the model presented here, and supports the idea that these proteins act as autophagy cargo adaptors for stress-induced mRNP granulophagy.

During his PhD work, Craig also consistently worked as a graduate teaching assistant and developed a love and aptitude for teaching at the undergraduate level.

Following this interest, he will begin teaching a second-semester biochemistry course for senior undergraduates, as a lecturer for the University of Tennessee.